

## DUST AND GAS IN NGC3627



DUST AND GAS IN NGC3627 USING OBSERVATIONS FROM  
SCUBA-2

By

JONATHAN H. NEWTON, B.A.

A Thesis

Submitted to the School of Graduate Studies

in Partial Fulfilment of the Requirements

for the Degree

Master of Science

McMaster University

©Copyright by Jonathan Newton, August 2014

MASTER OF SCIENCE (2014)

McMaster University

(Physics and Astronomy)

Hamilton, Ontario

TITLE: Dust and Gas in NGC3627 Using Observations from SCUBA-2

AUTHOR: Jonathan Newton, B.A. (Western Kentucky University)

SUPERVISOR: Christine D. Wilson

NUMBER OF PAGES: xiv, 104

# Abstract

This thesis presents new  $450\mu\text{m}$  and  $850\mu\text{m}$  observations of NGC3627 taken with the new SCUBA-2 with the main goal of trying to better understand the properties of gas and dust in the interstellar medium of NGC3627. We determined properties of the cold component of NGC3627's spectral energy distribution (SED) using dust models given by the Planck Collaboration, by Li and Draine, and allowing the emissivity index to be treated as a free parameter. Fitting the SED required the use of  $100\mu\text{m}$ ,  $160\mu\text{m}$ ,  $250\mu\text{m}$ ,  $350\mu\text{m}$ , and  $500\mu\text{m}$  data from the KINGFISH survey. Each of the KINGFISH observations have been passed through an extended emission filter in order to match the SCUBA-2 observations. The best fit temperatures and emissivity indices agreed with the results found in other recent studies, but our fitted masses were smaller than those of other studies due to differences in the fitted temperature and observed fluxes.

After the properties of the dust emission were calculated, we implemented a method to determine the amount of molecular hydrogen present in NGC3627. The method we used involves finding a CO-to-H<sub>2</sub> conversion factor that minimizes the scatter present in dust-to-gas mass ratio. We used CO J=2-1 from the HERACLES survey and CO J=1-0 from the Nobeyama 45-m telescope to act as our molecular tracer, and HI observations of NGC3627 from the THINGS survey. The results from minimizing the dust-to-gas ratio scatter give low  $\alpha_{CO}$  values, that are normally associated with U/LIRGs. The low  $\alpha_{CO}$  values can be attributed to the treatment of the error associated with reported  $\alpha_{CO}$ . The uncertainties for  $\alpha_{CO}$  reported in this thesis are a minimum

estimate, and if the error associated with  $\alpha_{CO}$  is large enough, then the best fit  $\alpha_{CO}$  values can be considered as a lower threshold for the system.

*To my family and Poly.*

# Acknowledgements

*When life looks like easy street, there is danger at your door... -Robert Hunter*

First and foremost I would like to thank my advisor Chris for helping me interpret my results and for polishing the roughest of thesis drafts to get a final copy out. I would also like to thank my officemates, Damien, Kaz, Max, Tara, and Angus, for the putting up with office pranks and shenanigans and their invaluable input into research discussions. I would also like to thank the other offices for the much needed coffee breaks and general comradery. Go Liquid State! I would also like to thank my parents for having me and always being there if things got a little rough. I would like to thank the rest of my family for their never ending encouragement. I also need to thank Christian who laid the initial groundwork to making SCUBA-2 Maps. I would also like to thank John Elway whose front office prowess has helped to make Sundays much more bearable. Go Broncos!



# Table of Contents

<b>Descriptive Notes</b>	ii
<b>Abstract</b>	iii
<b>Acknowledgements</b>	vi
<b>List of Figures</b>	x
<b>List of Tables</b>	xiii
 <b>Chapter 1 Introduction</b>	 <b>1</b>
1.1 The Interstellar Medium . . . . .	1
1.1.1 GMC Formation . . . . .	2
1.1.2 Molecular Hydrogen Formation . . . . .	3
1.1.3 Dissociation of Molecular Hydrogen . . . . .	7
1.2 Determining the H <sub>2</sub> Abundance . . . . .	8
1.2.1 Methods for Determining CO-to-H <sub>2</sub> Conversion Factor	10
1.3 Determining Dust Mass . . . . .	13
1.4 NGC 3627 . . . . .	17
 <b>Chapter 2 Observations and Data Preparation</b>	 <b>22</b>
2.1 SCUBA-2 . . . . .	22
2.2 Image Creation and Properties . . . . .	23
2.2.1 Beam Shape of the 450 $\mu$ m and 850 $\mu$ m Data . . . . .	30

2.3	Ancillary Data . . . . .	33
2.3.1	Key Insights on Nearby Galaxies: a Far-Infrared Survey with Herschel (KINGFISH) . . . . .	35
2.3.2	Nearby Galaxies Legacy Survey (NGLS) . . . . .	41
2.3.3	Nobeyama 45-m . . . . .	41
2.3.4	Hetrodyne Receiver Array CO-Line Extragalactic Sur- vey (HERACLES) . . . . .	43
2.3.5	The HI Nearby Galaxy Survey (THINGS) . . . . .	45
2.4	Data Preparation for Analysis . . . . .	47
2.4.1	Accounting for the $450\mu\text{m}$ Error Beam . . . . .	49
2.4.2	Extended Structure Removal via MAKEMAP . . . . .	50
<b>Chapter 3 Spectral Energy Distribution Analysis</b>		<b>55</b>
3.1	SED Fitting Method . . . . .	55
3.2	Fitting the Spectral Energy Distribution . . . . .	58
3.2.1	Pixel SED Fits . . . . .	58
3.2.2	Total Region Flux SED Fits . . . . .	64
3.3	Discussion . . . . .	75
3.3.1	Reliability of Individual Pixel Fits . . . . .	75
3.3.2	Comparison with Previous Work . . . . .	76
3.3.3	Effects of $850\mu\text{m}$ Emission . . . . .	77

<b>Chapter 4</b>	<b>Dust-to-Gas Ratio and <math>\alpha_{CO}</math></b>	<b>79</b>
4.1	Minimizing the Scatter in the Dust-to-Gas Ratio . . . . .	79
4.2	Effects of the Dust Model and CO Treatment . . . . .	87
4.3	Comparison of Results with Previous Work . . . . .	90
4.4	Caveats Due to Uncertainty Estimation . . . . .	91
<b>Chapter 5</b>	<b>Summary</b>	<b>96</b>

# List of Figures

1.1	Optical Image of NGC3627 . . . . .	19
2.1	Iterative Steps Used In MAKEMAP . . . . .	26
2.2	Flux Values vs High-Pass Filter Sizes . . . . .	27
2.3	450 $\mu$ m High-Pass Filter Images . . . . .	28
2.4	850 $\mu$ m High-Pass Filter Images . . . . .	29
2.5	NGC3627 450 $\mu$ m Observations . . . . .	31
2.6	NGC3627 850 $\mu$ m Observations . . . . .	32
2.7	SCUBA-2 Calibration and Beams . . . . .	34
2.8	NGC3627 100 $\mu$ m Observations . . . . .	36
2.9	NGC3627 160 $\mu$ m Observations . . . . .	37
2.10	NGC3627 250 $\mu$ m Observations . . . . .	38
2.11	NGC3627 350 $\mu$ m Observations . . . . .	39
2.12	NGC3627 500 $\mu$ m Observations . . . . .	40
2.13	NGC3627 CO J=3-2 Observations . . . . .	42
2.14	NGC3627 CO J=1-0 Observations . . . . .	44
2.15	NGC3627 CO J=2-1 Observations . . . . .	46
2.16	NGC3627 HI Observations . . . . .	48
2.17	100 $\mu$ m Filtering Steps . . . . .	53

2.18	HI surface density filtering Steps . . . . .	54
3.1	NGC3627 Regions . . . . .	59
3.2	NGC3627 Observations Used in SED Fitting . . . . .	61
3.2	(continued) . . . . .	62
3.3	Li and Draine Model SED Fit Quality Using $450\mu\text{m}$ Data . . . . .	63
3.4	Planck Model SED Fit Quality Using $500\mu\text{m}$ Data . . . . .	65
3.5	Li and Draine Model SED Fit Quality Using $500\mu\text{m}$ Data . . . . .	66
3.6	Emissivity as a Free Parameter SED Fit Quality using the $500\mu\text{m}$ Data . . . . .	67
3.7	SED Parameter Maps . . . . .	69
3.8	Initial Mass Dependence and Convergence of SED Fits for Region Fluxes and Variable Emissivity Index . . . . .	71
3.9	Initial Mass Dependence and Convergence of SED Fits for Region Fluxes and Fixed Emissivity Index . . . . .	72
3.10	Region Flux Best Emissivity Index Selection . . . . .	73
3.11	Region Flux SED Fits . . . . .	74
4.1	Dust-to-Gas Ratio Determination Plots for CO J=1-0 . . . . .	82
4.1	(continued) . . . . .	83
4.1	(continued) . . . . .	84
4.1	(Continued) . . . . .	87

4.2	Mean Dust-to-Gas Ratio vs $\alpha_{CO}$ . . . . .	88
4.3	Unfiltered Dust-to-Gas Ratio Determination Plots for CO J=2-1 .	93
4.4	Mean Dust-to-Gas Ratio vs $\alpha_{CO}$ Without Extended Emission Filtering . . . . .	94

# List of Tables

2.1	Properties of NGC3627 SCUBA-2 Observations . . . . .	30
2.2	Properties of NGC3627 KINGFISH Observations . . . . .	41
2.3	Properties of NGC3627 Gas Observations . . . . .	43
3.1	Systematic Calibration Uncertainties for SCUBA-2 and KINGFISH Observations . . . . .	56
3.2	Total Distance to 1 to 1 Line Using the 500 $\mu$ m Emission . . . . .	64
3.3	Best Fit Parameters for Planck Model Using 500 $\mu$ m Emission for Pixel Fits . . . . .	64
3.4	Best Fit Parameters for Li and Draine Model Using 500 $\mu$ m Emis- sion for Pixel Fits . . . . .	68
3.5	Best Fit Parameters for $\beta$ As A Free Parameter Using 500 $\mu$ m Emis- sion for Pixel Fits . . . . .	68
3.6	Best Fit Parameters for Planck Opacity Using Region Fluxes . . . .	71
3.7	Best Fit Parameters Excluding 850 $\mu$ m Emission Using Planck Opac- ity with Variable Emissivity Index . . . . .	78
4.1	Dust-to-gas ratio, $\alpha_{CO}$ , and H <sub>2</sub> Surface Density using CO J=1-0 as the H <sub>2</sub> Tracer . . . . .	85
4.2	Dust-to-gas ratio, $\alpha_{CO}$ , and H <sub>2</sub> Surface Density using CO J=2-1 as the H <sub>2</sub> Tracer . . . . .	86

4.3	CO Transition, $\alpha_{CO}$ , and $H_2$ Surface Density using the Li and Draine dust model with No Spatial Filtering of CO or HI . . .	92
-----	--	----



# Chapter 1

## Introduction

### 1.1 The Interstellar Medium

The interstellar medium (ISM) is the material that fills the space between the stars in galaxies and is composed of cosmic rays, magnetic field lines, dust, and gas. Each one of these constituents plays a role in shaping the overall physical and chemical behavior of a galaxy (Ferrière, 2001). This material is inhomogeneously spread about the galaxy's disk with dust and gas densities ranging from 1 particle per a thousand cubic centimeters to millions of particles per cubic centimeter ( $10^6 \geq N \geq 10^{-3}$ ), and temperatures ranging from 10 K in the most dense regions to  $10^6$  K in the most diffuse (Ferrière, 2001). The constituents of the ISM will interact leading to the creation of molecular gas in giant molecular clouds (GMCs) and eventually to the formation of stars (Field & Saslaw, 1965). After the stars are formed, they will eject new material back into the ISM through stellar winds and supernovae repopulating the ISM, where each successive iteration introduces heavier atoms creating a galactic ecosystem (Ferrière, 2001). In this thesis we focus on the physical

properties of the dust component of the ISM of the nearby barred spiral galaxy NGC3627 and also use the dust properties to learn more about its molecular gas properties.

### 1.1.1 GMC Formation

Intergalactic gas can be accreted into a host galaxy where it will condense and lead to the formation of molecular clouds (Kennicutt & Evans, 2012). The dominant process of GMC formation is divided between two camps, either a “bottom-up” or “top-down” formation scenario (McKee & Ostriker, 2007). The bottom-up scenario consists of small clouds of cold HI coagulating to eventually form a GMC (Field & Saslaw, 1965; Kwan, 1979). The major concern with the bottom-up scenario is if we include heating mechanisms in the cloud, coagulation will cease before the observed masses are reached (McKee & Ostriker, 2007). The amount of time to accumulate enough mass to form a relatively small GMC of  $10^5 M_{\odot}$  would take around  $10^8$  years which is much greater than the expected lifetime of a GMC (Kwan, 1979).

Given the extreme timescales required in the bottom up scenario, a more feasible formation has been suggested. The alternative formation scenario, top-down, postulates that GMC formation comes from instabilities in the diffuse ISM causing the clouds to collapse from their surrounding medium (McKee & Ostriker, 2007). Two main instabilities are thought to be responsible for the collapse. The first type of instability is a Parker instability, which involves distortion of magnetic field lines in the mid-plane of the galaxy, and at the location of these distortions gas will begin to accumulate (Parker, 1966; Dobbs

et al., 2013). The second instability responsible for collapse can be determined by the amount of rotational shear present (McKee & Ostriker, 2007). If a strong rotational shear is present, such as in the inter-arm region of a spiral galaxy, then the accumulation of gas will be due to its shearing as it moves through the disk of a galaxy in a process known as swing amplification (McKee & Ostriker, 2007; Dobbs et al., 2013). If no rotational shear is present, such as in the inner regions of a galaxy or spiral arms, then the collapse can be attributed to a magneto-Jeans instability which will remove the angular momentum responsible for the rotational shear through magnetic fields in order for the normal Jeans instability to occur (Elmegreen, 1987; Kim & Ostriker, 2001).

### 1.1.2 Molecular Hydrogen Formation

Regardless of either collapse or coagulation, molecular hydrogen is being formed inside the cloud. Molecular hydrogen can be formed via the two body reaction, three body reaction, formation using a free electron or proton, or surface formation (Krumholz, 2014). The two body formation scenario is the simplest reaction using two hydrogen atoms to produce molecular hydrogen,



However, two body formation is not the major mechanism in the formation of  $\text{H}_2$  due to the requirement of a forbidden photon that arises from the combination of hydrogen atoms in the ground state (Gould & Salpeter, 1963). If

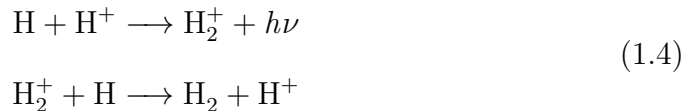
one of the hydrogen atoms is excited, the transition can occur and molecular hydrogen is formed, but the number of excited hydrogen atoms in the temperature ranges typical of the cold and warm phases of the ISM are expected to be nearly nonexistent (Krumholz, 2014).

The second formation scenario listed, three body formation, involves three hydrogen atoms coming together to form molecular hydrogen with a spare hydrogen atom,



The required density for three body formation to occur is on the order of  $10^8 \text{ cm}^{-3}$  (Palla et al., 1983; Abel et al., 1997), while the typical GMC density is on the order of  $300 \text{ cm}^{-3}$ . The disparity between these densities eliminates any possibility of this being the primary mechanism to form molecular hydrogen in galaxies today.

An alternative to the two or three body reactions uses either an electron or proton to ionize the hydrogen forming either  $\text{H}^-$  or  $\text{H}_2^+$  (Krumholz, 2014). The chemical reaction involving an electron is shown in equation 1.3, and the equation utilizing a proton is shown in reaction 1.4



The main limitation of the free electron/proton formation mechanism is an undersupply of free electrons and protons. Typical Milky Way conditions show that regions with a density  $>1 \text{ cm}^{-3}$  have free electron and proton densities  $<10^{-4} \text{ cm}^{-3}$  (Wolfire et al., 2003). Secondly, the  $\text{H}^-$  ion in equation 1.3 is more likely to interact with a stray photon than an electron resulting in the ion returning to the atomic state (Glover, 2003). While we observe singly ionized hydrogen regions, HII regions, only a small fraction of the region will successfully produce molecular hydrogen.

While the free electron/proton formation method is suspected to be the primary  $\text{H}_2$  catalyst in the early universe (Herbst et al., 2005), at low redshifts the formation of molecular hydrogen on the surface of dust grains is the dominant formation mechanism (Krumholz, 2014). Surface formation of molecular hydrogen will occur when a hydrogen atom strikes a dust grain and successfully sticks to the grain. The hydrogen will then interact with another hydrogen atom to form  $\text{H}_2$  and be ejected from the dust particle after the reaction has occurred (Pirronello et al., 1997). The same process occurs on the dust grain as the two body formation in the gas phase, but the dust grain will act as a medium to absorb the energy that would create the forbidden photon (Krumholz, 2014).

With a dominant mechanism for molecular hydrogen formation, a reaction rate can be defined based on the cross section of the grain,  $\Sigma_{gr}$ , a striking probability dependent on the temperature of the observed dust,  $S(T)$ , the probability of molecular hydrogen forming on the grain,  $\epsilon_{\text{H}_2}$ , the density of free hydrogen in the GMC,  $n_H$ , and the density of hydrogen attached to the

grain surface,  $n_{H_0}$  (Krumholz, 2014). Scaling the product of these properties with the integrated collisional probability of a Maxwellian gas, the reaction rate is determined to be

$$\frac{dn_{H_2}}{dt} = \frac{1}{2} \left( \frac{8k_b T}{\pi m_H} \right)^{\frac{1}{2}} \Sigma_{gr} S(T) \epsilon_{H_2} n_H n_{H_0} \quad (1.5)$$

where  $k_b$  is the Boltzmann constant,  $T$  is the temperature, and  $m_H$  is the mass of the hydrogen atom. Equation 1.5 is often simplified to

$$\frac{dn_{H_2}}{dt} = \mathcal{R}_{gr} n_H n_{H_0} \quad (1.6)$$

by introducing a variable known as the formation rate,  $\mathcal{R}_{gr}$ , that is constrained using the column densities of CI, CII, HI,  $H_2$  (Krumholz, 2014). The column densities of CI and CII are used to determine a reaction rate by examining their ratios and the mechanisms that convert ions to atoms and atoms to ions. The neutralization of CII involves its interaction with polycyclic aromatic hydrocarbons, and the ionization of C takes place by interacting with far-ultraviolet (FUV) photons (Wolfire et al., 2008). The FUV intensity will also dictate the amount of dissociation of  $H_2$  into H, and by balancing the amount of CI and CII with the amount of H and  $H_2$ , the FUV intensity can be determined as well as the amount of  $H_2$  being produced (Wolfire et al., 2008). Typical reaction rates for the Milky Way have been found to be  $\mathcal{R}_{gr}=3 \times 10^{-17} \text{cm}^3 \text{s}^{-1}$  (Jura, 1975; Gry et al., 2002; Wolfire et al., 2008).

### 1.1.3 Dissociation of Molecular Hydrogen

When molecular hydrogen has formed, it is still susceptible to photodissociation from FUV photons. The energy required for a single photon to break the bonds of molecular hydrogen is 14.5 eV (Krumholz, 2014). Conveniently, this is also enough energy to excite atomic hydrogen, so photodissociation using a single photon is highly unlikely due to the abundance of HI in the ISM (Krumholz, 2014). However, a photon with an energy of 11-13.6 eV will not be able to ionize atomic hydrogen, but will be able to excite molecular hydrogen to its first and second excitation levels, the Lyman and Werner bands, respectively. The excited  $H_2$  will eventually settle via photon emission to its ground state with a finite probability of returning to two hydrogen atoms rather than maintaining its molecular state (Krumholz, 2014).

A dissociation rate,  $\zeta_{diss}$ , can be obtained by scaling the total excitation rate,  $\zeta_{exc}$ , by the fraction of excited hydrogen molecules that will settle to an atomic ground state (Krumholz, 2014). The total excitation rate is found by summing each individual excitation from the ground state e.g.  $\zeta_{exc,0-1}$ ,  $\zeta_{exc,0-2}$ . In the Milky Way's diffuse ISM, the interstellar radiation field is  $6.9 \times 10^{-14} \text{ erg cm}^{-3}$  over the range of 6-13.6 eV resulting in  $\zeta_{exc} \approx 3 \times 10^{-10} \text{ s}^{-1}$  (Draine, 2011). The expected fraction of  $H_2$  to dissociate is between 0.11 and 0.13 resulting in  $\zeta_{diss} \approx 4 \times 10^{-11} \text{ s}^{-1}$  (Draine, 2011). Equating the formation and dissociation rates and then solving for a molecular hydrogen to atomic hydrogen ratio gives

$$\begin{aligned}
\zeta_{diss} n_{H_2} &= \mathcal{R} n_{H_0} n_H \\
\frac{n_{H_2}}{n_H} &= \frac{\mathcal{R} n_{H_0}}{\zeta_{diss}} \\
&= 8 \times 10^{-6} \left( \frac{4 \times 10^{-11} s^{-1}}{\zeta_{diss}} \right) \left( \frac{n_{H_0}}{10 cm^{-3}} \right)
\end{aligned} \tag{1.7}$$

(Krumholz, 2014). From equation 1.7 we can see, in the diffuse medium, atomic hydrogen is far more abundant than molecular hydrogen, as expected.

However, as the density of the gas increases via collapse or coagulation, the optical depth will also increase, limiting the number of FUV photons able to penetrate into the core of the cloud, a process known as shielding which is the main factor in accelerating  $H_2$  production (Draine, 2011). This shielding will decrease the value of  $\zeta_{diss}$  which will increase the  $n_{H_2}/n_H$  ratio in equation 1.7. The increase in the molecular to atomic hydrogen ratio signifies the accumulation of molecular gas reservoirs. The molecular gas density will build up and lead to fragmentation within the cloud, and will eventually lead to star formation.

## 1.2 Determining the $H_2$ Abundance

From the previous section, the formation of molecular hydrogen will result in the energy released during formation to be absorbed by a dust grain while the other methods resulted in the emission of a photon to account for the change in energy. The absorption of energy by the dust grain as opposed to the energy being released through emission results in the formation of  $H_2$  being a dark process (§1.1.2). Furthermore, since the molecule is made of two



hydrogen atoms, its symmetry and low mass results in the molecule having no permanent dipole moment making low energy rotational transitions nonexistent (Bolatto et al., 2013; Kennicutt & Evans, 2012). The high symmetry and low mass does not mean  $H_2$  is unexcitable, but that the temperatures required to excite molecular hydrogen ( $T \gtrsim 100K$ ) are above the temperature of a typical GMC (Bolatto et al., 2013). Also the returning of  $H_2$  to the ground state will more often than not result in the molecule separating into two hydrogen atoms (§1.1.3). For our purposes, we can consider molecular hydrogen a dark molecule requiring special treatment to determine the amount present.

The amount of molecular hydrogen in a system can be calculated in several ways, and for the purpose of extragalactic sources they all involve using a molecular tracer to determine the amount of  $H_2$  present. The molecule most commonly used in extragalactic studies is CO due to its abundance and ability to be easily observed (Bolatto et al., 2013). Other tracers that have been used are CO's photodissociated counterpart, CII, in order to trace regions that have little to no CO emission (Madden et al., 1997), and molecules such as OH that have been used in the past but have been limited to Milky Way targets due to difficulty in observing OH (Barrett, 1964). The amount of CO can then be converted to  $H_2$  using a conversion factor given as either

$$n_{H_2} = X_{CO} I_{CO} \quad (1.8)$$

where  $n_{H_2}$  is the column density,  $X_{CO}$  is the conversion factor in units of  $cm^{-2} (K km s^{-1})^{-1}$ , and  $I_{CO}$  is the CO intensity in units of  $K km s^{-1}$ . Typical values for  $X_{CO}$  in normal spiral galaxies tend to be around  $1-4 \times 10^{20} cm^{-2} (K$

$\text{km s}^{-1})^{-1}$ , and a commonly used value for the Milky Way is  $2 \times 10^{20} \text{ cm}^{-2} (\text{K km s}^{-1})^{-1}$  (Bolatto et al., 2013). Alternatively, the conversion factor can be used to determine the surface density of the molecular hydrogen,  $\Sigma_{H_2}$ , using

$$\Sigma_{H_2} = \alpha_{CO} I_{CO} \quad (1.9)$$

where  $\alpha_{CO}$  is given in units of  $\text{M}_\odot \text{ pc}^{-2} (\text{K km s}^{-1})^{-1}$ . Values of  $\alpha_{CO}$  for nearby extragalactic sources have shown a mean value of  $3.1 \text{ M}_\odot \text{ pc}^{-2} (\text{K km s}^{-1})^{-1}$  which is slightly lower than the assumed Milky Way value of  $4.4 \text{ M}_\odot \text{ pc}^{-2} (\text{K km s}^{-1})^{-1}$  (Sandstrom et al., 2013).

### 1.2.1 Methods for Determining CO-to-H<sub>2</sub> Conversion Factor

Several methods are available to determine the conversion factor for extragalactic sources, and each has its own caveats. One common method used to determine the conversion factor is to use the virial nature of GMCs (Bolatto et al., 2013). The virial nature of GMCs implies that the clouds are gravitationally bound and not collapsing due the balance of the temperature of the cloud and amount of material present and the prevention of collapse can be aided by magnetic support (McKee & Ostriker, 2007). This method works best for well defined clouds; however in the case of more distant nearby galaxies, the issue of whether or not giant molecular associations (GMAs) display the same virialization as their constituent GMCs can limit concrete results (Bolatto et al., 2013). The second caveat to using the virial mass to determine the conversion factor is that the method will only trace CO bright regions.

Tracing only CO bright regions produces results that show no dependence between the conversion factor and metallicity, while other methods display a negative correlation between the conversion factor and metallicity (Bolatto et al., 2013). The lack of correlation with metallicity is believed to be due to the level of dust shielding present in the system. If the amount of dust present in the region is large, then the region will display a large metallicity, and if little to no dust is present, the region will show a low metallicity. Regions with low metallicity will correspond to regions with little to no dust resulting in poor shielding. The lack of shielding will allow the CO to be dissociated resulting in large amounts of self shielding molecular hydrogen traced by ionized and atomic carbon gas instead of CO (Bolatto et al., 2013). While the virial method is suitable for determining conversion factors within CO bright regions, excluding any low metallicity regions will underestimate the total amount of  $H_2$  present in the system as well as skew any possible relations of the conversion factor with metallicity (Bolatto et al., 2013).

A second method to determine the conversion factor is to incorporate observations of isotopologues of CO that are optically thin, commonly  $^{13}\text{CO}$  (Bolatto et al., 2013). The temperature, density, and column or surface density of  $^{13}\text{CO}$  can be used to constrain the physical conditions of the GMC or GMA being examined. The main problem with using this method is the degeneracy between the temperature and density of CO emission such that hot low density regions can resemble cool dense regions (Rosenberg et al., 2014). This method also shares the same problem as the virial technique in that it only probes CO bright regions of the target leaving any CO-faint  $H_2$  gas untraced (Bolatto et al., 2013). The issue of CO-faint molecular hydrogen has

been examined using the photodissociated tracer of CO, CII, instead of  $^{13}\text{CO}$ . The CII ion was used as a tracer of molecular hydrogen in dwarf galaxies and revealed large reservoirs of self-shielding  $\text{H}_2$  (Madden et al., 1997).

The third way to determine the CO-to- $\text{H}_2$  conversion factor is by incorporating the emission from dust to determine the amount of molecular gas present. This method assumes that the gas is well mixed and has a constant ratio of dust mass to gas mass present in the galaxy (Leroy et al., 2011), which has been shown to be true for the Milky Way (Boulanger et al., 1996). A suitable conversion factor is found by solving

$$\begin{aligned}\delta_{GDR}\Sigma_{dust} &= \Sigma_{\text{H}_2} + \Sigma_{\text{HI}} \\ &= \alpha_{\text{CO}}I_{\text{CO}} + \Sigma_{\text{HI}}\end{aligned}\tag{1.10}$$

where  $\Sigma_{dust}$ ,  $\Sigma_{\text{H}_2}$ , and  $\Sigma_{\text{HI}}$  are the respective surface densities in  $\text{M}_\odot \text{ pc}^{-2}$ ,  $I_{\text{CO}}$  is the CO line intensity,  $\alpha_{\text{CO}}$  is the conversion factor in  $\text{M}_\odot \text{ pc}^{-2} \text{ K}^{-1} \text{ km}^{-1} \text{ s}$ , and  $\delta_{GDR}$  is the total mass of the gas divided by the total mass of the dust known as the gas-to-dust ratio (Leroy et al., 2011; Sandstrom et al., 2013). In equation 1.10, we can measure  $\Sigma_{dust}$ ,  $\Sigma_{\text{HI}}$ , and  $I_{\text{CO}}$  leaving only the conversion factor and gas-to-dust ratio free to vary. An appropriate  $\alpha_{\text{CO}}$  value will generate a molecular gas mass that produces a constant gas-to-dust ratio over the galaxy being studied. This method has been carried out extensively by Sandstrom et al. (2013) on kpc scales on nearby galaxies as well as on both of the Magellanic clouds by Leroy et al. (2011).

Determining a conversion factor via the dust emission provides the capability to trace the CO faint regions of a target (Israel et al., 1996). Despite

this advantage over the other two methods, using equation 1.10 leaves any gas not associated with atomic hydrogen to be treated as  $H_2$ . This is shown in equation 1.10 given that the total amount of gas, is  $\alpha_{CO}I_{CO} + \Sigma_{HI}$ , so any gas not associated with atomic hydrogen is assumed to be molecular hydrogen. This means that the calculated amount of  $H_2$  will include contributions from CO, OH, and CII as well as any other chemical species present in the region. This will effectively increase the conversion factor and the overall amount of molecular hydrogen reported (Bolatto et al., 2013), but given the dominance of  $H_2$  in the dense regions of the ISM, any increase will be negligible. Another caveat of this method rests with the assumption of a constant dust-to-gas ratio (Bolatto et al., 2013). Issues such as the gas-to-dust ratio's dependence on metallicity (Draine et al., 2007) can render this assumption null if not treated properly. Nevertheless, the agreement of conversion factors between the dust based method and other methods used for more local targets suggests that any gas present that has been incorrectly assumed to be  $H_2$  and local fluctuations in the metallicity of the target galaxy have very little effect on the final results (Bolatto et al., 2013).

### 1.3 Determining Dust Mass

Calculating a conversion factor using dust emission requires a knowledge of the amount of dust present in our system to determine a gas-to-dust ratio. Given that a significant portion of the dust mass lies within the cold phase we can calculate a dust mass using a modified blackbody fit over the cold portion of the dust's spectral energy distribution (SED) (Galametz et al., 2012). A

slight modification needs to be introduced to our blackbody resulting in what is known as a greybody or modified blackbody (MBB). The modification is necessary because the dust does not absorb and re-emit all of the light incident on its surface. If we assume an isolated optically thin medium ( $\tau_\nu \ll 1$ ) with a blackbody source function,  $B_\nu(T)$ , the radiative transfer equation can be written as

$$I_\nu = (1 - e^{-\tau}) B_\nu(T), \quad (1.11)$$

and simplified using a first order Taylor expansion with  $\tau_\nu \ll 1$  to get

$$I_\nu = \tau_\nu B_\nu(T) \quad (1.12)$$

The optical depth can be expanded to incorporate the surface density of the dust,  $\Sigma_{dust}$ , as

$$\tau_\nu = \kappa_\nu \Sigma_{dust} \quad (1.13)$$

such that the units on  $\Sigma_{dust}$  are in  $\text{kg m}^{-2}$  as opposed to  $\text{M}_\odot \text{ pc}^{-2}$ . The dust emissivity cross-section per unit mass is represented by  $\kappa_\nu$  and is often referred to as the opacity. The opacity will reflect the chemical makeup and grain structure of the dust, but will not indicate the grain size (Abergel et al., 2013). The behavior of the opacity has been well fit with a power law such that opacity shows a dependence on the frequency of the observed emission (Hildebrand, 1983). The opacity is typically written as

$$\kappa_\nu = \kappa_{\nu,0} \left( \frac{\nu}{\nu_0} \right)^\beta \quad (1.14)$$

where  $\nu_0$  is a reference frequency,  $\kappa_{\nu,0}$  is a reference opacity based on the reference frequency, and  $\beta$  is the dust emissivity index. Values for  $\kappa_\nu$  have been calculated for several models of varying dust compositions and can range from 0.2 to 2 m<sup>2</sup> kg<sup>-1</sup> over the wavelengths used to model the cold component (100 $\mu$ m–850 $\mu$ m)(Li & Draine, 2001). The emissivity index has commonly been fit between ranges of 1.0 to 2.0 suggested from laboratory experiments (Walcher et al., 2011). However, with the influx of Herschel data the ability to fill in the sub-millimeter portion of the SED between 100 $\mu$ m and 500 $\mu$ m has allowed the emissivity index to be determined based on observations, which have shown a range from 1 to 2.5 (Galametz et al., 2012). It should be noted that the lower limit of  $\beta=1$  is a hard cutoff due to limits determined by the Kramers-Kronig relationship in the optically thin case (Li, 2005), but in extreme instances when the dust becomes optically thick  $\beta$  will approach 0.

With the opacity well defined, substituting equation 1.14 into equation 1.13 and then into the original equation for the specific intensity of our MBB, equation 1.12, gives the formula for the specific intensity of a greybody as

$$I_\nu = \Sigma_{dust} \kappa_{\nu,0} \left( \frac{\nu}{\nu_0} \right)^\beta B_\nu(T) \quad (1.15)$$

Since we measure the flux of our target, it is useful to convert from the specific intensity to the flux using

$$F_\nu = \pi I_\nu \left( \frac{r}{D} \right)^2 \quad (1.16)$$

given the target is a uniform sphere with radius,  $r$ , and distance,  $D$  (Rybicki & Lightman, 1986). Substituting equation 1.16 into the greybody equation, 1.15, gives

$$S_\nu = \frac{\Sigma_{dust} \pi r^2}{D^2} \kappa_\nu \left( \frac{\nu}{\nu_0} \right)^\beta B_\nu(T). \quad (1.17)$$

Converting from surface density to overall mass is done using the relationship between mass and surface density of  $M = \Sigma * \text{Area}$  where the target's projected area is  $\pi r^2$ . This gives a final modified blackbody equation of

$$S_\nu = \frac{M_{dust}}{D^2} \kappa_\nu \left( \frac{\nu}{\nu_0} \right)^\beta B_\nu(T). \quad (1.18)$$

The dust mass can be solved from equation 1.18 by fitting the dust mass, temperature, and possibly the emissivity index. The fitted mass will act as a normalizing factor for the SED and correspond with the mass associated with the peak flux. The fitted dust mass should be used cautiously due to a sensitivity in mass with temperature fluctuations (Draine et al., 2007). An alternative to using the fitted mass is to isolate the mass from equation 1.18 to get

$$M_{dust} = \frac{S_\nu D^2}{\kappa_\nu B_\nu(T)} \left( \frac{\nu}{\nu_0} \right)^{-\beta} \quad (1.19)$$



and use the parameters returned from fitting. This equation is best used with a longer wavelength observation that will explore the Rayleigh-Jeans tail of the modified blackbody. This portion of the SED will see less of a dependence on the mass and temperature fluctuations (Draine et al., 2007). The main concern with both methods to determine the mass arises from fitting both the temperature and dust emissivity index and their strong anti-correlation (Galametz et al., 2012; Tabatabaei et al., 2014). A common method to help break the degeneracy is to fix the emissivity index to a reasonable value based upon the opacity model (Tabatabaei et al., 2014).

## 1.4 NGC 3627

In this thesis, we are using the new SCUBA-2 instrumentation on the JCMT, which observes both  $450\mu\text{m}$  and  $850\mu\text{m}$  emission simultaneously. Utilizing multiple 60 minute scans in high quality weather we can better constrain the emissivity index in our fits, as well as increase the resolution compared to previous work. With these new observations from the NGLS, we can better fit an SED and determine a more reliable dust mass to explore the amount of molecular gas present. To take full advantage of the benefits of SCUBA-2, we have selected the target NGC3627 for its relatively small angular size, pronounced spiral features, and relatively large flux.

NGC 3627 is the most prominent member of the interacting trio of galaxies called the Leo triplet (NGC 3623, NGC 3627, and NGC3628). An optical image is shown in Figure 1.1 while the data we used can be seen in sections §2.2 and §2.3. The interaction between NGC 3627 and NGC 3628 has been well

documented via HI emission in the form of a large HI debris tail extending from NGC 3628 in the direction of NGC 3627 (Rots, 1978; Haynes et al., 1979). The interaction between these galaxies has resulted in a high star formation rate of over  $1.7 \text{ M}_{\odot} \text{ yr}^{-1}$  (Calzetti et al., 2010), making NGC 3627 a prime candidate to study the current star forming conditions. The morphology of NGC 3627 is that of a barred spiral (SABb) with an inclination of  $60^{\circ}$  (Reuter et al., 1996) at a distance of 9.4 Mpc determined by Cepheid variable observations (Freedman et al., 2001). Furthermore, the strong spiral arm features of this galaxy are unique due to speculation that they are not contained within the plane of the galaxy (Dumke et al., 2011; Soida et al., 2001). This interpretation is supported by magnetic field lines traced by dust polarization that do not trace the spiral structure in the southeastern bar end (Soida et al., 2001) and CO observation with bimodal emission features in velocity space over the southeastern bar end (Dumke et al., 2011).

NGC 3627 was observed as part of the Spitzer Infrared Nearby Galaxies Survey (SINGS) (Kennicutt et al., 2003) and has been observed throughout the electromagnetic spectrum.  $^{13}\text{CO}$  observations by Watanabe et al. (2011) have shown that a majority of the star formation is occurring in the bar ends. This information agrees with Warren et al. (2010) showing the star formation efficiency being highest in the bar ends. Warren et al. (2010) also show the ISM of the galaxy to be dominated by molecular gas, with dense warm gas dominating the emission at the bar ends, the nucleus and a bright region located beneath the southwestern spiral arm, and more diffuse and cooler molecular gas outside of these regions. The atomic gas is located primarily in the spiral arms with little to no emission in the nucleus of the galaxy.

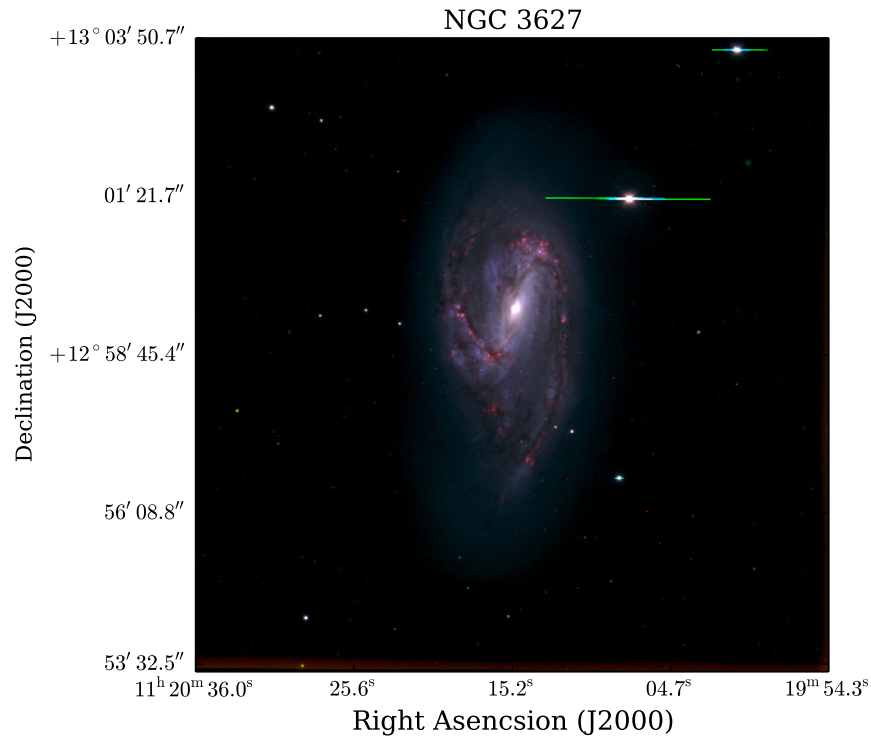


Figure 1.1: Optical composite image of NGC3627 made using the SINGS 5<sup>th</sup> enhanced data release (Kennicutt et al., 2003). Blue areas represent the B band, green areas represent V band and red areas show the H $\alpha$  band. Component images were retrieved from NED.

A mean conversion factor of  $\alpha_{CO}=1.2 \text{ M}_{\odot} \text{ pc}^{-2} (\text{K km s}^{-1})^{-1}$  was found by Sandstrom et al. (2013) using the dust method (§1.2.1). An HI mass was given as  $8.18 \times 10^8 \text{ M}_{\odot}$  (Walter et al., 2008), and a corresponding  $\text{H}_2$  mass was calculated as  $5.79 \times 10^9 \text{ M}_{\odot}$  (Kennicutt et al., 2003), and a stellar mass of  $2.8 \times 10^{10} \text{ M}_{\odot}$  (Skibba et al., 2011). Comparing the properties of NGC3627 to local galaxies, we see a more gas rich system than M33 whose total hydrogen mass is  $\approx 2 \times 10^9 \text{ M}_{\odot}$  (Braine et al., 2010), and a lower stellar mass than the Milky Way which has been calculated to be  $\approx 6 \times 10^{10} \text{ M}_{\odot}$  (McMillan, 2011).

The dust emission of NGC 3627 follows the same trend as the CO emission with the brightest regions at the bar ends, nucleus, and a bright region below the southwest bar end. The southeastern spiral arm shows some knotted features in the dust emission. Global values for the cold and warm components of the SED were fit by Galametz et al. (2012) and reveal dust temperatures of  $T_W=55.8 \pm 5.6 \text{ K}$  and  $T_C=20.2 \pm 1.4 \text{ K}$  for the warm and cold components, respectively, with a best fit emissivity index of  $\beta=2.3 \pm 0.2$  and a total dust mass of  $7.82 \times 10^7 \text{ M}_{\odot}$ .

This thesis will explore the properties of dust emission from NGC3627 by exploring its SED using new observations from SCUBA-2 in order to measure the mass and dust emissivity index at a higher resolution in order to build on the work of Galametz et al. (2012). Furthermore, we can use our SED derived dust masses to determine the overall amount of molecular gas present in the galaxy while gaining insight into the dust-to-gas ratio and conversion factor for this galaxy using the methods outlined by Leroy et al. (2009) and Sandstrom et al. (2013). The information in this thesis is arranged as follows: Chapter

2 will describe the data reduction and properties of the SCUBA-2 data and any ancillary data, Chapter 3 will describe the SED fitting method, Chapter 4 will include the results from the dust-to-gas ratio analysis, and Chapter 5 will summarize our findings.

## Chapter 2

# Observations and Data Preparation

### 2.1 SCUBA-2

The Submillimetre Common-User Bolometer Array 2 (SCUBA-2) was designed to decrease the observing time of the sub-millimeter sky relative to its predecessor SCUBA (Holland et al., 2013). This would benefit the community by allowing for rapid data acquisition in the submillimeter regime of the electromagnetic spectrum, at the  $450\mu\text{m}$  and  $850\mu\text{m}$  bands in particular. Prior to SCUBA-2, other bolometer cameras such as LABOCA, BOLOCAM and SHARC-II were limited to less than 100 pixels, while the new SCUBA-2 has been able to incorporate over 10,000 pixels in its design and effectively reduce the required observing time (Chapin et al., 2013). Increasing the number of pixels by a factor of 100 was possible by the advent of new technology such as high precision micromachining, superconducting transition edge sensors, and superconducting quantum interference device amplifiers (SQUIDs) (Holland et al., 2013).

The observations of NGC3627 were taken from the Nearby Galaxies Legacy Survey’s (NGLS) initial science images using SCUBA-2 from December 29, 2011 to January 21, 2012, and consist of 24  $18'$  by  $18'$  scans taken in weather conditions where the optical depth of the water in the atmosphere is no greater than  $\tau < 0.13$ . The observations were centered at  $450\mu\text{m}$  and  $850\mu\text{m}$  emission with a  $32\mu\text{m}$  and  $85\mu\text{m}$  bandpass, respectively. 16 of the 24 scans were deemed useable, and whether or not an observation was deemed worthwhile was determined by factors such as the behavior of the image background or whether the image was flagged during observing to be unusable. The observations of NGC3627 were taken using a DAISY scanning pattern to help remove any random noise by introducing crossing points. The scanning speed of the JCMT was  $150''/\text{second}$  in order to reduce any drifting effects seen from the instrument or sky (Chapin et al., 2013).

## 2.2 Image Creation and Properties

For any imaging process to be successful, the final image needs to have minimal white noise (Chapin et al., 2013). White noise in our bolometer observations arises from thermal variations from the instrumentation and atmosphere during data acquisition and is referred to as random noise during the image creation. The random noise is minimized through scanning methods and during image processing (Chapin et al., 2013). To create the final SCUBA-2 data products, we use the Submillimetre User Reduction Facility (SMURF) procedure MAKEMAP. This procedure reduces the noise of the observations while maintaining the source’s emission by incorporating a combination reduc-

tion techniques, one of which principal component analysis which will remove any correlated signal and is useful in detecting point sources (Chapin et al., 2013). The second method is a maximum likelihood analysis that will invert the time series of the data then apply a variety of weights to minimize the variance in the inverted time series (Janssen & Gulkis, 1992; Chapin et al., 2013). Both of these methods have proven useful in reducing bolometer data on their own, but due to the size of raw SCUBA-2 data, either method on its own would result in extreme run times or the process becoming resource intensive (Chapin et al., 2013).

MAKEMAP breaks down the image creation into several steps performed in iteration in order to successfully reduce any background noise (Chapin et al., 2013). The raw data is modeled by

$$b_i(t) = f [e_i(t) * a_i(t) + g_i * n_c(t) + n_f(t) + n_r(t)] \quad (2.1)$$

such that  $b_i(t)$  is the  $i^{th}$  bolometer output at time  $t$ ,  $f$  is a scaling factor determined from flat field calibrations,  $e_i(t)$  is the extinction at time  $t$  for the  $i^{th}$  bolometer,  $a_i(t)$  is the astronomical signal for  $i^{th}$  bolometer at time  $t$ ,  $g_i * n_c(t)$  is the noise due to the product of the common mode and gain,  $n_f(t)$  is the low-frequency noise, and  $n_r(t)$  is the random noise from the atmosphere or thermal variations in the equipment (Chapin et al., 2013).

The steps used in MAKEMAP are designed so they can estimate each noise component of the bolometer signal. The COM and GAI steps estimate a common mode signal by fitting the average time-series of each bolometer observation. The next step is EXT, which is used to apply the measured ex-



inction corrections. Following EXT is FLT to apply high- and low-pass filters to remove any noise features not removed in the COM and GAI filtering. After the high- and low-pass filters, the AST step is performed. AST converts the data from a time series to an image and detects sources to be removed from reduction. The sources removed during this portion of MAKEMAP are intended to be astronomical in nature. The final step is NOI which determines the noise in the gridded map after each step has been performed and is calculated by isolating the white noise component in equation 2.1. A convergence check is then done based on the magnitude of change in each pixel from the previous map and the current version. If the check fails, the COM, GAI, EXT, and FLT values are recalculated using the AST information obtained from the previous iteration, and the process is repeated until the convergence values are met or the maximum number of iterations has been carried out (Chapin et al., 2013). A diagram of the steps is shown in Figure 2.1 inspired by the flowchart in Chapin et al. (2013). Creating the data was done locally using scripts to implement MAKEMAP.

In our production of maps, we used the configuration file `dimconfig_bright_compact.lis` and altered the AST and FLT sections of the image creation by introducing a mask made from Herschel’s  $250\mu\text{m}$  map. The purpose of the mask was to exclude the target from interfering with the noise minimization as well as to keep any emission from the galaxy from being significantly altered during image production. The filter size of the high-pass filter was also modified, and an appropriate value was determined to be  $175''$ . We determined an appropriate high-pass filter size by running a large range of filters from  $100''$  to  $300''$  and inspecting the total recovered flux of NGC3627. A plot of the

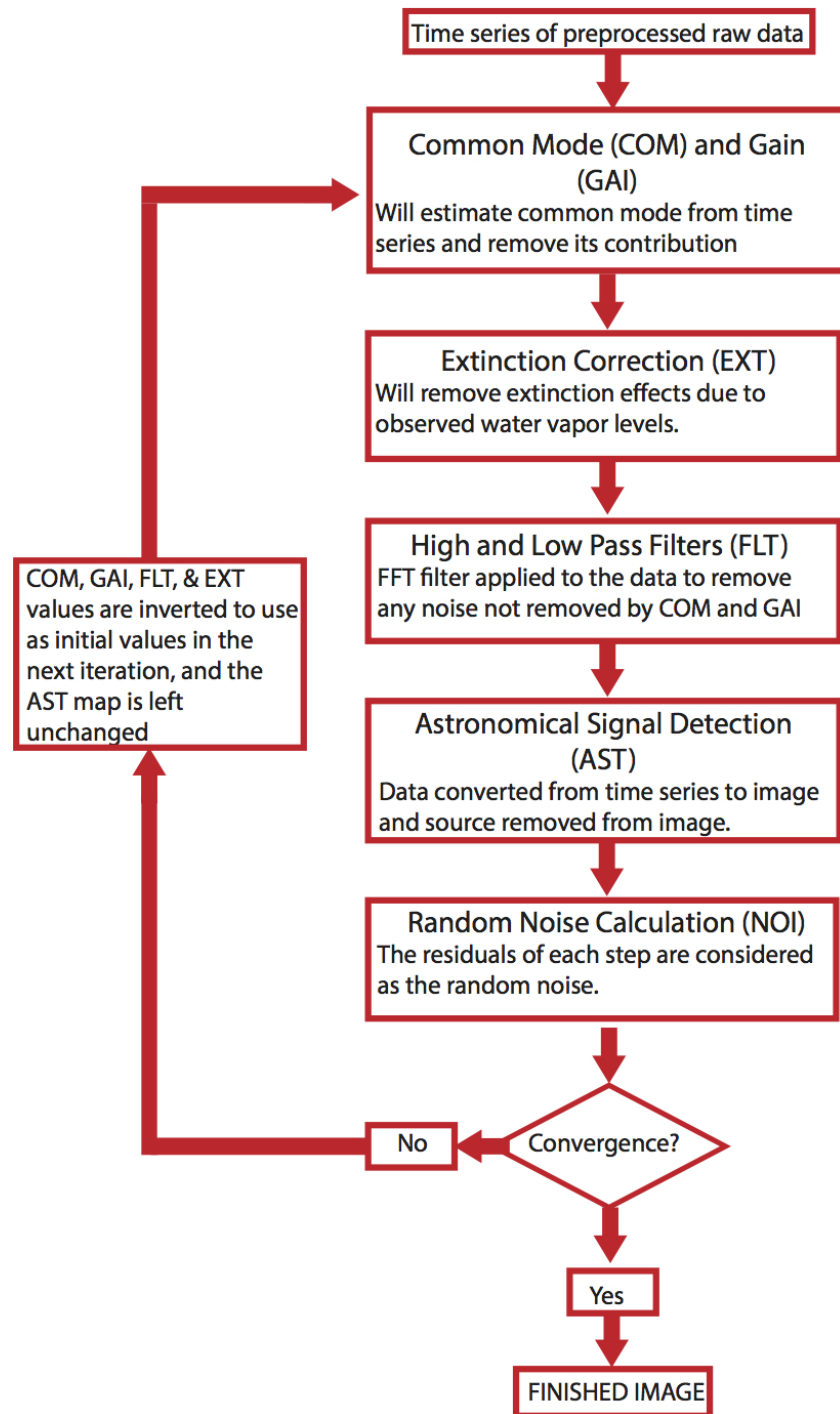


Figure 2.1: The iterative steps taken to create SCUBA-2 data using MAKEMAP. Inspired by the diagram in Chapin et al. (2013).

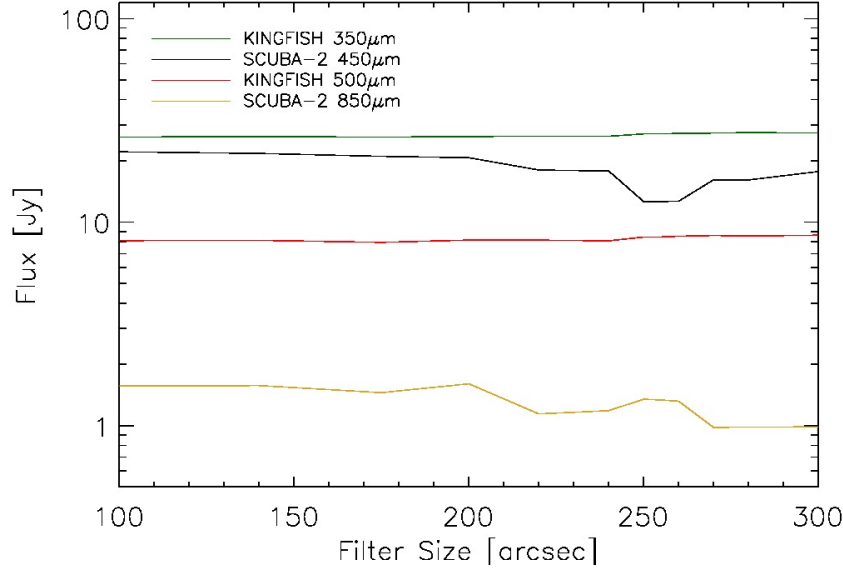


Figure 2.2: Returned flux values for NGC3627 with varying high-pass filter sizes. The KINGFISH fluxes have been processed using the fakesource process, §2.4.2

returned flux values can be seen in Figure 2.2. A good filter would not show any significant decrease in flux compared to the  $350\mu\text{m}$  or  $500\mu\text{m}$  fluxes. This requirement removes any filters greater than  $200''$ . Given the flux was nearly constant with filters less than  $200''$ , we chose an appropriate filter size by examining the structure that was returned, in particular how well the spiral arms were recovered for the  $850\mu\text{m}$  image, and how well the disk was preserved in the  $450\mu\text{m}$  image. The spatial effect of the filters can be seen in Figure 2.3 for  $450\mu\text{m}$  and Figure 2.4 for  $850\mu\text{m}$ . The maps were returned from MAKEMAP in units of pW with a pixel size of  $2''$  by  $2''$  for both the  $450\mu\text{m}$  and  $850\mu\text{m}$ .

The final  $450\mu\text{m}$  image was then re-gridded down to a  $4''$  by  $4''$  pixel grid, and flux calibration values of 491000 and 4710 (Dempsey et al., 2013) were applied to convert from pW to mJy/beam and mJy/square arcsecond, respec-

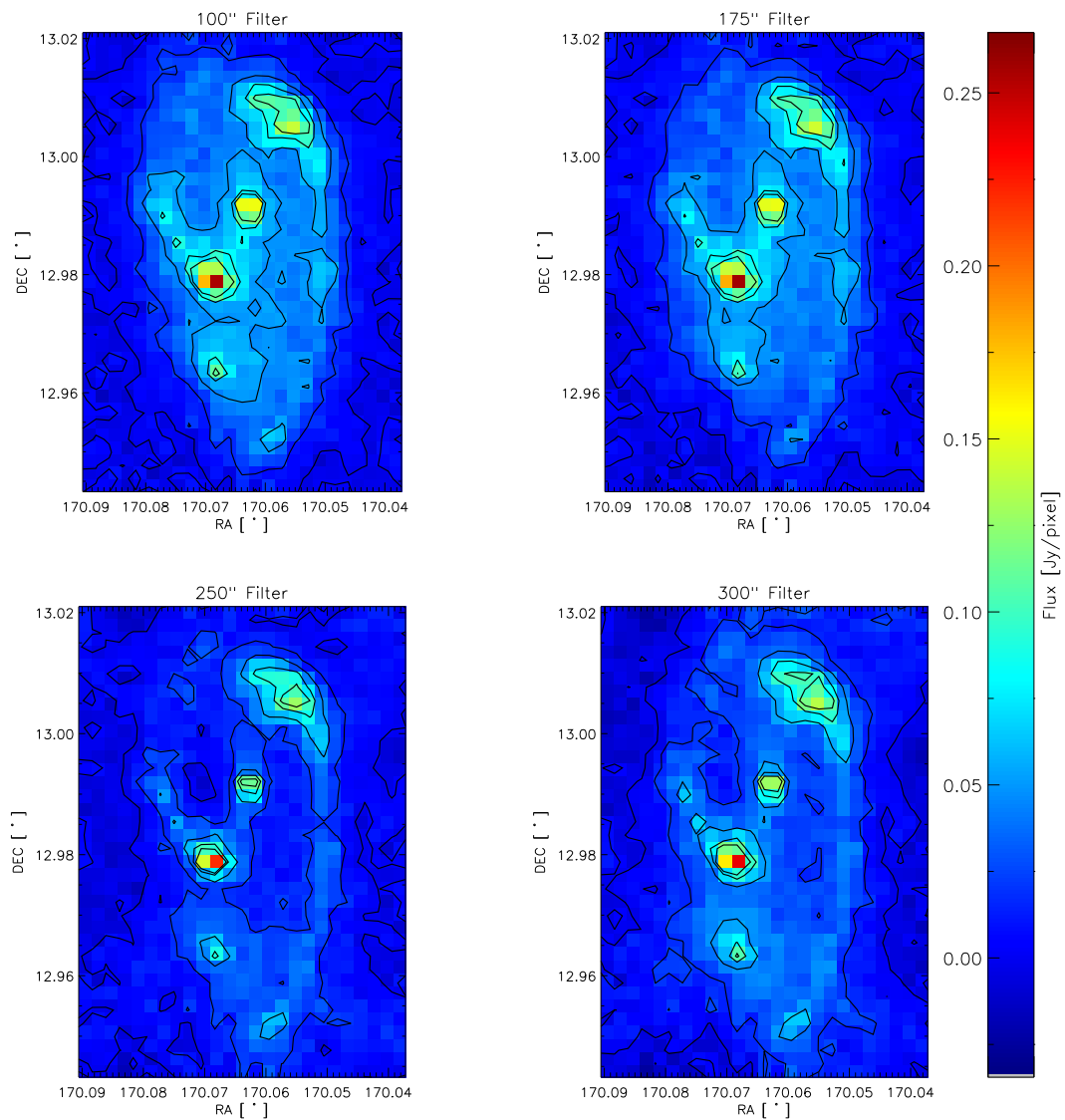


Figure 2.3: Four 450  $\mu\text{m}$  maps of NGC3627 using varying high-pass filter sizes. The contours shown are for 0.0, 0.02, 0.05, 0.08 and 0.1 Jy/pixel for each image with 8'' by 8'' pixels.

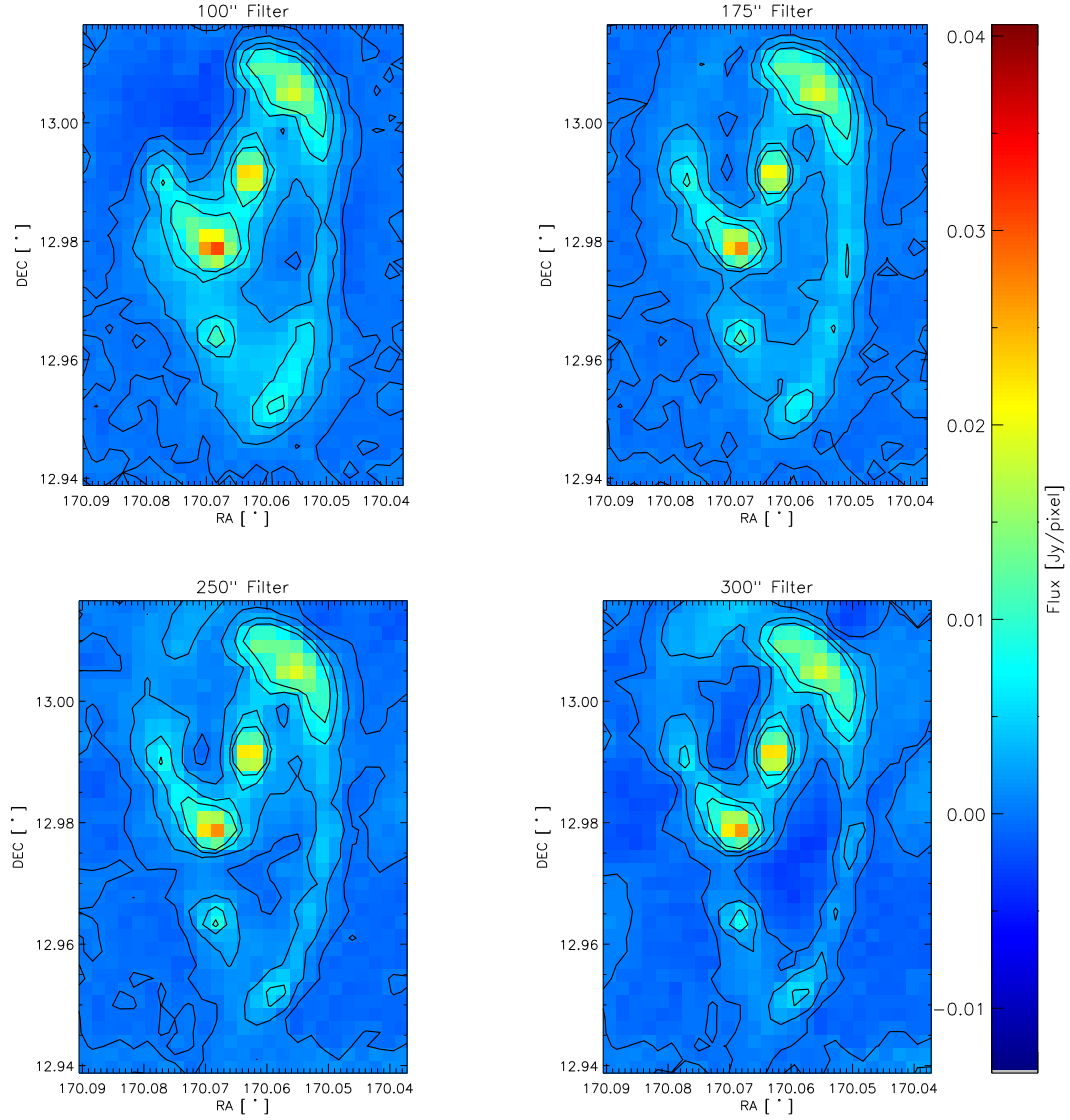


Figure 2.4: Four 850  $\mu\text{m}$  maps of NGC3627 using varying high-pass filter sizes. The contours shown are for 0.0, 0.002, 0.005, and 0.008 Jy/pixel for each image with 8'' by 8'' pixels.

Table 2.1. Properties of NGC3627 SCUBA-2 Observations

Observation	Beam Properties				[mJy/beam]
	Main Beam Amplitude	Main Beam FWHM	Error Beam Amplitude	Error Beam FWHM	
450 $\mu$ m	$0.854 \pm 0.002$	$7.48'' \pm 0.03''$	$0.146 \pm 0.003$	$23.1'' \pm 0.2''$	
850 $\mu$ m	$0.9624 \pm 0.0002$	$12.8'' \pm 0.004''$	$0.0376 \pm 0.0002$	$44.5'' \pm 0.09''$	

tively. The 850 $\mu$ m maps were re-gridded to an 8'' by 8'' pixel size and used flux calibration values of 537000 and 2340 for mJy/beam and mJy/square arc-second (Dempsey et al., 2013). The 4'' and 8'' pixels correspond to a 180pc and 360pc size scale for our target, NGC3627. To simplify the analysis, the images are also converted to Jy/pixel. The 450 $\mu$ m and 850 $\mu$ m images are shown in Figures 2.5 and 2.6. The calibration values used are the default flux calibration factors that are determined from our calibrator source, Uranus, in (Dempsey et al., 2013). The overall noise in the final image can be seen in Table 2.1.

### 2.2.1 Beam Shape of the 450 $\mu$ m and 850 $\mu$ m Data

Calibration images of Uranus were used to determine the shape of the beam for the 450 $\mu$ m and 850 $\mu$ m observations. The beam shape of both the 450 $\mu$ m and 850 $\mu$ m maps deviates from a single gaussian due to the second maximum of the airy diffraction pattern in the response function of the telescope and minor imperfections in the mirror of the JCMT due to boundaries of the panels (Dempsey et al., 2013). This abnormality is best represented by a sum of two gaussians whose amplitudes sum to unity (Dempsey et al., 2013). The

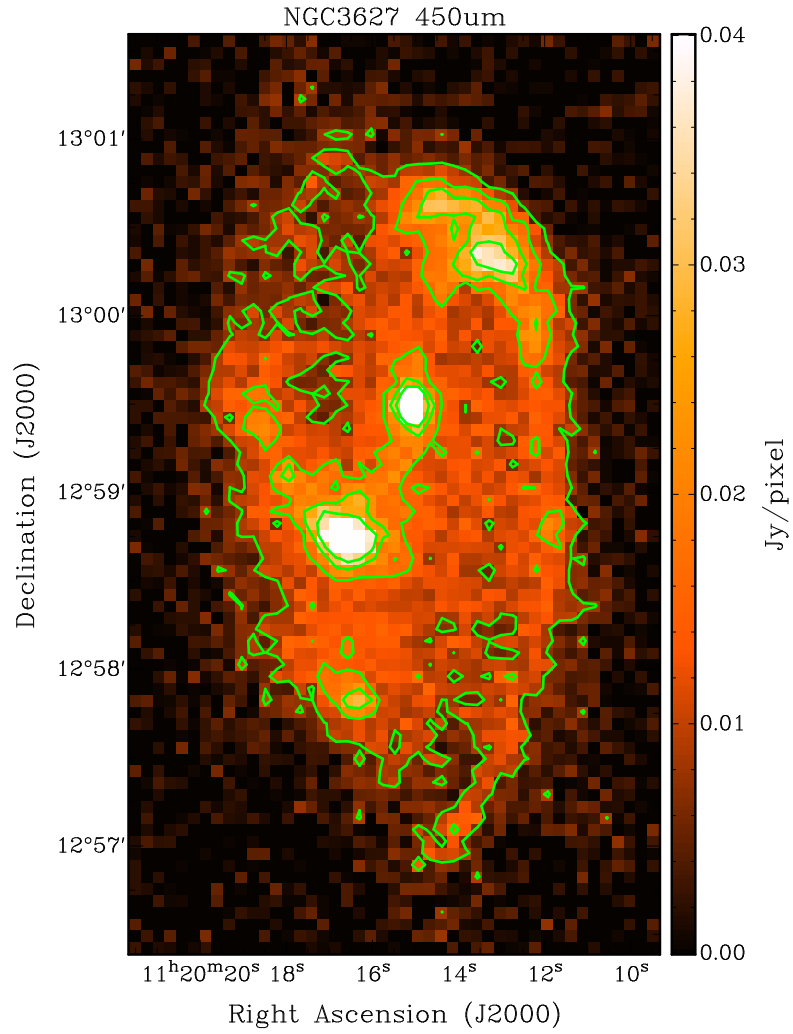


Figure 2.5: 450 $\mu$ m observation produced at the end of the image production with 20%, 40%, 60%, and 80% contours with 4'' by 4'' pixels.

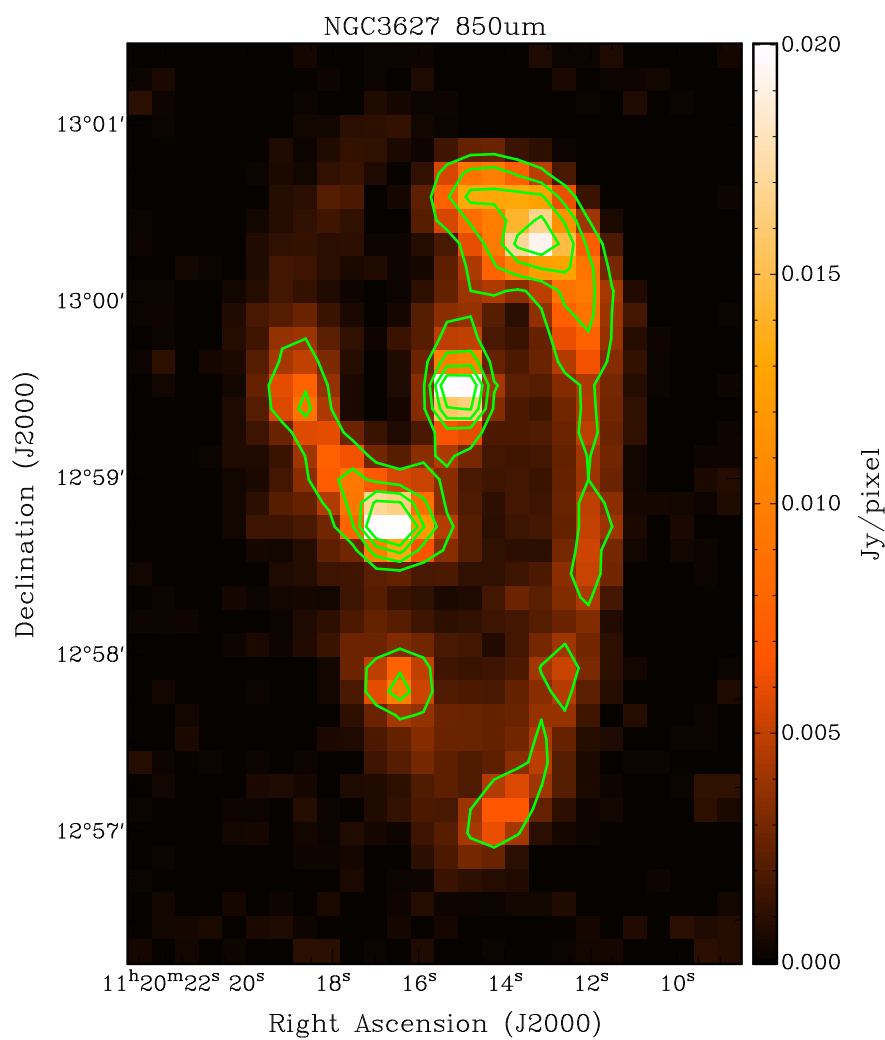


Figure 2.6:  $850\mu\text{m}$  observation produced at the end of the image production with 20%, 40%, 60%, and 80% contours with  $8''$  by  $8''$  pixels.



average beam resolutions for the  $450\mu\text{m}$  and  $850\mu\text{m}$  data are reported in Table 2.1 and are within an acceptable difference from the values found in Dempsey et al. (2013) since we used only the nights our data was taken compared to the work done by Dempsey et al. (2013) that used observations taken over a year. The calibration images, fitted beams, and the residual of the fits can be seen in Figure 2.7. The residuals seen in here are due to asymmetries in the Uranus PSF. The contribution of the error beam in the  $850\mu\text{m}$  emission is negligible, and allows the beam to be approximated by a single gaussian. However, the contribution of the error beam in the  $450\mu\text{m}$  images was large enough to require special treatment in order to properly match the beams for analysis.

## 2.3 Ancillary Data

The scientific goals of this thesis require data outside the capabilities of SCUBA-2. For instance, accurately determining the dust mass involves fitting the spectral energy distribution (SED) for NGC3627. To successfully fit an SED, we need shorter wavelength data to fully probe the cold component of this galaxy. We used data ranging from  $100\mu\text{m}$  to  $500\mu\text{m}$  from the KINGFISH survey (Kennicutt et al., 2011) to gain a large enough wavelength range for fitting the cold component. Secondly, the bandpass of the  $850\mu\text{m}$  filter contains the CO J=3-2 line. In order to get a valid measurement of the dust mass, this contribution had to be removed. We used emission data from the NGLS from the HARP instrument on the JCMT (Wilson et al., 2012) to remove this contamination. When a dust mass was obtained, we used CO J=1-0 from the

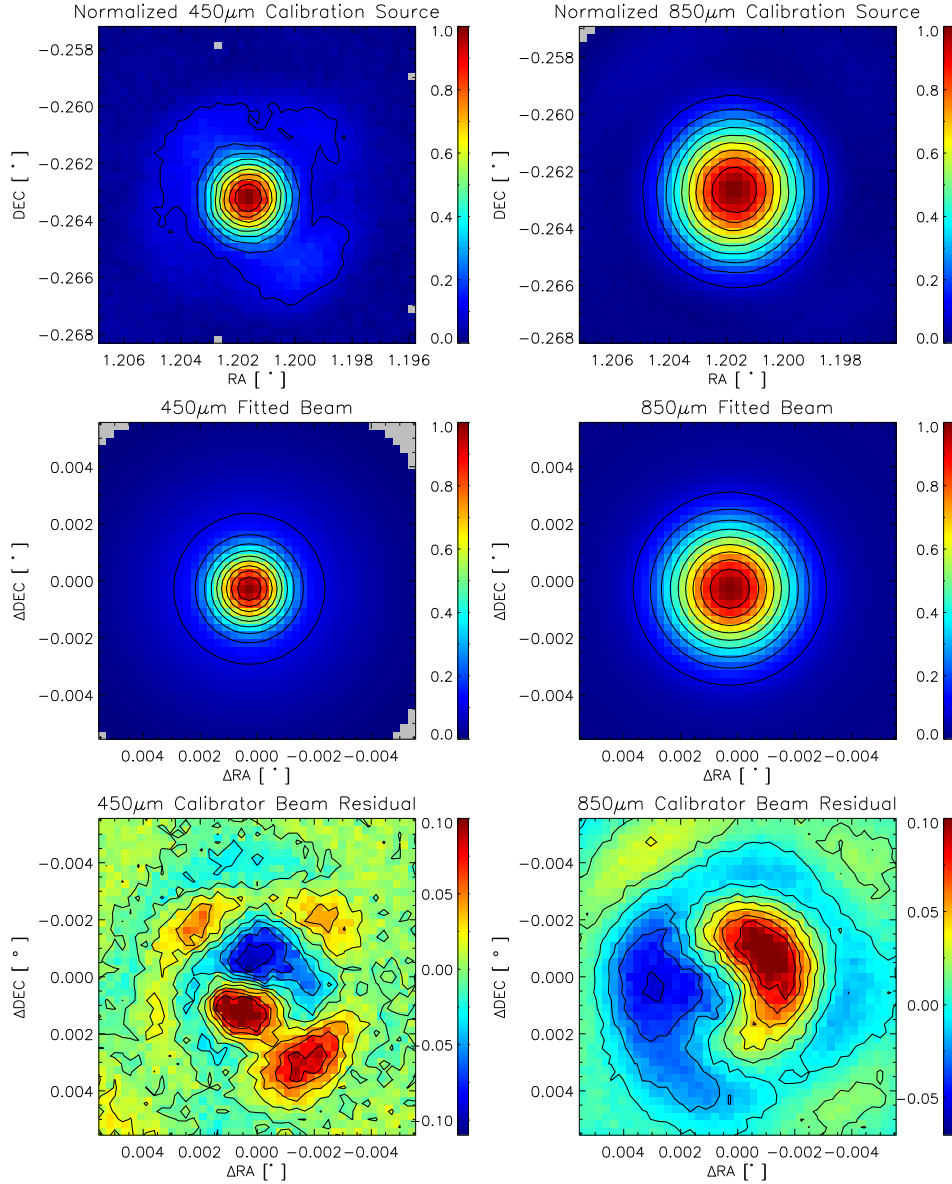


Figure 2.7: The top row shows the Uranus images taken on January, 8th 2012 for 450 $\mu$ m on the left and 850 $\mu$ m on the right. The middle row shows the fitted beams for 450 $\mu$ m on the right and 850 $\mu$ m on the left using the double gaussian beam shape. The bottom row shows the difference between the original image and the fitted beam. The contours in the image are from 10% to 90% in intervals of 10%.

Nobeyama 45-m telescope (Kuno et al., 2007), CO J=2-1 from HERACLES (Leroy et al., 2009), and *HI* observations from THINGS (Walter et al., 2008) to determine a reasonable molecular hydrogen mass to calculate a dust-to-gas ratio. In the next sections we give some details for these ancillary data sets.

### 2.3.1 Key Insights on Nearby Galaxies: a Far-Infrared Survey with Herschel (KINGFISH)

The Key Insights on Nearby Galaxies: a Far-Infrared Survey with Herschel (KINGSFISH) was designed to be a follow up to the Spitzer Infrared Nearby Galaxies Survey (SINGS) (Kennicutt et al., 2003) with observations of the warm and cold component of dust emission using the increased resolution from Herschel (Kennicutt et al., 2011). The main science goals of the KINGFISH survey were to better understand the star formation processes that were shielded by dust, to make resolved studies of heating and cooling of the interstellar medium (ISM), and to build an inventory of how cold dust emission relates to other dust components in the ISM (Kennicutt et al., 2011). The survey consists of 61 nearby galaxies ( $d < 30 \text{ Mpc}$ ) that cover a range of environments. Each target was observed at  $70 \mu\text{m}$ ,  $100 \mu\text{m}$ ,  $160 \mu\text{m}$ ,  $250 \mu\text{m}$ ,  $350 \mu\text{m}$ , and  $500 \mu\text{m}$ . Our analysis focuses on fitting the cold component of NGC3627's SED, so we omitted the  $70 \mu\text{m}$  emission from the fitting, and processed the data through MAKEMAP as described below in § 2.4. The rms and beam size after the large scale structure has been removed can be seen in Table 2.2 given for  $8''$  by  $8''$  pixels, while the preconvolved maps are shown in Figures 2.8 to 2.12.

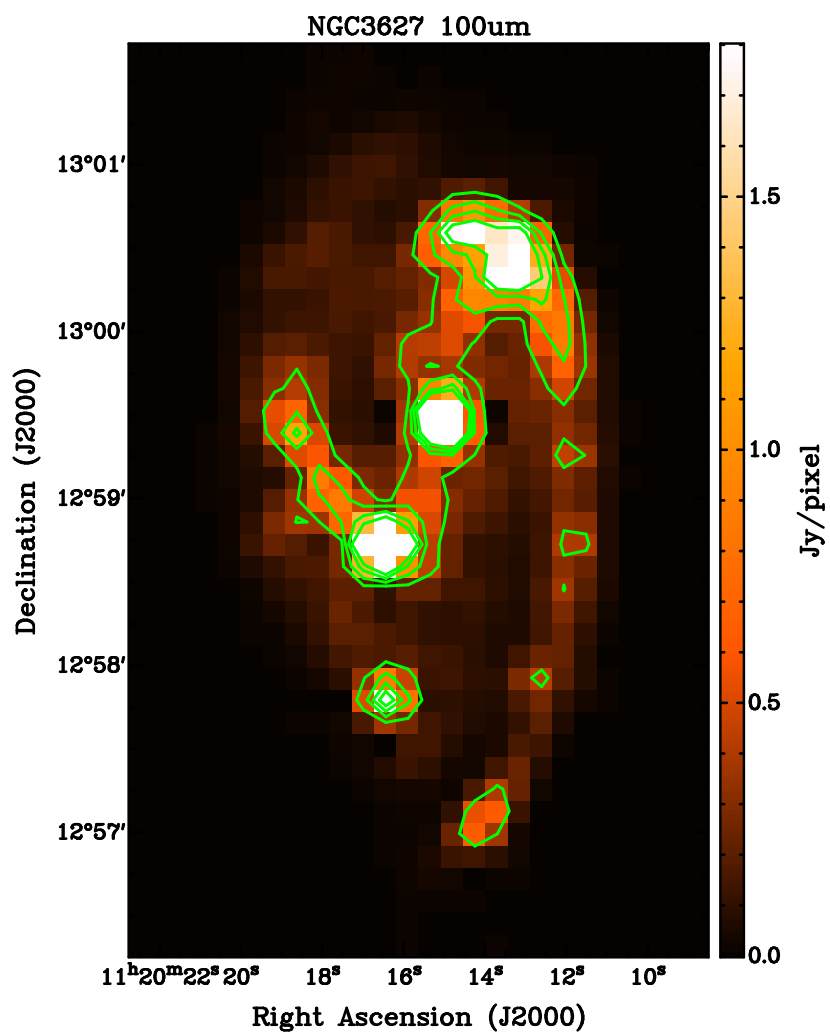


Figure 2.8: Image after the MAKEMAP filtering of 100 $\mu$ m observations with 20%, 40%, 60%, and 80% contours.

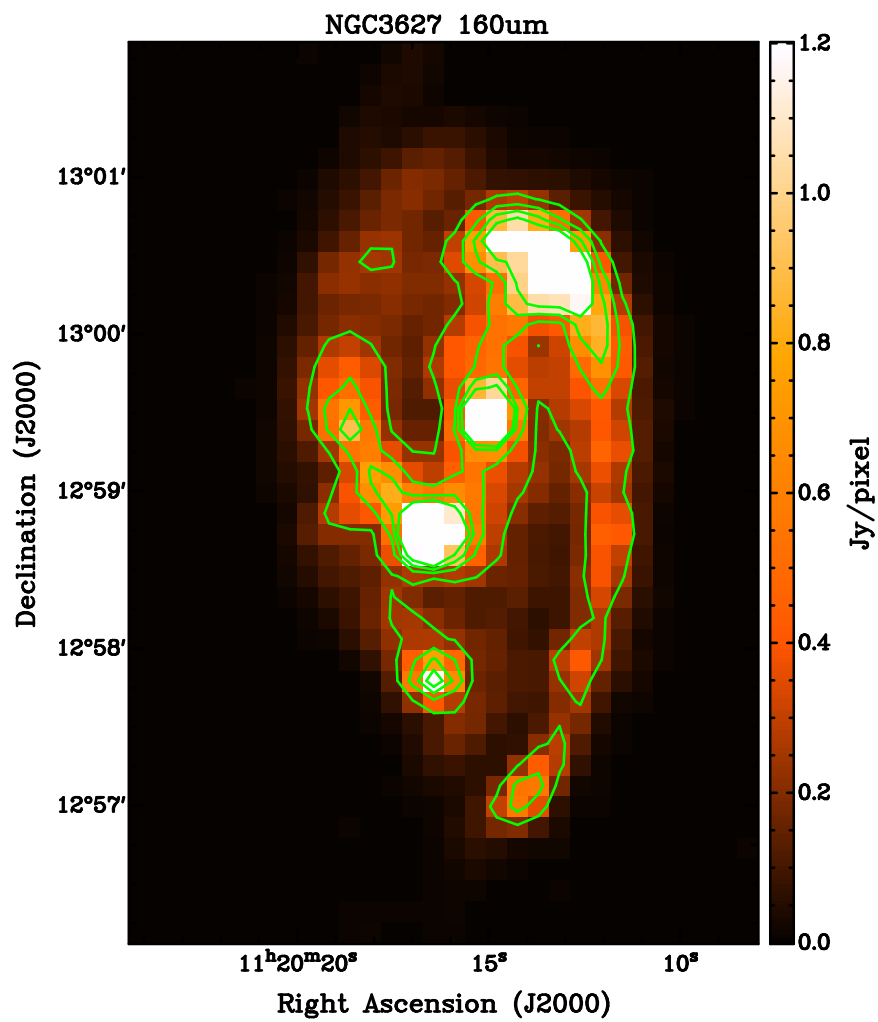


Figure 2.9: Image after the MAKEMAP filtering of 160 $\mu$ m observations with 20%, 40%, 60%, and 80% contours.

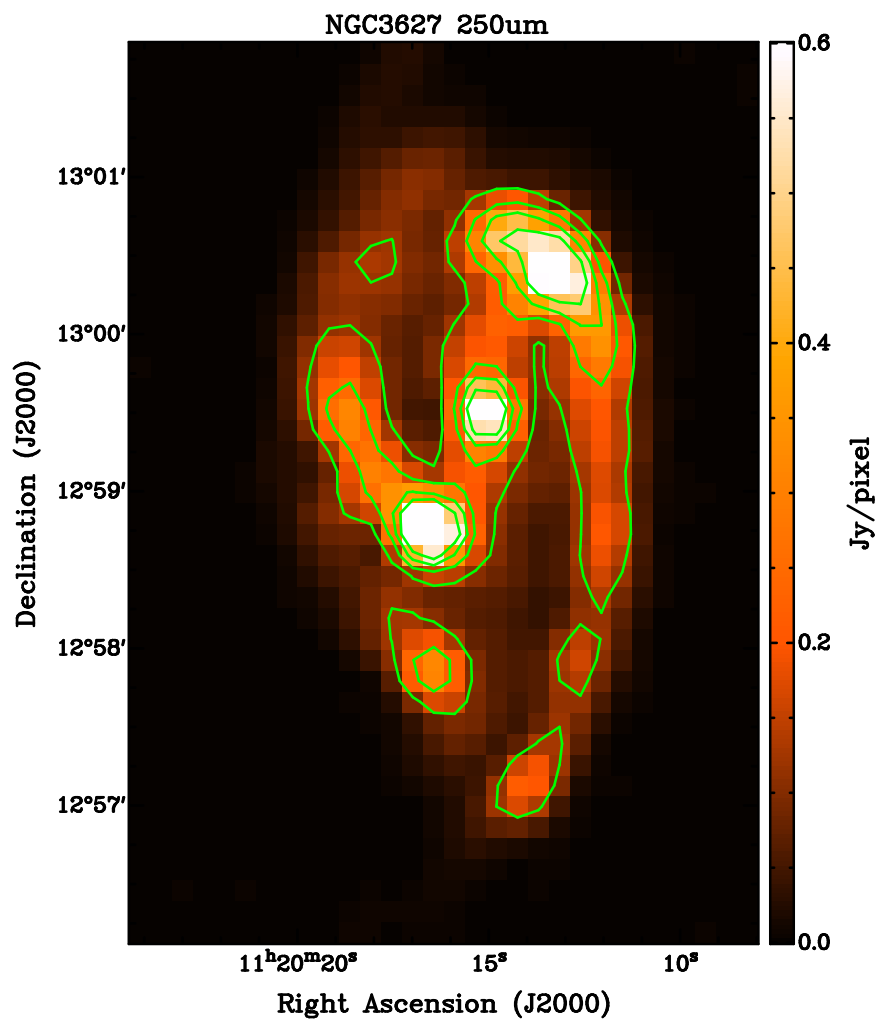


Figure 2.10: Image after the MAKEMAP filtering of  $250\mu\text{m}$  observations with 20%, 40%, 60%, and 80% contours.

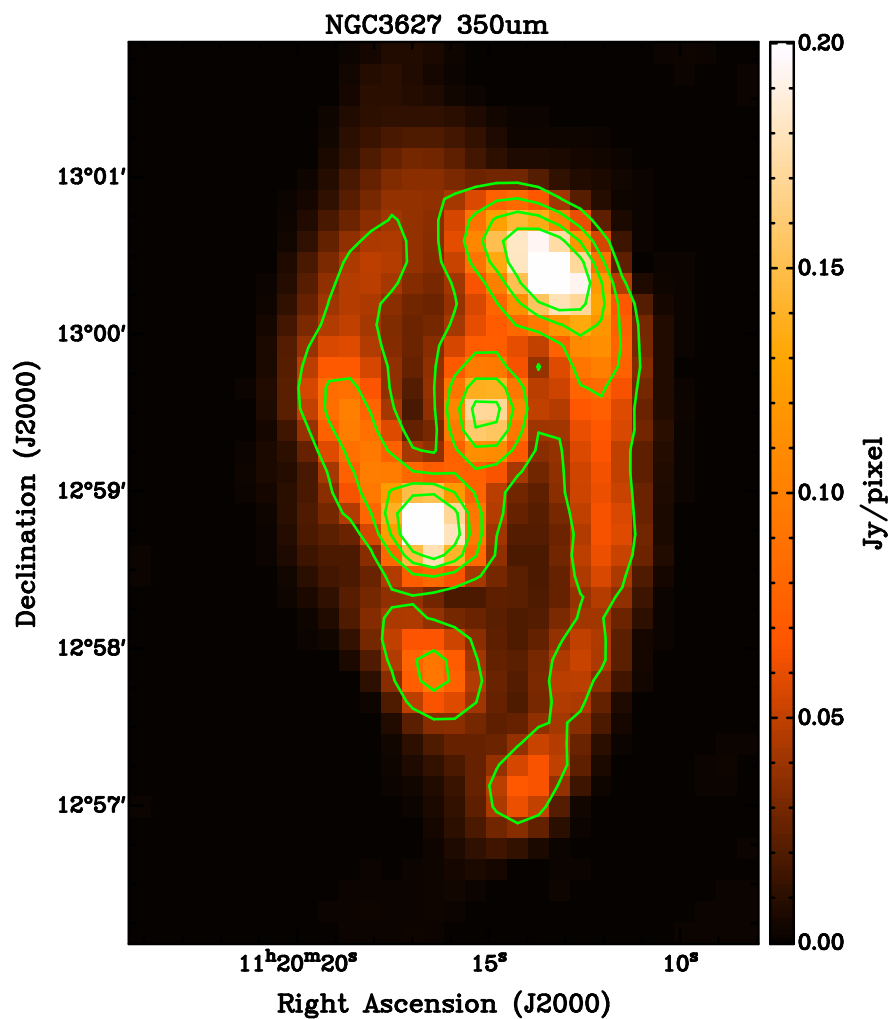


Figure 2.11: Image after the MAKEMAP filtering of the 350 $\mu$ m observations with 20%, 40%, 60%, and 80% contours.

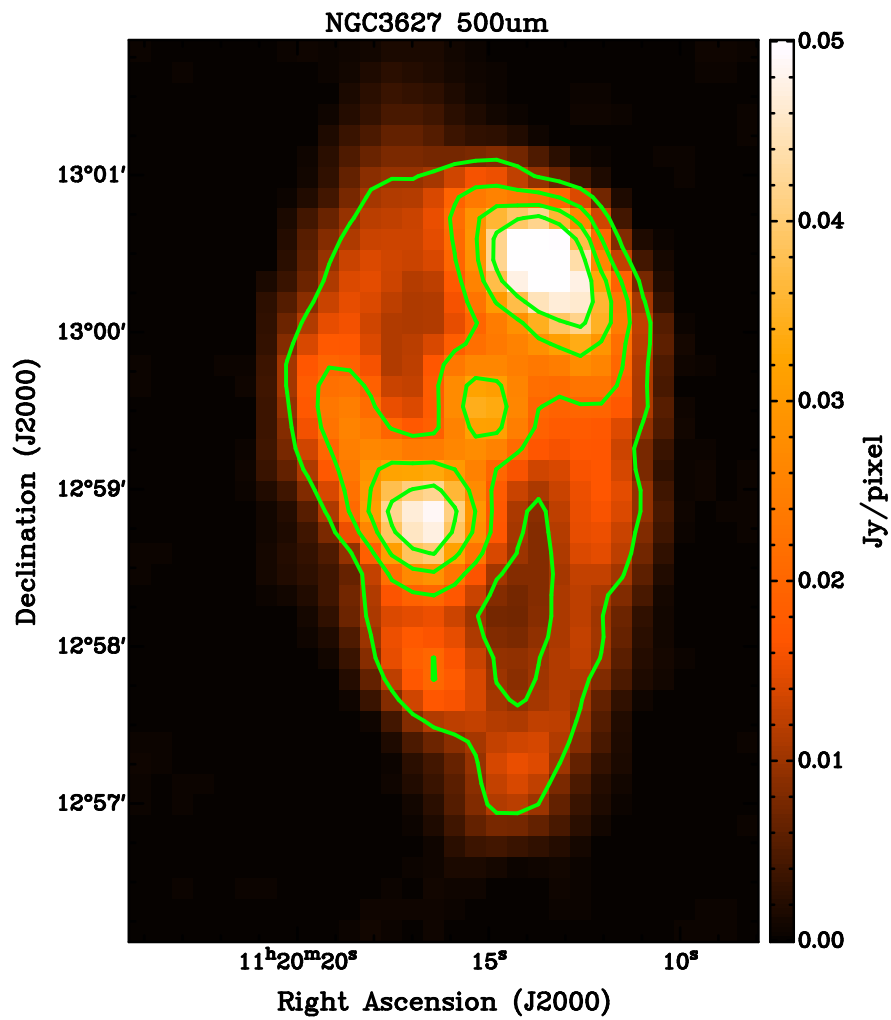


Figure 2.12: Image after the MAKEMAP filtering of the  $500\mu\text{m}$  observations with 20%, 40%, 60%, and 80% contours.



Table 2.2. Properties of NGC3627 KINGFISH Observations

Observation	Beam Properties $\theta_{beam}$	RMS $[mJy/Pixel]$	Percentage of Emission Removed
100 $\mu$ m	6.8''	2.24	11%
160 $\mu$ m	11.6''	3.95	17%
250 $\mu$ m	18.0''	2.47	20%
350 $\mu$ m	24.9''	1.08	21%
500 $\mu$ m	36.0''	0.387	28%

### 2.3.2 Nearby Galaxies Legacy Survey (NGLS)

The Nearby Galaxies Legacy Survey is an HI-selected set of 155 galaxies contained with distances between 2 and 25 Mpc observed using the instrumentation on the JCMT (Wilson et al., 2012). The NGLS consists of multiwavelength data that include the 450 $\mu$ m and 850 $\mu$ m data used for this thesis. As mentioned previously, the bandpass for SCUBA-2's 850 $\mu$ m emission contains the CO J=3-2 line which is contained in the NGLS data set. We used the zeroth moment CO J=3-2 maps from the NGLS to determine the percentage of CO J=3-2 emission present in the 850 $\mu$ m band as well as removing it for an accurate SED analysis. The rms and resolution of the CO J=3-2 emission are shown in Table 2.3 for 8'' by 8'' pixels, and the scan prior to convolution is shown in Figure 2.13.

### 2.3.3 Nobeyama 45-m

Determining a dust-to-gas ratio requires a molecular tracer to estimate the amount of molecular hydrogen present. The most frequently used tracer is CO

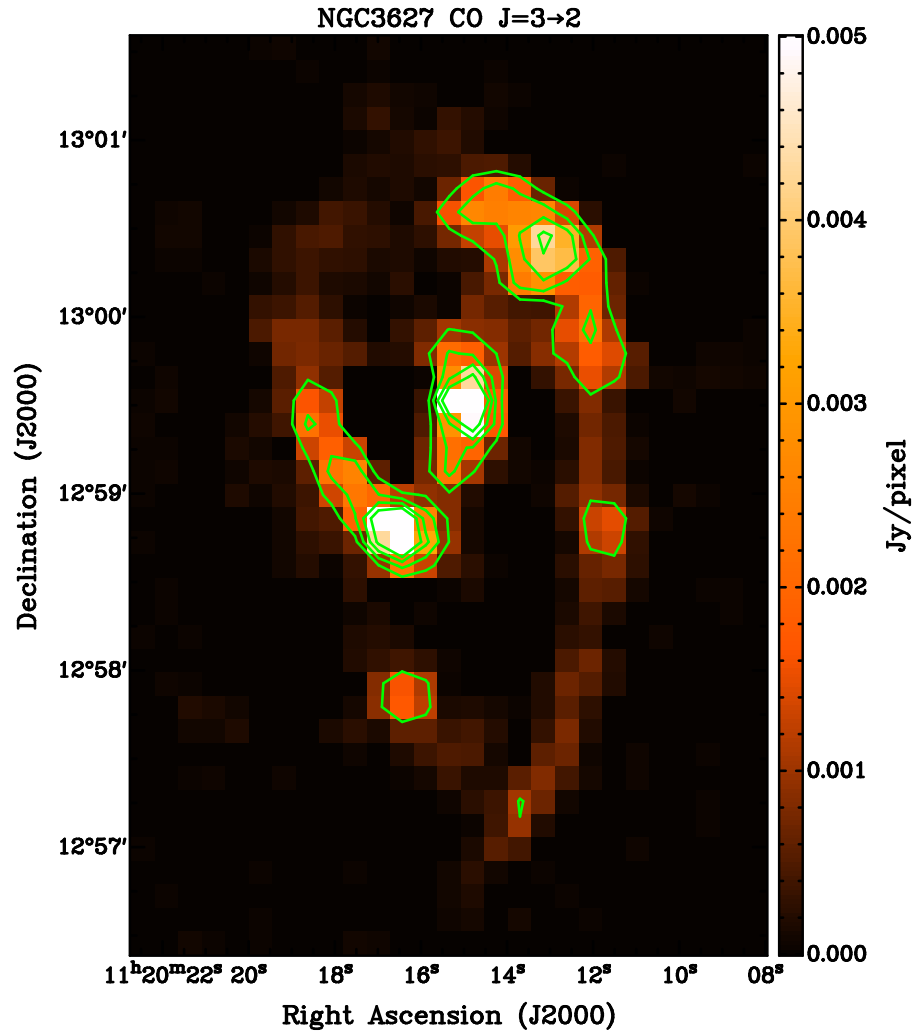


Figure 2.13: Residual of the MAKEMAP filtering of CO J=3-2 observations used to subtract line contamination from 850μm SCUBA-2 map with 20%, 40%, 60%, and 80% contours.

Table 2.3. Properties of NGC3627 Gas Observations

Observation	Beam Properties $\theta_{beam}$	RMS	Percentage of Emission Removed
CO J=1-0	15.0''	0.681 [K km s <sup>-1</sup> ]	20%
CO J=2-1	13.0''	0.305 [K km s <sup>-1</sup> ]	7%
CO J=3-2	14.5''	1.28e-2 [mJy pixel <sup>-1</sup> ]	29.8%
HI	10.6'' × 8.85''	0.760 [M <sub>⊙</sub> pc <sup>-2</sup> ]	>99%

J=1-0 due to its abundance in the ISM. The CO J=1-0 data were obtained from the Nobeyama 45-m CO Atlas of Nearby Spiral Galaxies (Kuno et al., 2007). The Nobeyama 45-m CO Atlas consists of galaxies with morphologies ranging from Sa to Scd, located less than 25Mpc from the Milky Way, inclination values less than 79°, 100 $\mu$ m flux greater than 10Jy, and spiral structure that has not been compromised through interactions. Any galaxies that met these criteria were then observed with the Nobeyama 45-m telescope (Kuno et al., 2007). The beam sizes and rms of the filtered CO J=1-0 map are displayed in Table 2.3 for 8'' by 8'' pixels, and the final image product can be seen in Figure 2.14.

#### 2.3.4 Hetrodyne Receiver Array CO-Line Extragalactic Survey (HER-ACLES)

The CO J=2-1 line was used to determine a CO 2 – 1/1 – 0 line ratio which can be used to trace a gradient in  $\alpha_{CO}$  and hint towards regions of high star formation (Reuter et al., 1996). We used the CO J=1-0 data from

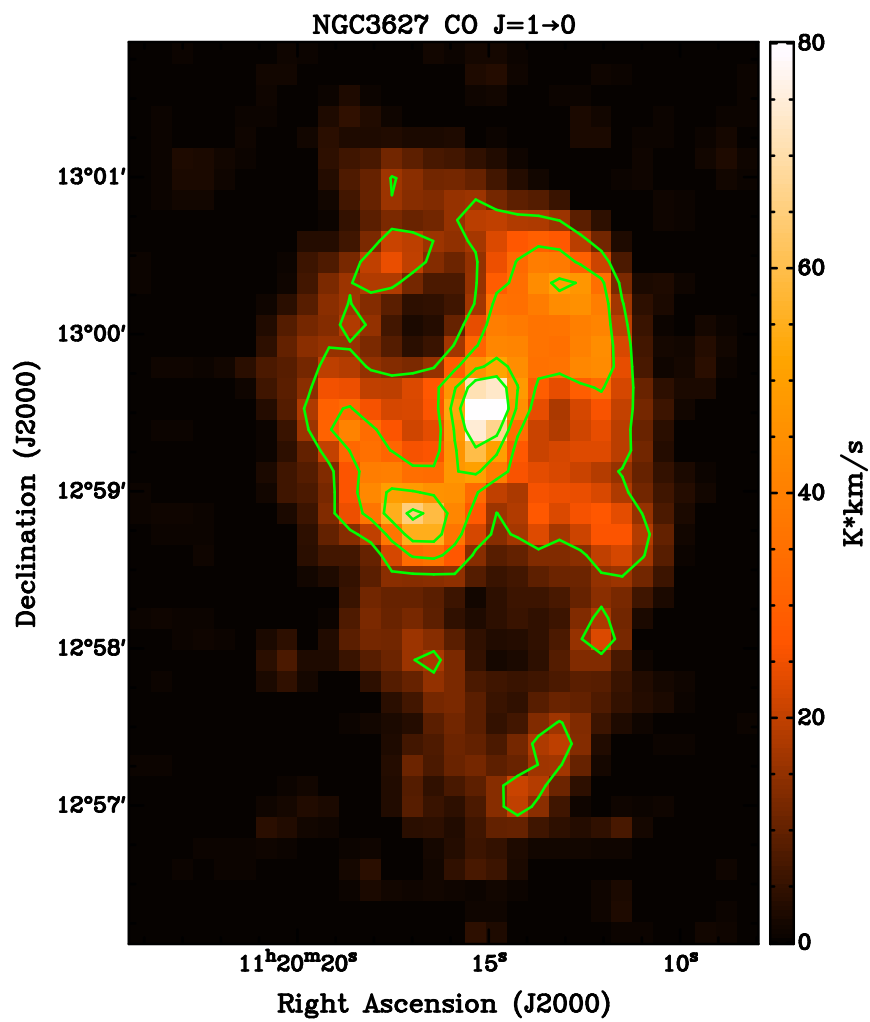


Figure 2.14: Residual of the MAKEMAP filtering of CO J=1-0 observations with 20%, 40%, 60%, and 80% contours.

the Nobeyama 45-m telescope (§ 2.3.3), and CO J=2-1 from the Heterodyne Receiver Array CO-Line Extragalactic Survey (HERACLES) using the IRAM 30-m telescope. The main goal of HERACLES was to quantify the relationship between atomic and molecular gas and star formation using a large sample of galaxies (Leroy et al., 2009). The galaxies chosen were targets contained in THINGS that were within the observing limits of the IRAM 30-m telescope. The final CO J=2-1 image can be seen in Figure 2.15 and the image properties can be seen in Table 2.3 with 8'' by 8'' pixels.

### 2.3.5 The HI Nearby Galaxy Survey (THINGS)

To determine the gas-to-dust ratio we had to determine the total amount of gas present which includes both atomic and molecular hydrogen. We approximated the amount of molecular hydrogen by using CO J=1-0, and measured the amount of atomic hydrogen (HI) present from The HI Nearby Galaxy Survey (THINGS) designed to observe HI emission in nearby galaxies with the extreme spatial resolution of the Very Large Array (VLA). Targets in THINGS included many of the SINGS targets with the exception of known HI poor sources (E/S0 type galaxies), dynamically complex systems (edge-on spirals), and large extended galaxies found in the Local Group (Walter et al., 2008). The resolution and rms of the filtered image are shown in Table 2.3 for 8'' by 8'' pixels. The final data product is shown in Figure 2.16 and has been converted to  $M_{\odot} \text{ pc}^{-2}$  using

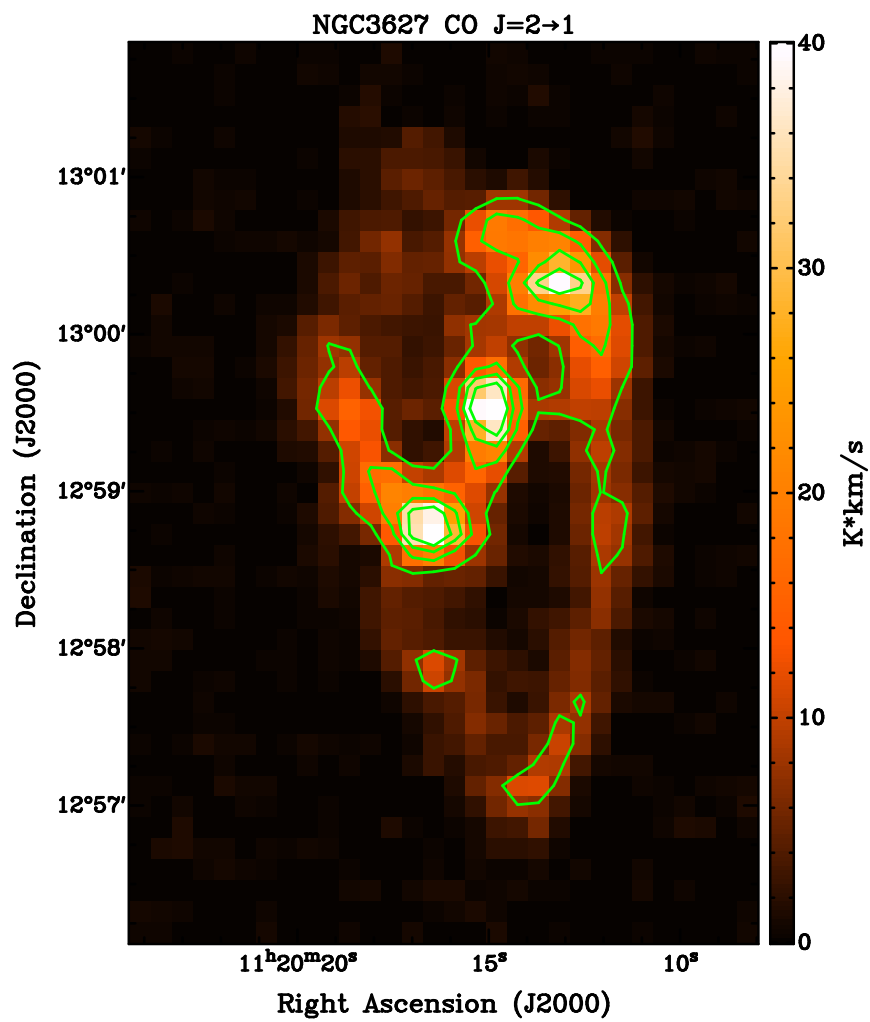


Figure 2.15: Residual of the MAKEMAP filtering of CO J=2-1 observations with 20%, 40%, 60%, and 80% contours.

$$M_{HI} [M_{\odot}] = 2.36 \times 10^5 D^2 \times \sum_i S_i \Delta v \quad (2.2)$$

(Walter et al., 2008) and then dividing by the pixel area in  $\text{pc}^2$  where  $D$  is the distance, and  $\sum_i S_i \Delta v$  is the first moment of the flux. Since most of the HI emission is diffuse and extended, the filtering process removed nearly all of the HI features. The removal of most of the HI resulted in a severe depression feature resampling a bowl in the middle of the map around the galaxy that was lower than the mean background value of the map. The bowling effect ended up further lowering the surface densities of the final maps by lowering the peak value and removing a significant fraction of the surface density.

## 2.4 Data Preparation for Analysis

Looking at Figures 2.5, 2.6 and comparing them with the ancillary data images in Figures 2.8-2.16 it is clear the data do not agree completely even with their extended structure removed. Other than the presence of the large scale/extended structure prior to filtering, the main difference between each image is its resolution, in particular the beam shape of the  $450\mu\text{m}$  data. We have taken several steps to correct for these disagreements and maximize the compatibility of the data. In order to account for the varying beam resolutions, we use a gaussian convolution to degrade the resolution of our maps to the largest beam size in our dataset,  $\sigma_{max}=36''$ . An appropriate convolution beam width is determined by

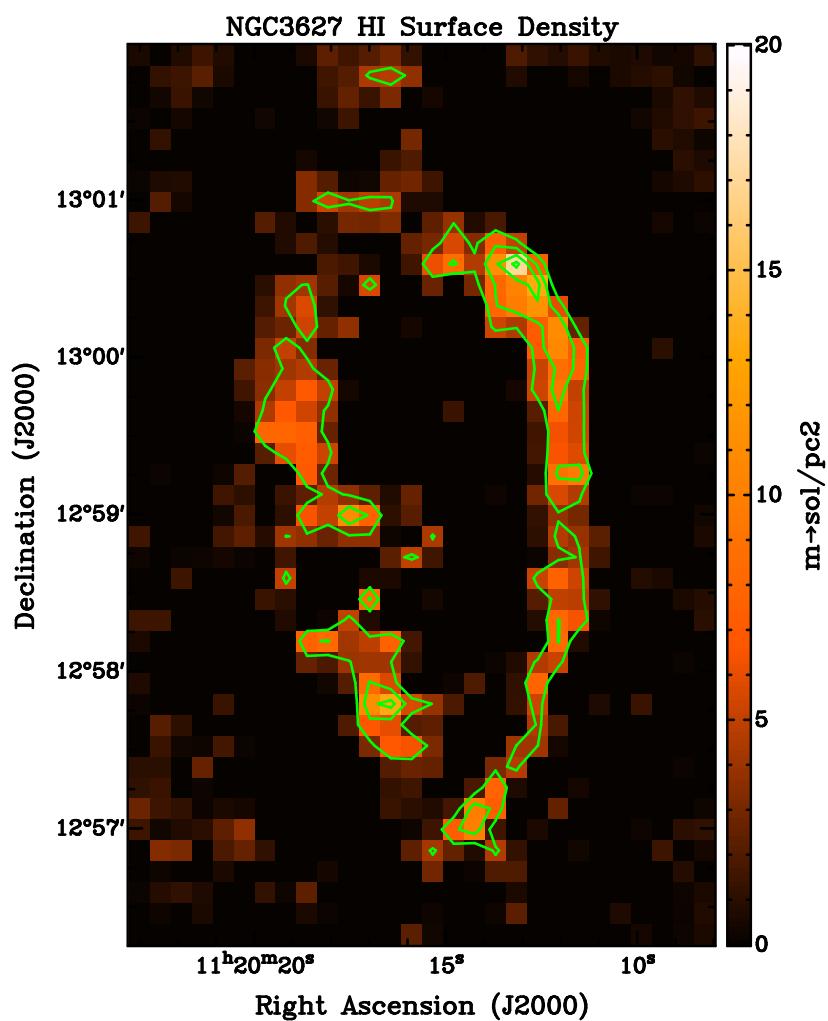


Figure 2.16: Residual of the MAKEMAP filtering of HI observations with 20%, 40%, 60%, and 80% contours.



$$\sigma_{desire} = \sqrt{\sigma_{max}^2 - \sigma_{given}^2} \quad (2.3)$$

where  $\sigma_{desire}$  is the desired beam width,  $\sigma_{max}$  is the beam size we are convolving to, and  $\sigma_{given}$  is the beam size we are convolving from. However, equation 2.3 only works when the beams are well approximated by a single gaussian which is not the case for the  $450\mu\text{m}$  beam. The steps taken to match the resolution of the  $450\mu\text{m}$  beam with the rest of the data set are given in §2.4.1.

Removing any large scale structure from our ancillary data is implemented using a feature built into MAKEMAP that allows us to add fake sources into the data during production. The fake source implementation allows us to remove the same amount of large scale structure from our ancillary data as was removed from the SCUBA-2 data. The steps taken to prepare the ancillary data are described in §2.4.2.

#### 2.4.1 Accounting for the $450\mu\text{m}$ Error Beam

Taking the  $450\mu\text{m}$  error beam into consideration is different from a normal beam convolution in the sense that we are not convolving the higher resolution map to the lowest resolution. Instead we are adding in an error beam similar to the error beam found in the  $450\mu\text{m}$  observations. We have to take these steps because convolving a double gaussian beam with a single gaussian kernel will not sufficiently remove the error component of our beam resulting in a poor approximation to the wings of our beam shape.

In order to accommodate the  $450\mu\text{m}$  map's error beam, we used a method employed by another SCUBA-2 legacy survey, the Gould Belt Survey. This method uses the distributive nature of the Fourier transform to create similar error components in the beams we were convolving to and from. Carrying out this convolution involves breaking the  $450\mu\text{m}$  beam into its two components,  $X_\alpha$  and  $X_\beta$ , to represent the main beam and error beam. The values of the main beam amplitude,  $X_\alpha$ , and error beam amplitude,  $X_\beta$ , will sum to one so the height of the total beam is normalized to one. The poorest resolution beam,  $X_{max}$ , is convolved with the two components  $X_\alpha$  and  $X_\beta$  and the resulting beams are added together. This process produces an equivalent two component beam to the  $450\mu\text{m}$  beam convolved with  $X_{max}$ . The relationship can be expressed as

$$\begin{aligned} X_{max} * X_\alpha + X_{max} * X_\beta &= (X_\alpha + X_\beta) * X_{max} \\ &= X_{450\mu\text{m}} * X_{max} \end{aligned} \tag{2.4}$$

where  $X_{max}$  is the poorest resolution beam,  $X_\alpha$  and  $X_\beta$  are the main and error beam of the  $450\mu\text{m}$  observations, and  $X_{450\mu\text{m}}$  is the double gaussian beam shape of the  $450\mu\text{m}$  observations.

#### 2.4.2 Extended Structure Removal via MAKEMAP

Due to the combination of methods used in MAKEMAP, large scale/extended structure is removed from the final SCUBA-2 images. However, in all of our ancillary data the large scale emission was present in the initial maps. The removal of the extended features from our ancillary data was carried out by

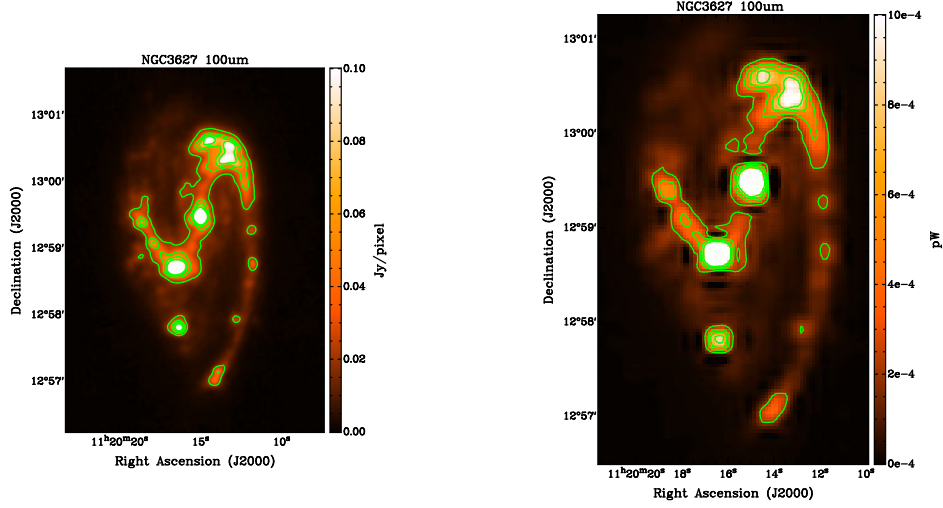
passing the data through MAKEMAP using a special function called fakemap. Using fakemap allows us to pass an image through the SCUBA-2 processing and have it added into the image being processed. We use the  $850\mu\text{m}$  map as our base image for the filtering process and add the ancillary data to the  $850\mu\text{m}$  image. The output image then consists of the sum of the ancillary data and the  $850\mu\text{m}$  map. Finally, the ancillary data were isolated by subtracting the  $850\mu\text{m}$  image from the fakemap output image.

Preparing the data to be added via fakemap consists of either converting the images from their native units into pW using the  $850\mu\text{m}$  flux calibration factor and scaling down to match the observed signal or by just applying a scaling factor. Which method is used is based on the desired units of the final map, and can be separated by what purpose the data had in our analysis.

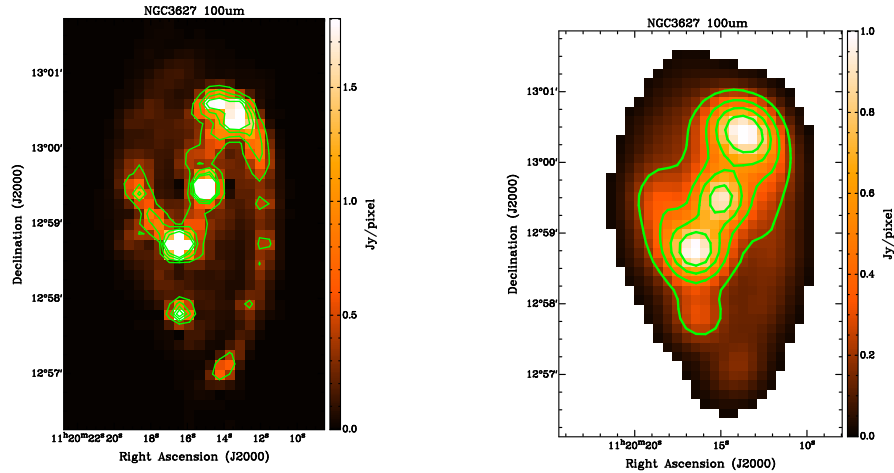
The data used in the SED fitting (KINGFISH and NGLS) were scaled to pW so they could have a similar reduction and calibration process as the SCUBA-2 maps. The KINGFISH data are regridded to a  $2''$  by  $2''$  pixel size and have the appropriate calibration factor from Dempsey et al. (2013) applied to convert from either MJy/sr to pW in the case of the  $250\mu\text{m}$ ,  $350\mu\text{m}$ , and  $500\mu\text{m}$  or from Jy/pixel to pW for the  $100\mu\text{m}$  and  $160\mu\text{m}$ . Converting the CO J=3-2 data requires the final product to be in the same units as the  $850\mu\text{m}$  observations in order to properly remove the molecular gas contribution. Converting from K km/s to mJy/beam involves applying a scaling constant of 0.70 [mJy/beam][K km/s] $^{-1}$  (Drabek et al., 2012) prior to applying the  $850\mu\text{m}$  flux calibration factor to convert to pW.

After the data has been converted to pW, the image used in fakemap is then scaled down to the same order of magnitude as the base image using a scaling factor specified prior to the map production. After the fakemap image has been processed and the  $850\mu\text{m}$  map subtracted, the maps are scaled back up using the same scaling factor used to scale them down and calibrated using the same flux calibration factors as the  $850\mu\text{m}$  map and scaled to an  $8''$  by  $8''$  grid. The amount of extended flux lost from the KINGFISH and NGLS images is shown in Tables 2.2 and 2.3. This process is illustrated in Figure 2.17 from the original Herschel  $100\mu\text{m}$  map, to the final image used in SED fitting convolved to the  $500\mu\text{m}$  beam resolution,  $36.0''$ .

The rest of the ancillary data are used in calculating a dust to gas ratio, and follow nearly the same process as the SED data filtering. The major difference is the CO J=1-0, CO J=2-1 and HI maps need to remain in their original units of K km/s and  $\text{M}_{\odot}/\text{pc}^2$ . This requirement simplified the process by only requiring a scaling factor of 0.001 to be applied to the original maps. After the image is scaled, it is filtered using the fakesource option in MAKEMAP with the  $850\mu\text{m}$  observation as the base image. The atomic and molecular gas maps were then isolated in the same fashion as the KINGFISH and NGLS by subtracting the  $850\mu\text{m}$  map. Then they were rescaled back to their original values, fit to an  $8''$  by  $8''$  grid and finally convolved to a  $36.0''$  resolution. The process is illustrated in Figure 2.18. The amount of emission lost is shown in tables 2.3.

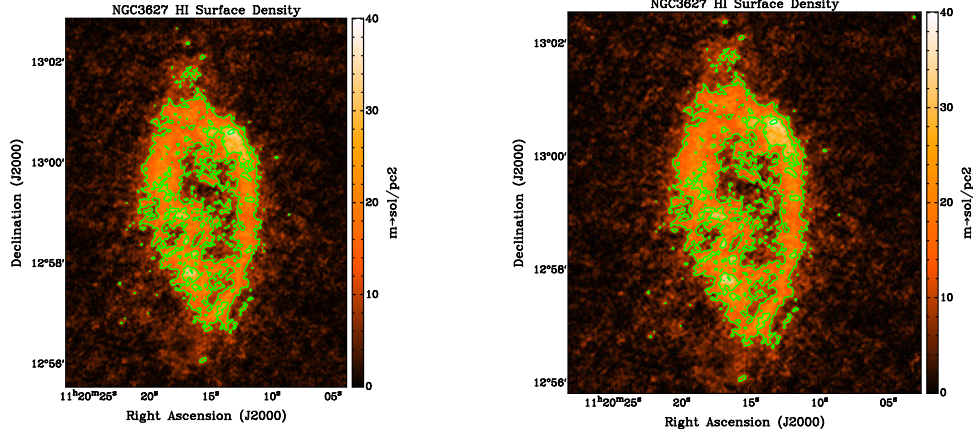


(a) Herschel 100μm image of NGC3627 with 1.7'' by 1.7'' pixels. (b) Herschel 100μm image converted to pW and rescaled to a 2'' by 2'' pixel grid.

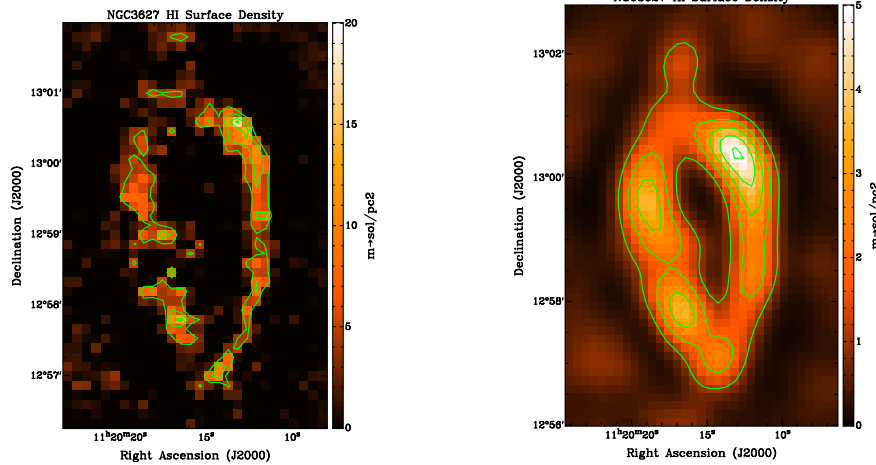


(c) 100μm map of NGC3627 after large scale structure has been removed and rescaled to an 8'' by 8'' grid. (d) 100μm map with extended structure removed and convolved to final resolution of 36.0'' with a 5σ cut applied.

Figure 2.17: The 100μm image from the beginning of processing to the end of processing. All of the contours shown are 20%, 40%, 60%, and 80%.



(a) HI surface density map of NGC3627 with  $1.5''$  by  $1.5''$  pixels. (b) HI surface density map rescaled to a  $2''$  by  $2''$  pixel grid.



(c) HI surface density map of NGC3627 after large scale structure has been removed and rescaled to an  $8''$  by  $8''$  grid. (d) HI surface density map with extended structure removed and convolved to final resolution of  $36.0''$ .

Figure 2.18: The HI surface density maps from the beginning of processing to the end of processing. The contours in the top row are 30%, 60% and 90%, and the contours in the bottom row are 20%, 40%, 60%, and 80%.

## Chapter 3

# Spectral Energy Distribution Analysis

### 3.1 SED Fitting Method

In order to determine a dust mass, we use the IDL package MPFIT (Markwardt, 2009) to fit equation

$$S_{\nu}(T) = \frac{M \kappa_{\nu,0}}{D^2} \left( \frac{\nu}{\nu_0} \right)^{\beta+3} B_{\nu}(T) \quad (3.1)$$

for the temperature,  $T$ , mass,  $M$ , and the emissivity index,  $\beta$  while the opacity,  $\kappa_{\nu,0}$ , distance,  $D$ , and reference wavelength,  $\nu_0$  are held fixed. The routine MPFIT utilizes the Levenberg-Marquardt algorithm. This algorithm uses a combination of two minimization techniques (the steepest descent method and the Newton-Raphson Method) to determine the parameter combination that corresponds to a minimum in the  $\chi^2$  space while maximizing the efficiency of the step sizes in each iteration (Burden & Faires, 2001). The algorithm begins by implementing the steepest descent method. The way this technique works is it will follow the direction opposite to the largest gradient in order to traverse the  $\chi^2$  space to locate a minimum. As the set of solutions approaches

Table 3.1. Systematic Calibration Uncertainties for SCUBA-2 and KINGFISH Observations

Observation	Scaling Factor
100 $\mu\text{m}$	3%
160 $\mu\text{m}$	5%
250 $\mu\text{m}$	7%
350 $\mu\text{m}$	7%
450 $\mu\text{m}$	12%
500 $\mu\text{m}$	7%
850 $\mu\text{m}$	8%

a minimum, it will switch to the Newton-Raphson method to locate the best set of parameters by finding where the derivative at that point is closest to zero (Gavin, 2013).

In order for MPFIT to provide the most accurate fit, we establish a reasonable uncertainty for each of our data points, and determine a realistic set of starting points for the fitting. The variance for our SCUBA-2 data is determined using

$$\sigma^2 = \sigma_{obs}^2 + \sigma_{rms,sky}^2 + \sigma_{calib}^2 \quad (3.2)$$

such that  $\sigma_{obs}$  is the noise determined by MAKEMAP,  $\sigma_{rms,sky}$  is the RMS of the sky, and  $\sigma_{calib}$  is the product of calibration uncertainty and observed flux for each observed wavelength. The systemic calibration scaling factors are shown in Table 3.1.



The variances for the KINGFISH data are determined in a similar fashion using

$$\sigma^2 = \sigma_{rms,sky}^2 + \sigma_{calib}^2. \quad (3.3)$$

The observation error is excluded since the reported variance in the filtered images reflects the fake source image used and not the KINGFISH data set.

The nature of the Levinberg-Marquardt method leaves the solution vulnerable to converge at a local minimum rather than converging at the global minimum. This is remedied by selecting reasonable initial conditions. The initial conditions we used were a modified blackbody with a temperature of 20 K, a dust emissivity index of 2, and a mass determined by

$$\begin{aligned} M &= \frac{D^2 S_{250}}{\kappa_{\nu,0} B_{250}(T)} \left( \frac{\nu}{\nu_0} \right)^{-\beta} \\ &= 5.40 \times 10^5 S_{250} [M_{\odot}] \end{aligned} \quad (3.4)$$

using the flux from the  $250\mu\text{m}$  emission and our initial temperature and dust emissivity index values with a reference opacity of  $0.2665 \text{ m}^2 \text{ kg}^{-1}$  at  $300\mu\text{m}$ . When the best fit values have been calculated we use equation 3.4 to determine the dust mass associated with the  $250\mu\text{m}$  emission instead of using the fitted peak mass in order to increase the signal to noise of our data and avoid any temperature dependences associated with emission further from the Rayleigh-Jeans tail of the SED. The error in the dust mass is then determined by taking the total derivative of the mass function with respect to each of the free variables.

## 3.2 Fitting the Spectral Energy Distribution

The fitting procedure was carried out in two different ways on a modified blackbody equation. One of the two methods is fitting an SED to each individual pixel in order to generate a set of parameter maps. The second method sums the flux of each of the selected regions shown in Figure 3.1 to maximize the signal to noise ratio in order to generate a more precise set of parameters. For both of the fitting methods the mass,  $M$ , and temperature,  $T$ , are set as free parameters, but the emissivity index,  $\beta$ , requires special treatment for each of the methods. The distance,  $D$ , has been set to 9.4 Mpc (Walter et al., 2008), and the reference opacity,  $\kappa_{\nu,0}$ , was tested using  $0.2665 \text{ m}^2 \text{ kg}^{-1}$  (Li & Draine, 2001) and  $1.0 \text{ m}^2 \text{ kg}^{-1}$  (Planck Collaboration et al., 2011).

### 3.2.1 Pixel SED Fits

In order to generate a parameter map of NGC3627, each individual pixel has its own SED determined from the available wavelengths described in the observations chapter. The fits are performed over  $100\mu\text{m}$ ,  $160\mu\text{m}$ ,  $250\mu\text{m}$ ,  $350\mu\text{m}$ ,  $450\mu\text{m}$  or  $500\mu\text{m}$ , and  $850\mu\text{m}$  observations. Initially, we excluded the  $500\mu\text{m}$  emission in order to increase the resolution of our final maps, but an over abundance of emission in the  $450\mu\text{m}$  map provided unreliable results, so we exchanged the  $450\mu\text{m}$  emission with  $500\mu\text{m}$  emission. The maps used in the SED fitting is shown in Figure 3.2 where each image has been convolved to the resolution of the  $500\mu\text{m}$  observations and a  $5\sigma$  cut has been applied. The treatment of the dust emissivity index is performed by fixing it at  $\beta = 1.8$  for the Planck opacity model where the opacity is  $\kappa_{300\mu\text{m},0} = 1.0 \text{ m}^2 \text{ kg}^{-1}$

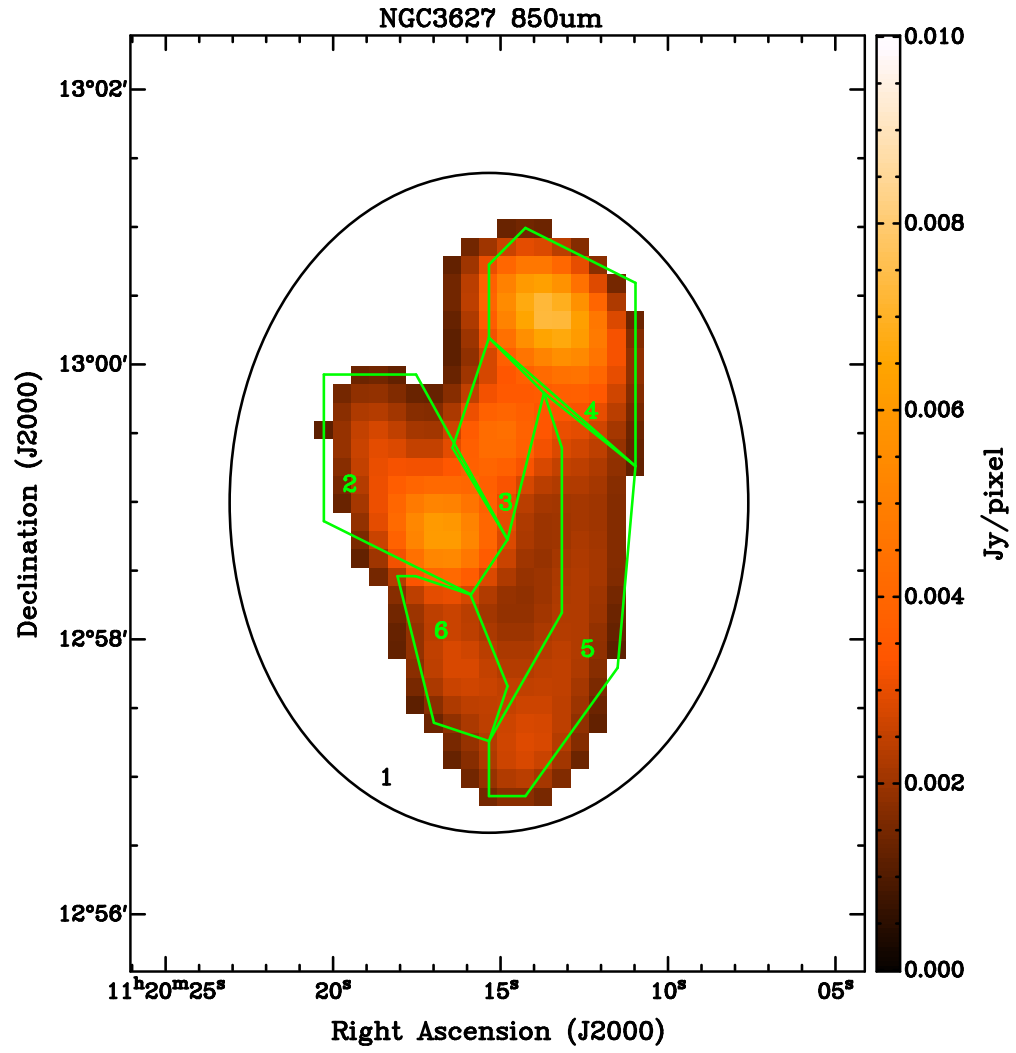


Figure 3.1: 850 $\mu$ m emission convolved to the 500 $\mu$ m beam size overlaid with the selected regions of NGC3627 labeled 1 through 6 such that region 1 includes the entire galaxy.

(Planck Collaboration et al., 2011) and  $\beta = 2.0$  for the Li and Draine opacity model where the opacity is  $\kappa_{300\mu m,0} = 0.2665 \text{ m}^2 \text{ kg}^{-1}$  (Li & Draine, 2001). A third fit is performed where the emissivity index is allowed to vary as a free parameter. While the emissivity index is allowed to vary, the opacity being used is the Planck model. Using either an opacity of  $1.0 \text{ m}^2 \text{ kg}^{-1}$  or  $0.2665 \text{ m}^2 \text{ kg}^{-1}$  will not affect the shape of the SED, only its normalization. In the case of our fits, it is the mass that acts as the normalizing value, so increasing or decreasing the opacity will yield the opposite effect in the mass. The inverse proportionality can be seen in equation 3.4.

The quality of the fit using the  $450\mu\text{m}$  observations for the Li and Draine model of  $\beta=2$  and  $\kappa_{\nu,300}=0.2665$  is shown in Figure 3.3. The quality of the fit is determined by how well the expected flux from the SED fitting matches the observed flux. If the fits are able to recreate the observed emission, then all of the points will lie on the line  $y = x$  shown in the plots as a black line. If the SED is underestimating the flux, the points will appear below the 1 to 1 line, and an over estimation from the SED will result in points above the line.

From Figure 3.3, the fitting procedure is able to handle the  $100\mu\text{m}$ ,  $250\mu\text{m}$ , and  $850\mu\text{m}$  with some slight under estimation in the  $160\mu\text{m}$  and over estimation in the  $350\mu\text{m}$ . The most compelling piece of information in Figure 3.3 is the SED's inability to fit the observed  $450\mu\text{m}$  flux despite the care taken to account for the odd beam shape of the  $450\mu\text{m}$  data. The discrepancy between the observed and fitted fluxes is not a result of a poor fit, but rather an intrinsic error in the  $450\mu\text{m}$  observations. The over abundance of flux present in the SCUBA-2  $450\mu\text{m}$  data was determined to be an issue with the data itself

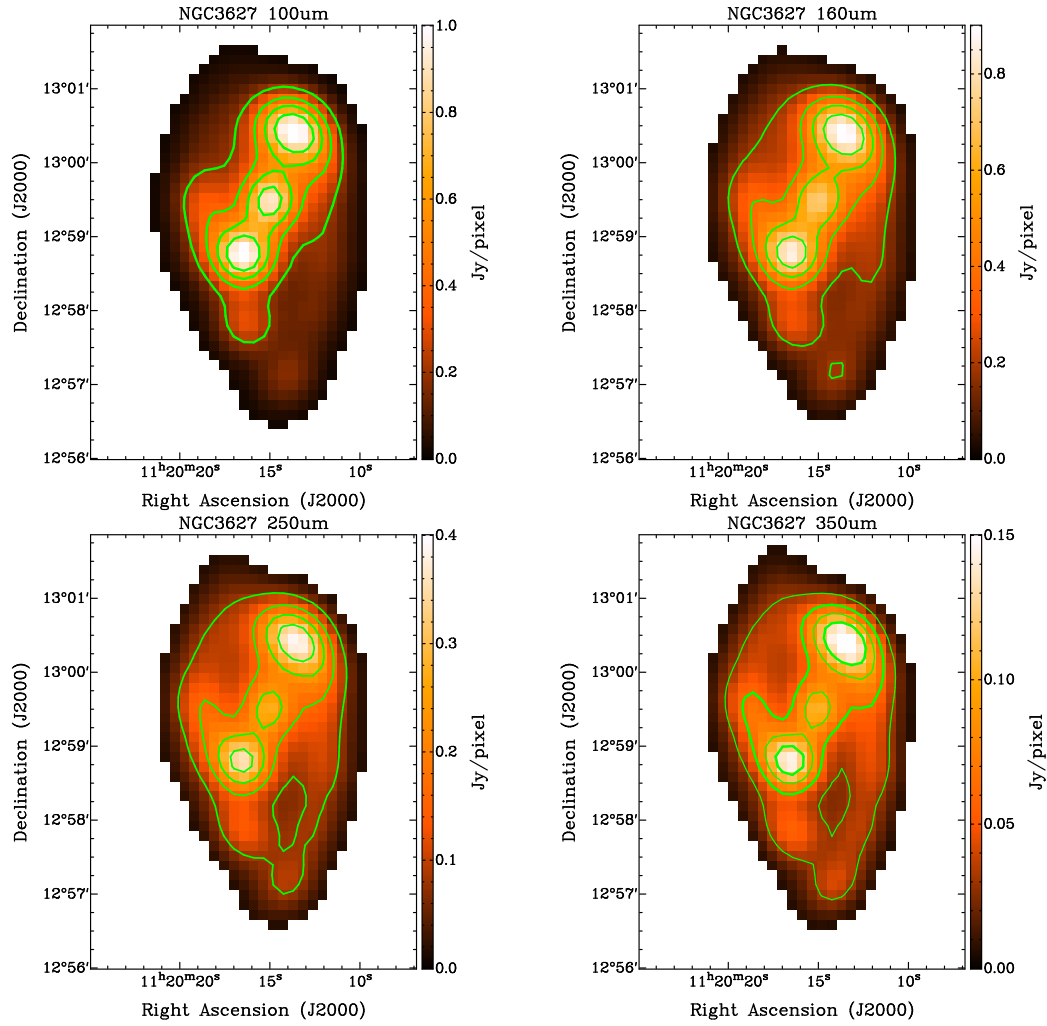


Figure 3.2: Observation of NGC3627 used for SED fitting. Each of the images is on a  $8''$  by  $8''$  grid and has been convolved to  $36.0''$  with a  $5\sigma$  cut applied. The contours for each image are 20%, 40%, 60%, and 80%.

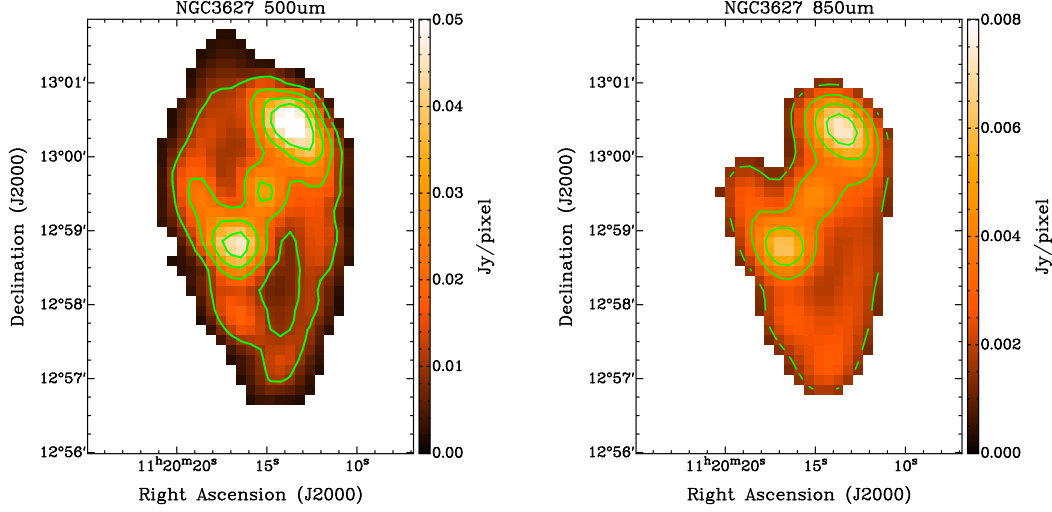


Figure 3.2: (continued)

rather than a signature of a physical process. We determined that the  $450\mu\text{m}$  data was overestimating the flux by calculating a  $450\mu\text{m}$  flux using a linear fit between the filtered  $350\mu\text{m}$  flux of 27.1 Jy and the filtered  $500\mu\text{m}$  flux of 8.56 Jy. The  $450\mu\text{m}$  flux expected from these two data points was 14.7 Jy; however our  $450\mu\text{m}$  flux was measured to be 20.6 Jy.

In order to avoid any errors in our final parameter maps, we substitute the  $450\mu\text{m}$  emission with KINGFISH  $500\mu\text{m}$  emission. The quality of the fitted SEDs using the  $500\mu\text{m}$  emission are shown in Figures 3.4, 3.5, and 3.6 for the Planck model, Li and Draine model and the emissivity as a free parameter, respectively. To assign a numerical quantity to the quality of the fit the vertical distance was calculated for each point to the 1 to 1 line and then summed. The summed distances are shown in Table 3.2 and suggest the best fit comes from allowing the emissivity index to vary. The resulting parameter maps of the fits using the  $500\mu\text{m}$  observations are shown in Figure 3.7. The numerical

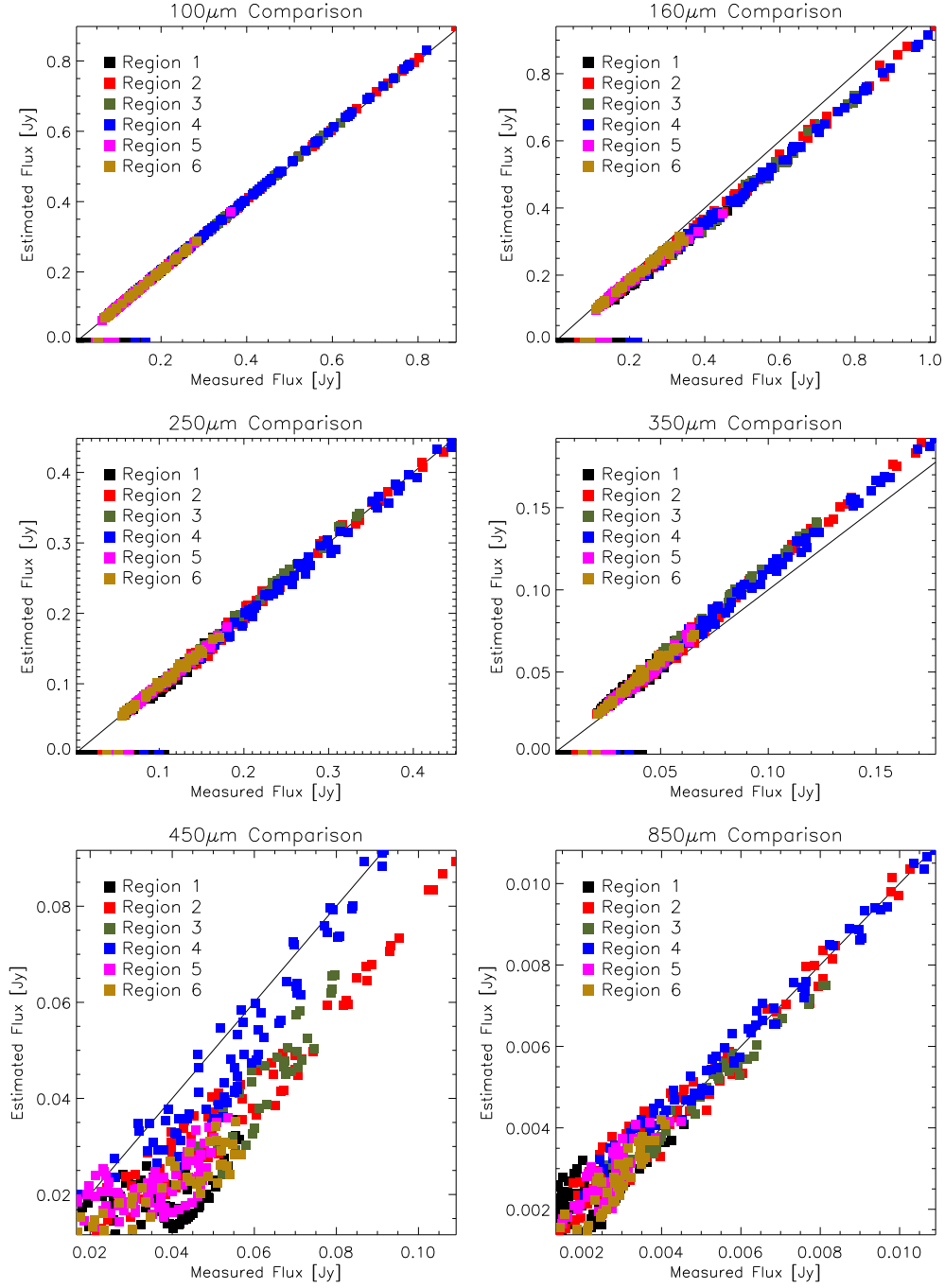


Figure 3.3: Quality of the SED fits to the Li and Draine model using the 450 $\mu$ m emission. The regions shown are the regions in Figure 3.1.

Table 3.2. Total Distance to 1 to 1 Line Using the  $500\mu\text{m}$  Emission

Observation	Planck Model	Li and Draine Model	Variable Emissivity Index
$100\mu\text{m}$	0.000	0.01245	0.1277
$160\mu\text{m}$	15.55	8.979	2.159
$250\mu\text{m}$	5.808	3.071	0.4465
$350\mu\text{m}$	0.8045	0.3541	0.1161
$500\mu\text{m}$	0.08192	0.1147	0.1866
$850\mu\text{m}$	0.02825	0.05218	0.09528
Total	22.23	12.583	3.131

Table 3.3. Best Fit Parameters for Planck Model Using  $500\mu\text{m}$  Emission for Pixel Fits

Region	Average $\beta$	Total Dust Mass [ $10^5 M_\odot$ ]	Average Dust Surface Density [ $M_\odot pc^{-2}$ ]	Average Temperature [K]
1	1.8	$52 \pm 23$	$0.10 \pm 0.05$	$26 \pm 2$
2	1.8	$13 \pm 4$	$0.12 \pm 0.04$	$27 \pm 1$
3	1.8	$6 \pm 1$	$0.12 \pm 0.02$	$28.8 \pm 0.6$
4	1.8	$16 \pm 6$	$0.15 \pm 0.05$	$26 \pm 1$
5	1.8	$10 \pm 2$	$0.08 \pm 0.02$	$24 \pm 1$
6	1.8	$4 \pm 1$	$0.08 \pm 0.02$	$25 \pm 1$

values from fitting each model are shown in Tables 3.3, 3.4, and 3.5 where each region corresponds to the regions labeled in Figure 3.1.

### 3.2.2 Total Region Flux SED Fits

The second method used to determine the dust mass was to fit the SED to the flux of each region in Figure 3.1. Performing the fit in this manner is



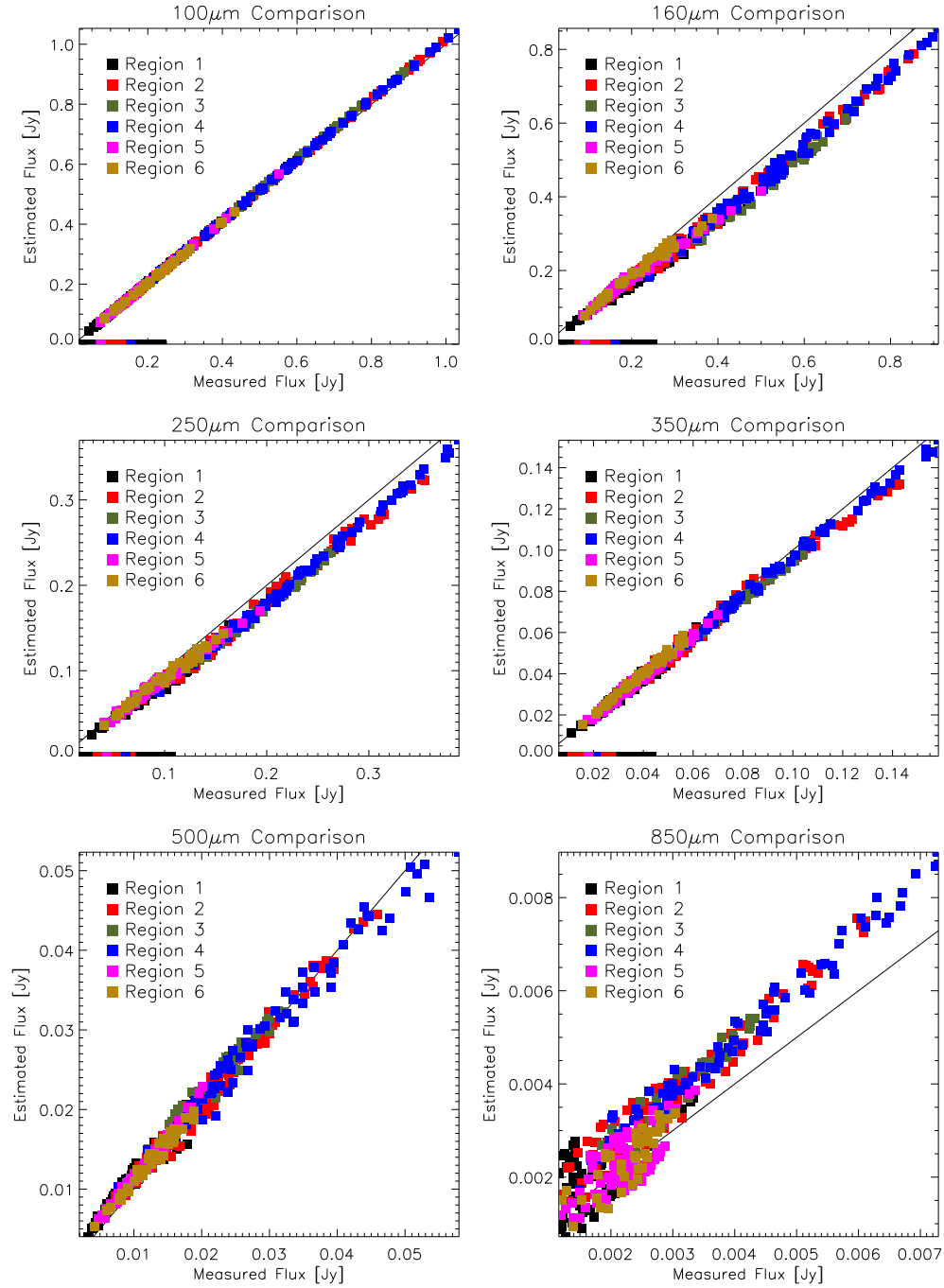


Figure 3.4: Quality of the SED fits using the Planck model with the 500 $\mu$ m emission. The regions shown are the regions in Figure 3.1.

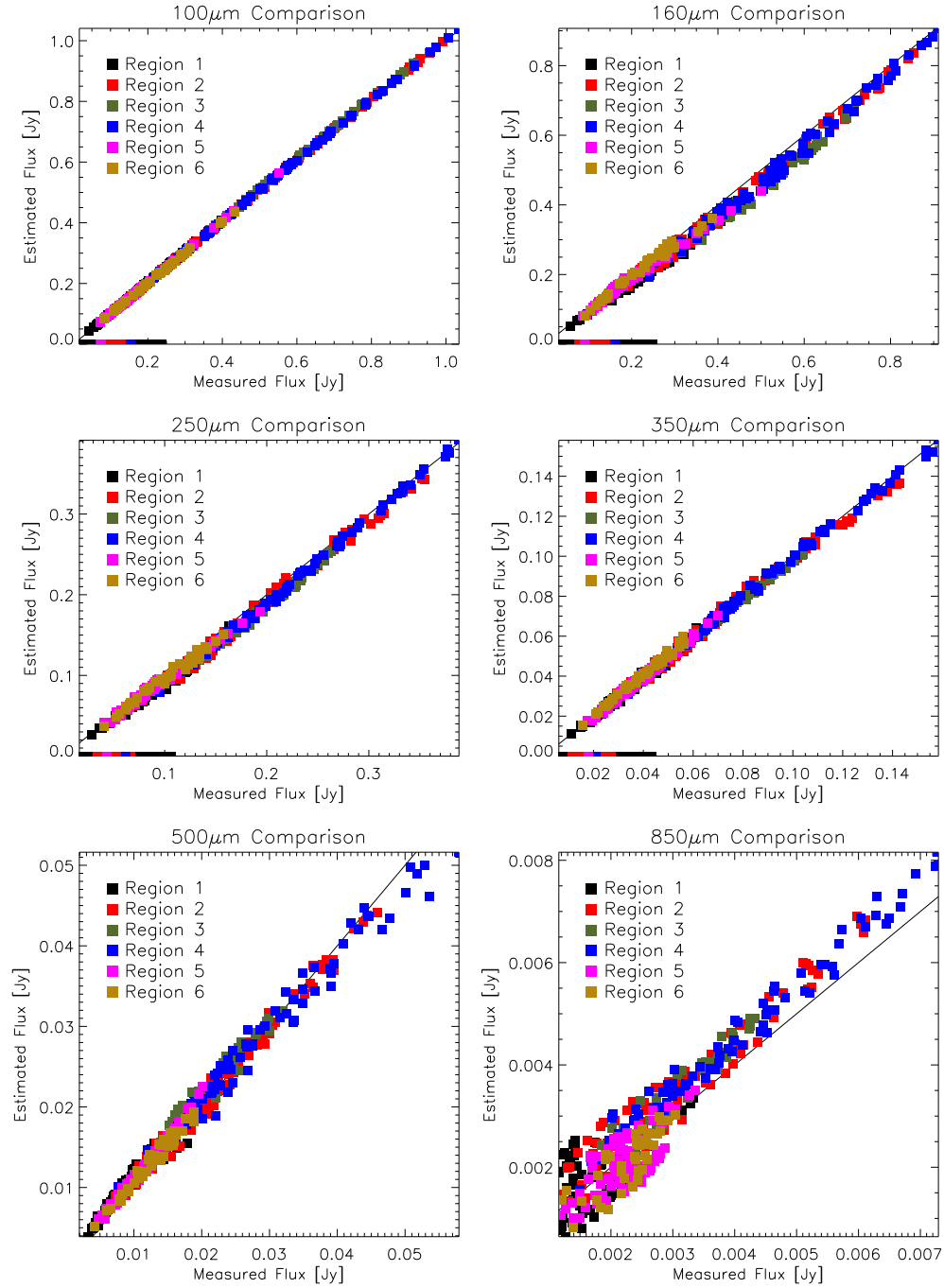


Figure 3.5: Quality of the SED fits using the Li and Draine model with the 500 $\mu$ m emission. The regions shown are the regions in Figure 3.1.

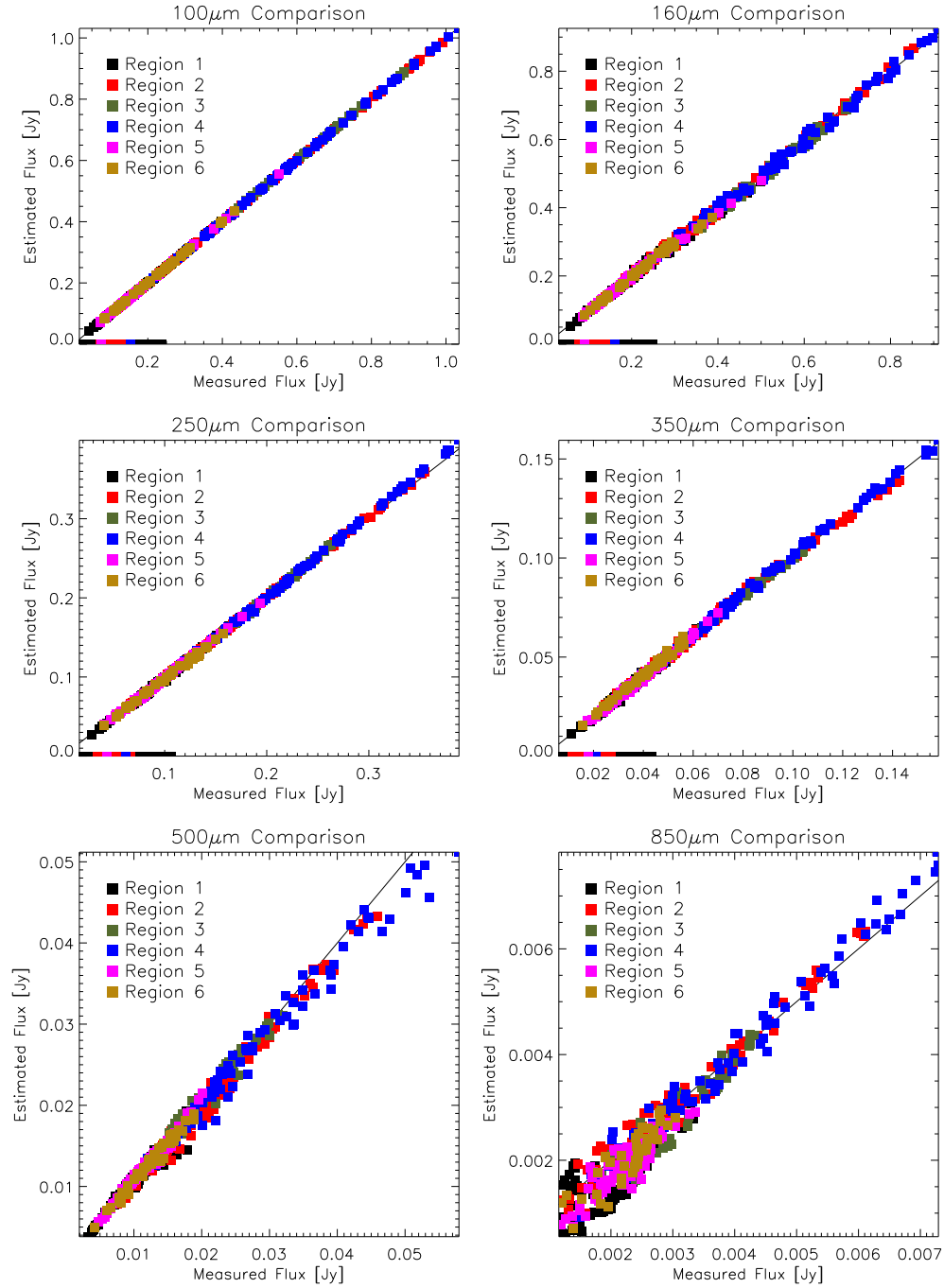


Figure 3.6: Quality of the SED fits with the emissivity index as a free parameter with the 500μm emission. The regions shown are the regions in Figure 3.1.

Table 3.4. Best Fit Parameters for Li and Draine Model Using  $500\mu\text{m}$  Emission for Pixel Fits

Region	Average $\beta$	Total Dust Mass [ $10^5 M_\odot$ ]	Average Dust Surface Density [ $M_\odot pc^{-2}$ ]	Average Temperature [K]
1	2.0	$230 \pm 103$	$0.5 \pm 0.2$	$24 \pm 2$
2	2.0	$57 \pm 19$	$0.6 \pm 0.2$	$25 \pm 1$
3	2.0	$28 \pm 5$	$0.52 \pm 0.09$	$26.4 \pm 0.5$
4	2.0	$70 \pm 22$	$0.7 \pm 0.3$	$24.4 \pm 0.8$
5	2.0	$42 \pm 9$	$0.34 \pm 0.08$	$22.4 \pm 0.8$
6	2.0	$18 \pm 4$	$0.33 \pm 0.08$	$23.5 \pm 0.9$

Table 3.5. Best Fit Parameters for  $\beta$  As A Free Parameter Using  $500\mu\text{m}$  Emission for Pixel Fits

Region	Average $\beta$	Total Dust Mass [ $10^5 M_\odot$ ]	Average Dust Surface Density [ $10^5 M_\odot pc^{-2}$ ]	Average Temperature [K]
1	$2.2 \pm 0.2$	$73 \pm 31$	$0.14 \pm 0.06$	$22 \pm 1$
2	$2.3 \pm 0.2$	$18 \pm 5$	$0.18 \pm 0.05$	$22 \pm 2$
3	$2.34 \pm 0.09$	$9 \pm 1$	$0.18 \pm 0.02$	$23.0 \pm 0.9$
4	$2.2 \pm 0.1$	$22 \pm 5$	$0.21 \pm 0.05$	$22 \pm 1$
5	$2.1 \pm 0.2$	$12 \pm 4$	$0.10 \pm 0.03$	$22 \pm 1$
6	$2.1 \pm 0.1$	$5 \pm 1$	$0.09 \pm 0.03$	$23.0 \pm 0.9$

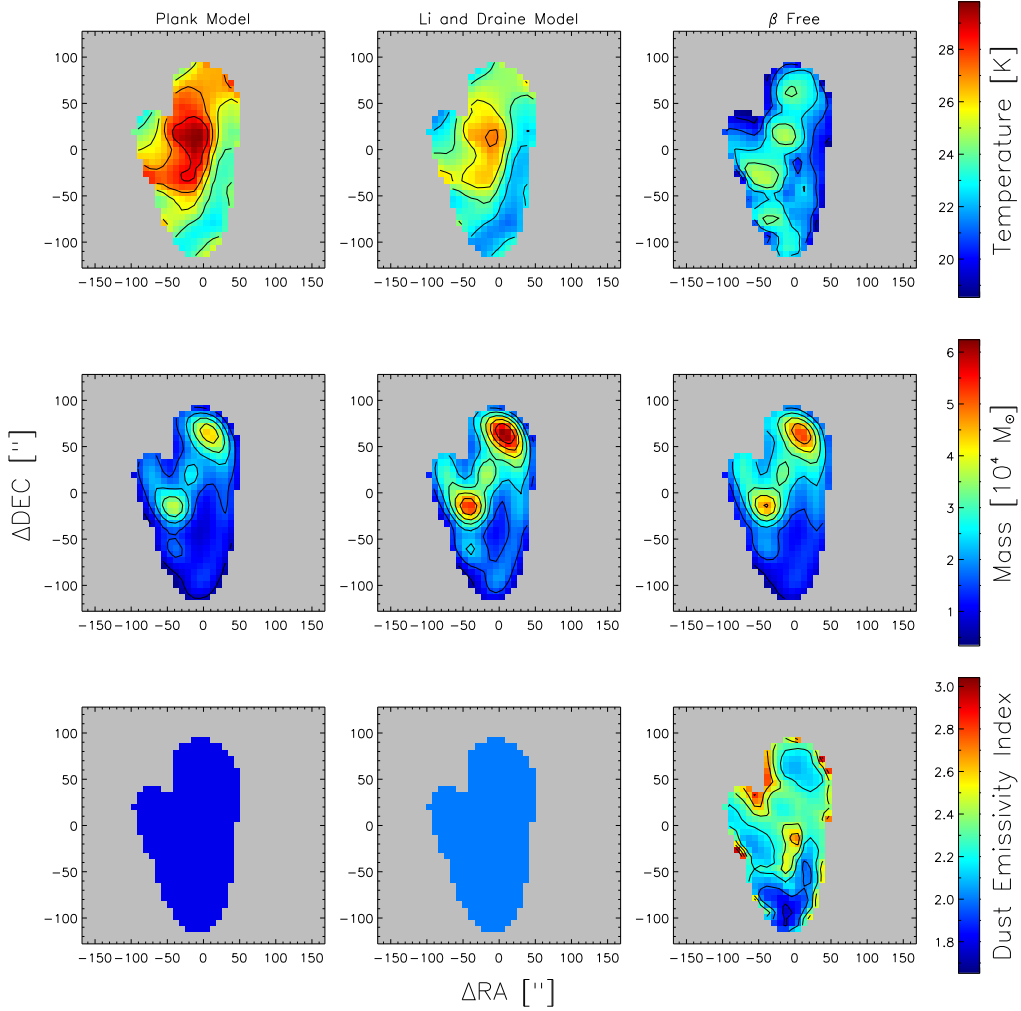


Figure 3.7: Returned value for the SED fits using the 500 $\mu$ m observations with the Planck model in the left column, the Li and Draine model in the middle column, and  $\beta$  as a free variable in the right column. The top row shows the temperature with contours from 19.5K to 28.5K in 1.5K increments. The second row show the returned masses with contours from 1.9 $M_{\odot}$  to 13.3 $M_{\odot}$  in 1.9 $M_{\odot}$  increments. The Li and Draine mass fits have been divided by three to better show the features relative to the other two fits. The bottom row shows the returned dust emissivity index values with contours from 1.8 to 2.8 with 0.2 increments.

beneficial because it increases the signal to noise of the region and produces a more precise set of parameters. Initially, fitting the total flux of each region was carried out in the same manner as the individual pixel fits by fixing the emissivity index to 1.8 and 2.0, and allowing the emissivity index to vary. This method ran into issues when determining an initial mass to use in the fitting. If we used the same procedure as we did for the pixel fitting, equation 3.4, our initial masses would either converge on a local minimum or not be able to produce a useable fit. This was due to the Levenberg-Marquardt method not being able to efficiently step through the parameter space to find a useable minimum, or the method would converge to a local minimum instead of the global minimum. The behavior of the fitted parameters with respect to the initial mass is shown in Figure 3.8 for a variable emissivity index.

In order to prevent any false convergences, we established a range of emissivity index values from 1.6 to 2.9 with increments of 0.05 and found the best fit mass and temperature for each of these indices. This method ended up being significantly more robust than allowing the emissivity index to vary. The relationship between the initial mass and the fitted parameters with a fixed emissivity is shown in Figure 3.9, and shows the results are independent of the initial mass up to a cutoff point where the Levenberg-Marquardt method is unable to produce reliable fits. Determining the best emissivity index was decided by which value returned the lowest reduced  $\chi^2$  value. The reduced  $\chi^2$  and emissivity index plots are shown in Figure 3.10 for each of the regions of NGC3627, where the minimum value is marked by the red line. The best fit results using this method are shown in Table 3.6 using the opacity suggested by the Planck model and the fitted SEDs are shown in Figure 3.11.

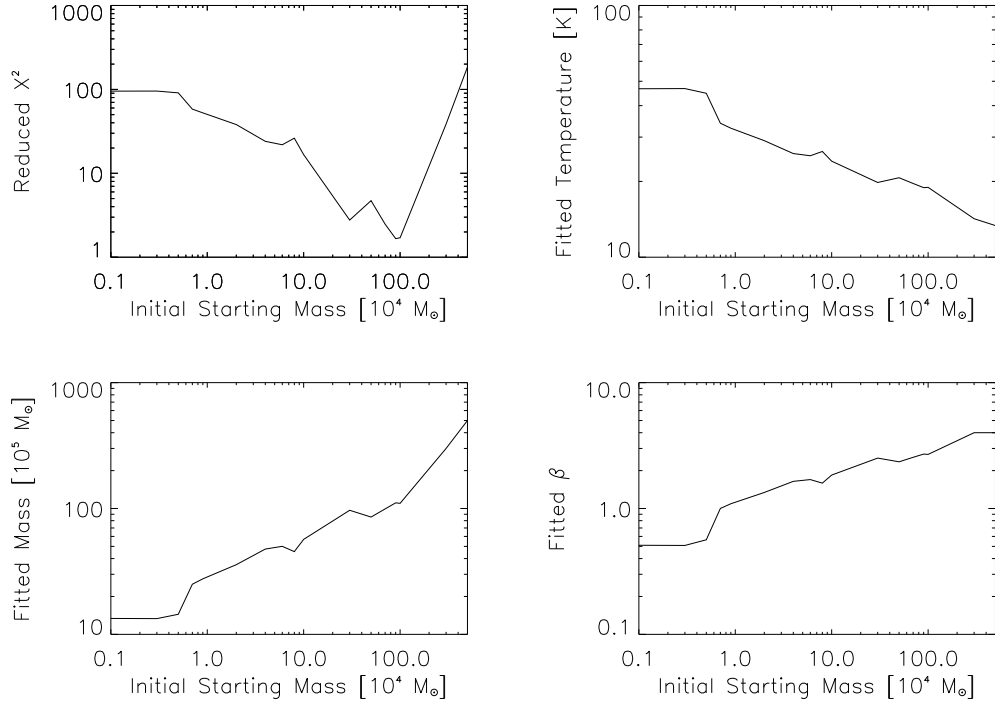


Figure 3.8: Returned SED fitting output for region 1 with Planck opacity for the  $\chi^2$ , temperature, mass, and emissivity index with varying initial mass. The top left panels shows the  $\chi^2$  values for each starting mass. The top right, bottom left, and bottom right panel show the returned temperatures, mass, and emissivity index.

Table 3.6. Best Fit Parameters for Planck Opacity Using Region Fluxes

Region	$\beta$	Mass [ $10^5 M_\odot$ ]	Mean Surface Density [ $M_\odot pc^{-2}$ ]	Temperature [K]
1	$2.20 \pm 0.03$	$70 \pm 5$	$0.14 \pm 0.01$	$22.8 \pm 0.5$
2	$2.30 \pm 0.03$	$19 \pm 1$	$0.18 \pm 0.01$	$22.5 \pm 0.3$
3	$2.35 \pm 0.03$	$9.5 \pm 0.6$	$0.21 \pm 0.01$	$23.3 \pm 0.3$
4	$2.30 \pm 0.03$	$23 \pm 1$	$0.22 \pm 0.01$	$22.2 \pm 0.2$
5	$2.00 \pm 0.03$	$11.4 \pm 0.8$	$0.093 \pm 0.007$	$22.3 \pm 0.4$
6	$1.95 \pm 0.03$	$4.6 \pm 0.3$	$0.087 \pm 0.006$	$23.9 \pm 0.4$

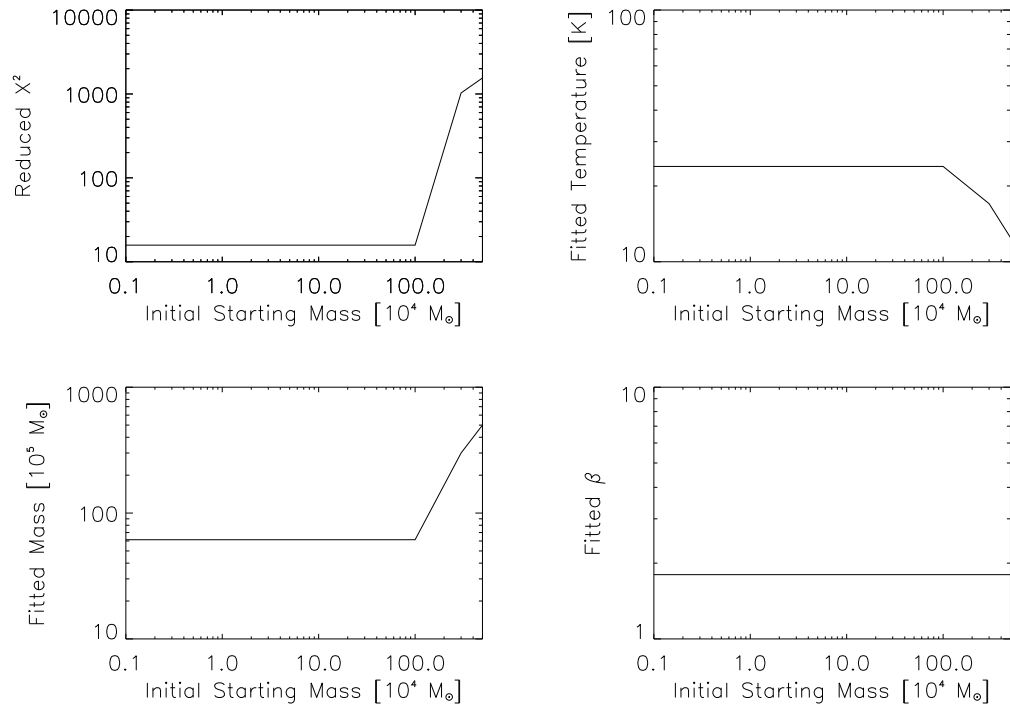


Figure 3.9: The same as Figure 3.8, however the emissivity index has been fixed to 1.8.



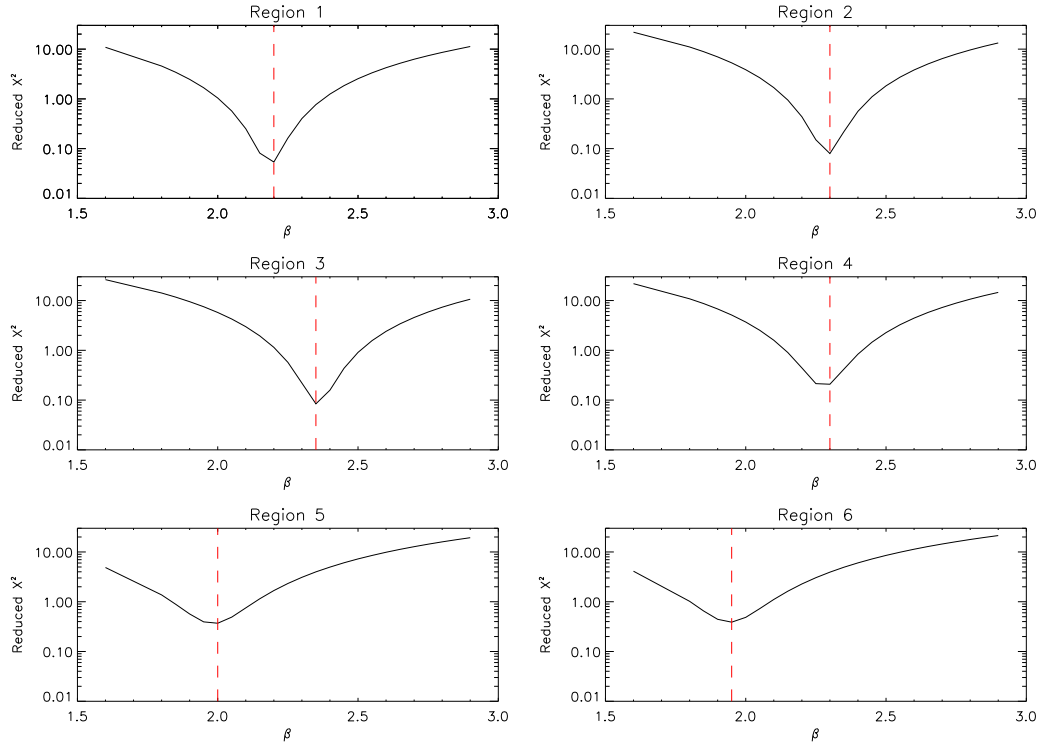
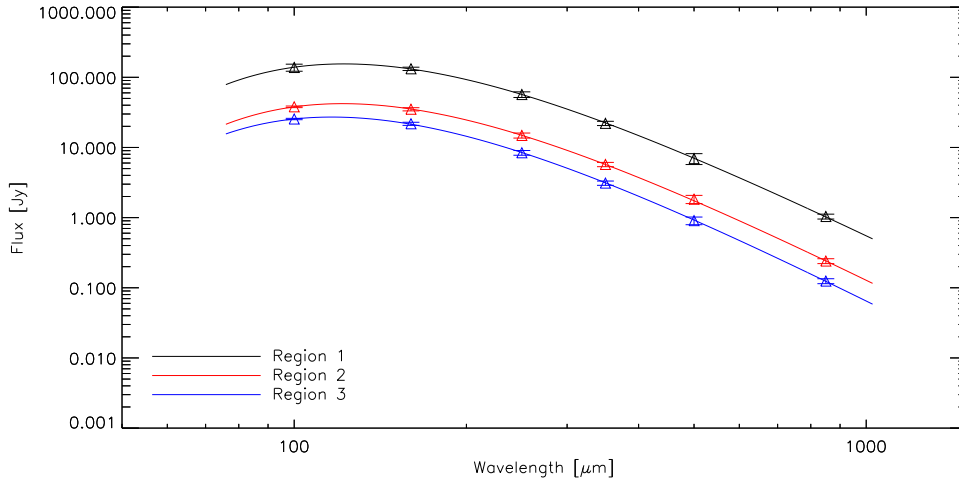
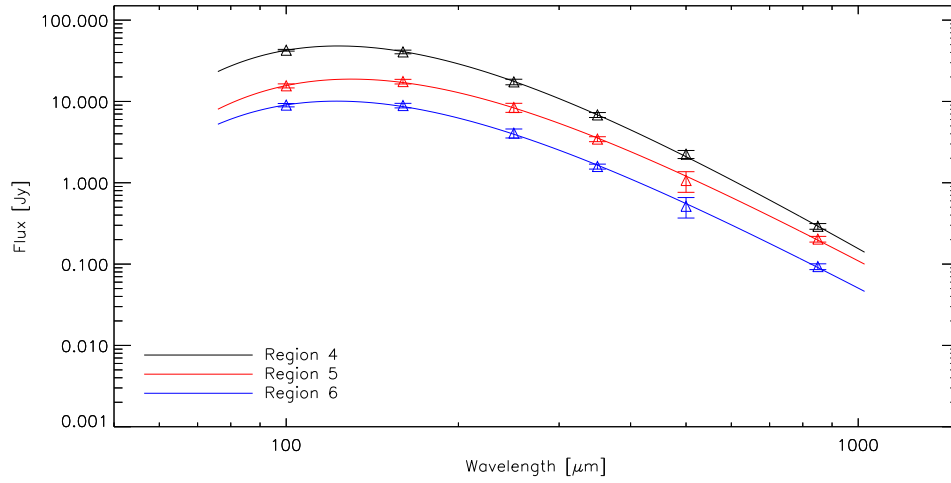


Figure 3.10: Plots for each region from figure 3.1 showing the Fixed emissivity index value and the resulting reduced  $\chi^2$  value.



(a) Regions 1, 2, and 3 SEDs



(b) Regions 4, 5, and 6 SEDs

Figure 3.11: SED fits for the flux of each region in Figure 3.1 using the Planck Opacity and allowing the emissivity index,  $\beta$  to vary.

## 3.3 Discussion

### 3.3.1 Reliability of Individual Pixel Fits

The issue of whether or not the individual pixel fits are reliable for a variable emissivity index is raised after seeing a strong dependence with the initial mass of the region SED fits shown in Figure 3.8. The argument can be made that since both fits have returned the same temperature ( $T_{pixel}=22\pm1$  K and  $T_{region}=22.8\pm0.5$  K), emissivity index ( $\beta_{pixel}=2.2\pm0.2$  and  $\beta_{region}=2.20\pm0.03$ ), and mass ( $M_{pixel}=85\pm38$   $M_{\odot}$  and  $M_{region}=82\pm6$   $M_{\odot}$ ), after the removal of any initial mass dependence for the region fits, the initial values for the pixel fits are able to locate the global minimum of the  $\chi^2$  space regardless of any dependence. The inability of the region fits to successfully converge was due to an overestimate of the initial mass, and was shown by the fitting routine returning the input parameters or the returned values would vary significantly given minor changes to the starting mass. The mass associated with the  $250\mu\text{m}$  flux using the 20 K Li and Draine model was scaling the peak of the SED to values larger than what would be expected using the Planck model which is the opacity used for the region fits. The difference between the two initial masses was large enough for the Levenberg-Marquardt method to fail at finding a minimum. This could be remedied by retooling the initial mass to use the Planck model; however by cycling through emissivity index values, we have provided a more reliable check to our pixel maps by breaking the dependency with the initial mass.

### 3.3.2 Comparison with Previous Work

We can check the validity of our results by comparing them to previous SED fits using the KINGFISH data (Galametz et al., 2012). Their best fit parameters were  $T=20.2\text{K}\pm 1.4\text{K}$  and  $\beta=2.3\pm 0.2$  which agree within the uncertainties with our results of  $T=22\text{K}\pm 1\text{K}$  and  $\beta=2.2\pm 0.2$  for a variable emissivity index. However, the dust mass reported by Galametz et al. (2012) was  $7.82^{+0.80}_{-0.66}\times 10^7 M_{\odot}$  using the opacity model from Li and Draine, and our reported dust mass for the region fits was  $7.0\pm 0.5\times 10^6 M_{\odot}$  using the Planck opacity. To check the agreement between our mass and that of Galametz et al. (2012) we need to take into account several differences in the two analyses. The differences consist of a lower flux from the extended structure removal in our data set, the opacity values used, which wavelength was used to calculate the mass, and finally how an increase or decrease in the temperature or emissivity index can affect the mass.

If we use the equation for mass given in Parkin et al. (2012) for Centaurus A, we can extract the distance from the constant to get

$$M = 364 D_{Mpc}^2 S_{250\mu m} (e^{57.58/T} - 1) \quad (3.5)$$

We use equation 3.5 for a simple comparison of our fit with that of Galametz et al. (2012) based on only the temperature and observed flux at  $250\mu m$ . With our regional flux, we get a mass of  $2.29\times 10^7 M_{\odot}$  using our temperature of 22 K and  $S_{250\mu m}=56$  Jy from the sum of the  $250\mu m$  pixels used to generate the maps shown in Figure 3.7. Using the temperature of 20 K and  $S_{250\mu m} = 96.7$  Jy from Galametz et al. (2012) gives a mass of  $5.22\times 10^7 M_{\odot}$ . The disagreement in the

masses can be partly attributed to the difference in temperatures; however, this will only decrease the mass calculated using the values from Galametz et al. (2012) by 25% which still leaves their mass higher than our mass. The lower mass can also be attributed to our lower fluxes which are due to the extended emission removal and any calibration differences between the two data sets as well as any corrections that were applied in Galametz et al. (2012) to calculate their flux. The difference in fluxes will decrease the mass using the information from Galametz et al. (2012) by another 42%, bringing the two masses into agreement.

### 3.3.3 Effects of 850 $\mu$ m Emission

The major difference between our work on NGC3627 and the work done in Galametz et al. (2012) is the presence of the 850 $\mu$ m data point. We tested the effect of the 850 $\mu$ m data by excluding it from our fits. The returned values for a variable emissivity index are shown in Table 3.7. The presence of the 850 $\mu$ m has little effect on the returned parameters.

The absence of a significant change in the returned parameters indicates a lack of any excess submillimeter emission, which can be indicative of an abundance of a very cold ( $T \lesssim 10\text{K}$ ) dust component (Dale et al., 2012). This excess in emission is typically seen in low-metallicity systems such as dwarf galaxies (Madden et al., 2011). The dwarf galaxies showing an excess typically have a metallicity of  $\log(\text{O}/\text{H}) + 12 \lesssim 8.3$  (Rémy-Ruyer et al., 2013). An 870 $\mu$ m excess has also been seen in NGC3627 (Galametz et al., 2014), but our results show no excess of emission at 850 $\mu$ m (evident in Figures 3.4, 3.5,

Table 3.7. Best Fit Parameters Excluding  $850\mu\text{m}$  Emission Using Planck Opacity with Variable Emissivity Index

Region	Average $\beta$	Total Mass [ $10^5 M_\odot$ ]	Average Surface Density [ $M_\odot pc^{-2}$ ]	Average Temperature [K]
1	$2.3 \pm 0.3$	$75 \pm 28$	$0.15 \pm 0.06$	$22 \pm 2$
2	$2.3 \pm 0.3$	$18 \pm 5$	$0.17 \pm 0.05$	$23 \pm 2$
3	$2.4 \pm 0.2$	$10 \pm 1$	$0.19 \pm 0.02$	$23 \pm 1$
4	$2.2 \pm 0.2$	$22 \pm 5$	$0.21 \pm 0.05$	$23 \pm 2$
5	$2.3 \pm 0.2$	$14 \pm 3$	$0.11 \pm 0.03$	$21 \pm 1$
6	$2.2 \pm 0.2$	$5 \pm 1$	$0.10 \pm 0.02$	$22 \pm 1$

and 3.6). The discrepancy between our results and those of Galametz et al. (2014) may be attributed to their treatment of the removal of the CO J=3-2 emission from their data and possibly to how their  $870\mu\text{m}$  data were processed. If their image processing method does not remove extended emission (unlike SCUBA-2), then submillimeter excess might be attributed to diffuse emission regions that are absent in our analysis. However, we would not expect to see any submillimeter excess given that  $\log(\text{O}/\text{H}) + 12 = 8.99$  for NGC3627 (Moustakas et al., 2010), well above the estimated threshold where the  $850\mu\text{m}$  excesses are typically found.

## Chapter 4

### Dust-to-Gas Ratio and $\alpha_{CO}$

#### 4.1 Minimizing the Scatter in the Dust-to-Gas Ratio

In order to determine the amount of molecular hydrogen present, we have chosen to use the dust based method to determine the CO-to-H<sub>2</sub> conversion factor. In our analysis we have used the conversion factor  $\alpha_{CO}$  which will return the amount of molecular hydrogen present in units of surface density. Calculating the amount of molecular hydrogen present with this method involves minimizing the scatter in the dust to gas ratio for a collection of pixels in a region. The dust-to-gas ratio is calculated using

$$\delta_{DGR} = \frac{\Sigma_{dust}}{I_{CO} * \alpha_{CO} + \Sigma_{HI}} \quad (4.1)$$

where  $\delta_{DGR}$  is the ratio of the surface densities of the dust and gas present in the system,  $\Sigma_{dust}$  is the surface density of the dust in  $M_{\odot} \text{ pc}^{-2}$ ,  $I_{CO}$  is the CO intensity in  $\text{K km s}^{-1}$ ,  $\alpha_{CO}$  is the conversion factor in units of  $M_{\odot} \text{ pc}^{-2} (\text{K km s}^{-1})^{-1}$ , and  $\Sigma_{HI}$  is the surface density of the atomic hydrogen in  $M_{\odot} \text{ pc}^{-2}$ . The

scatter of the dust-to-gas ratio is determined by finding the standard deviation of the dust-to-gas ratios for the pixels assuming a Gaussian distribution.

In addition, the atomic hydrogen surface density map had a cut applied to it where any points below 20% of the maximum surface density were set to zero. Applying this cut removed all but two of the pixels associated with the nuclear region (region 3 from Figure 3.1). By removing most of the data, the variation of the scatter in the dust-to-gas ratio with  $\alpha_{CO}$  does not show as dramatic an upturn at higher  $\alpha_{CO}$  as other regions do. Therefore region 3 has been omitted from our analysis.

The best fit values for  $\delta_{DGR}$  and  $\alpha_{CO}$  were determined using the dust surface densities found in Chapter 3 for both the Planck and the Li and Draine models. The  $\alpha_{CO}$  variable was handled by assigning it a single value over the range of 0.01 to 100  $M_{\odot} \text{ pc}^{-2} (\text{K km s}^{-1})^{-1}$ , and the best-fit  $\alpha_{CO}$  was determined by the value resulting in the lowest scatter in the dust-to-gas ratio for the pixels of each region from Figure 3.1. In addition, a 7<sup>th</sup> region was added that is the galaxy without the nucleus. This 7<sup>th</sup> region was created to accommodate the lack of HI emission in the nucleus of NGC3627. Once the best  $\alpha_{CO}$  is found, the surface density of molecular hydrogen is then determined by scaling the CO intensity by the calculated conversion factor. Finally, the dust-to-gas ratio is found by dividing the dust surface density by the sum of the HI and H<sub>2</sub> surface densities.

The results using the Planck model with the CO J=1-0 line are shown in Figure 4.1 where the left panel shows the value of the dust-to-gas ratio in each pixel versus the H<sub>2</sub> to HI ratio, with the solid red line indicating the mean



value for the dust-to-gas ratio, and the dotted lines showing the standard deviation of the dust-to-gas ratio. The right panels of Figure 4.1 show the scatter in the dust-to-gas ratio as a function of the  $\alpha_{CO}$  value adopted. The numerical values of the dust-to-gas ratio,  $\alpha_{CO}$ , and  $H_2$  surface density using both the Planck and the Li and Draine dust masses are shown in Table 4.1. The behavior of the mean dust-to-gas ratio as a function of  $\alpha_{CO}$  is shown in Figure 4.2, and shows that as the conversion factor is increased the amount of gas increases, and with a fixed dust surface density, the dust-to-gas ratio decreases. The error in the dust-to-gas ratio in Table 4.1 is the same as the minimum scatter found in Figure 4.1, and the error reported for  $\alpha_{CO}$  is half of the spacing between the values used to calculate the minimum scatter.

While CO J=1-0 is the standard molecular tracer of  $H_2$  (Bolatto et al., 2013), these observations are not always available. When CO J=1-0 data is not available, an alternative rotational transition of CO is used. For example, Sandstrom et al. (2013) used the CO J=2-1 transition, and Warren et al. (2010) used the CO J=3-2 transition, where the observations were scaled to the expected intensity of the CO J=1-0 using a ratio of the observed CO transition to the CO J=1-0 transition. We have measured the CO J=2=1 / J=1-0 line ratio to be 0.39 for the galaxy as a whole, and can examine the effects of using this technique to approximate the CO J=1-0 transition in this method. The results for the dust-to-gas ratio,  $\alpha_{CO}$ , and  $H_2$  surface density are shown using CO J=2-1 in Table 4.2.

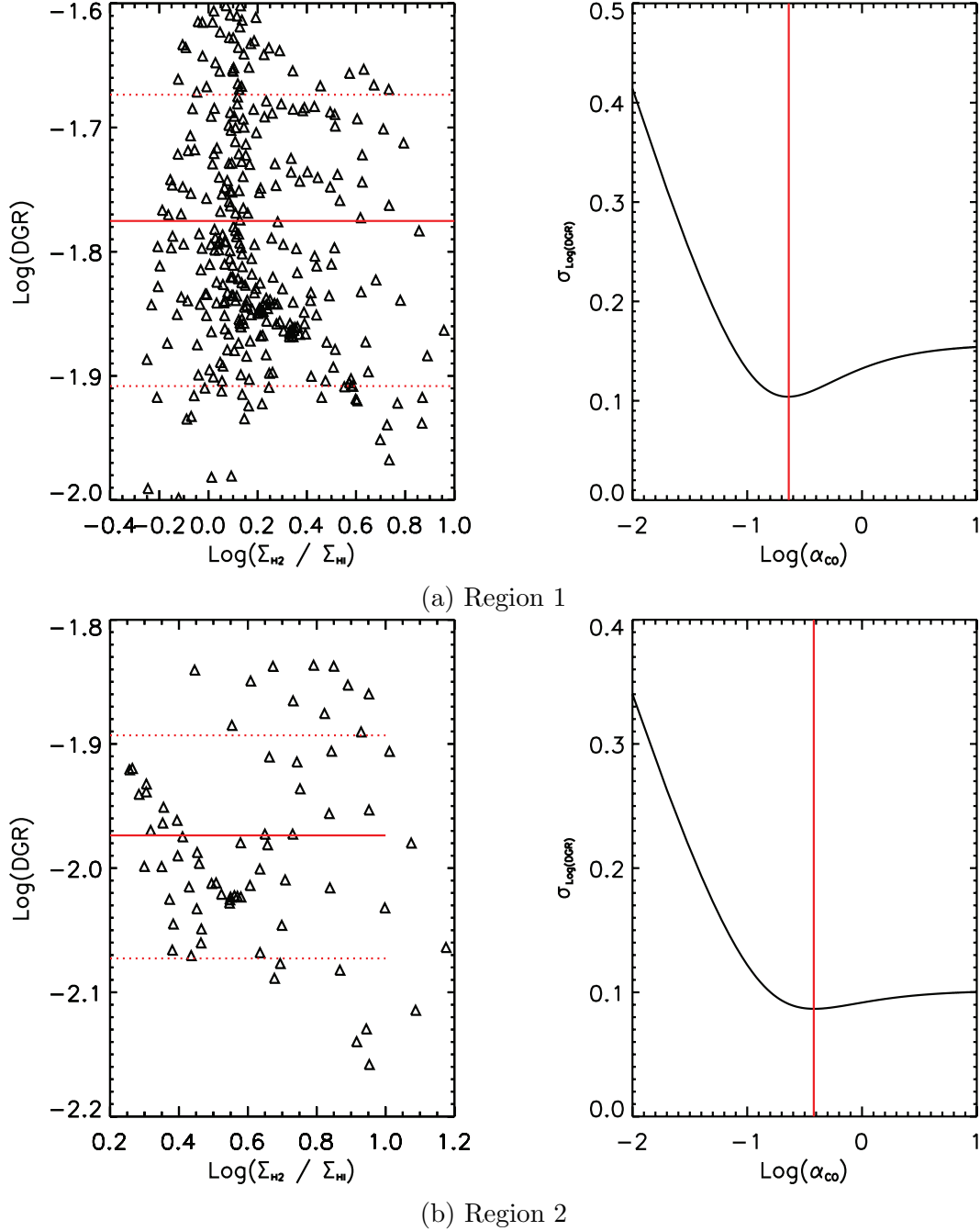
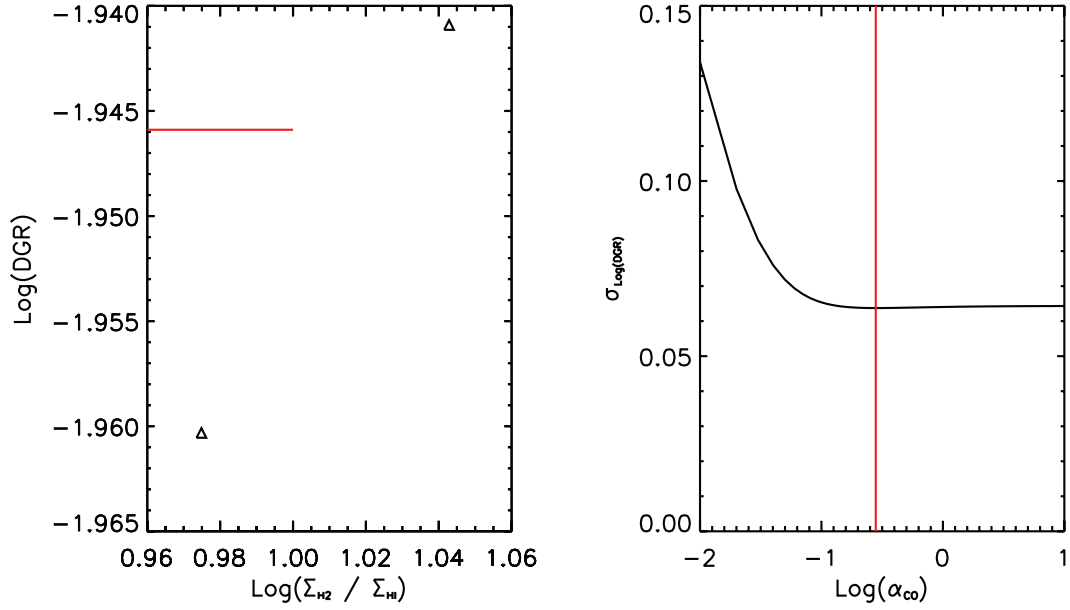
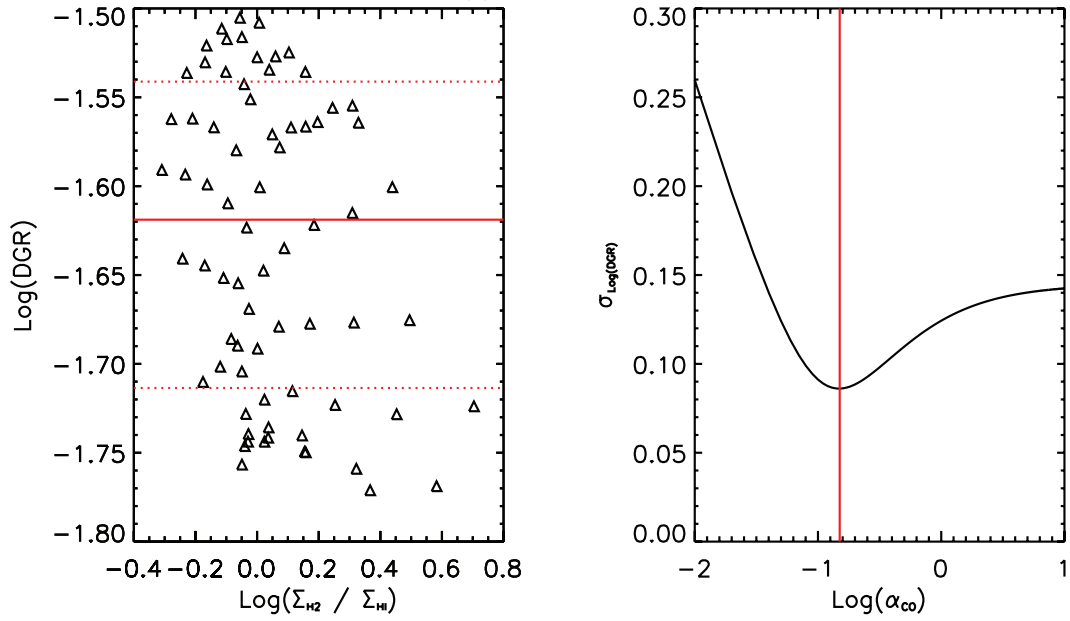


Figure 4.1: Plots of the dust-to-gas ratio vs the  $\text{H}_2$  to HI surface density using the best fit  $\alpha_{\text{CO}}$  (left) and the scatter in the dust-to-gas ratio as a function of  $\alpha_{\text{CO}}$  (right). Each parameter was calculated using the CO J=1-0 line and the Planck dust model.

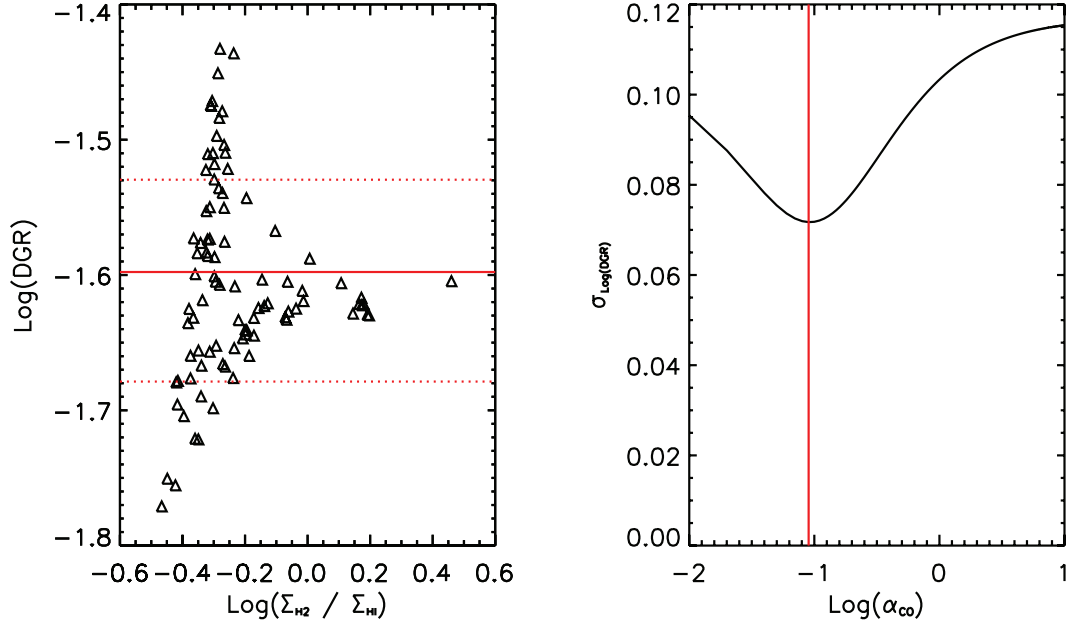


(c) Region 3

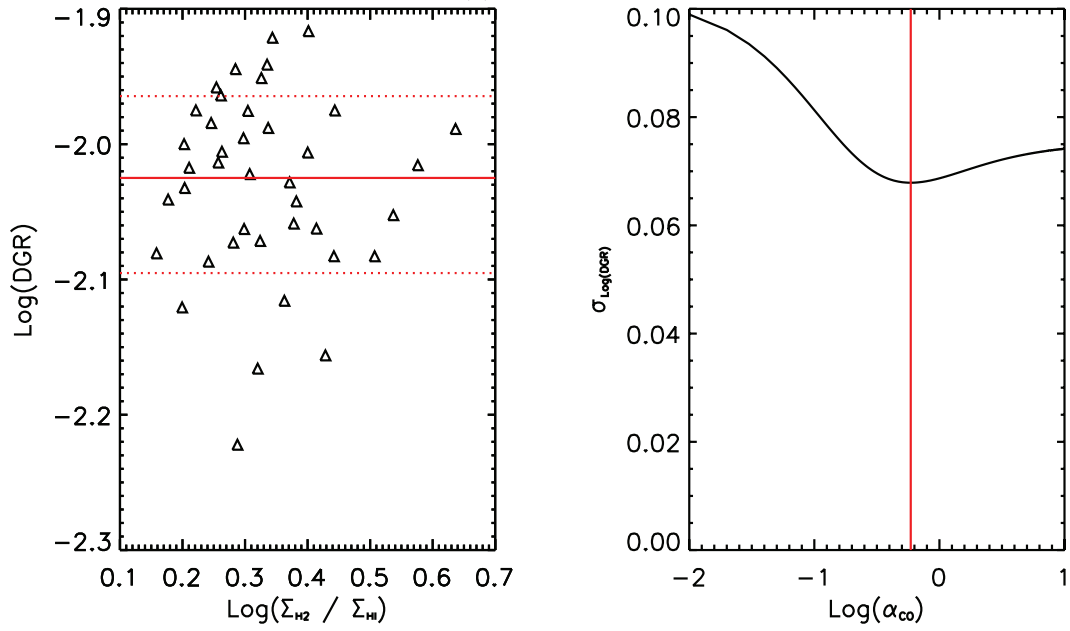


(d) Region 4

Figure 4.1: (continued)



(e) Region 5



(f) Region 6

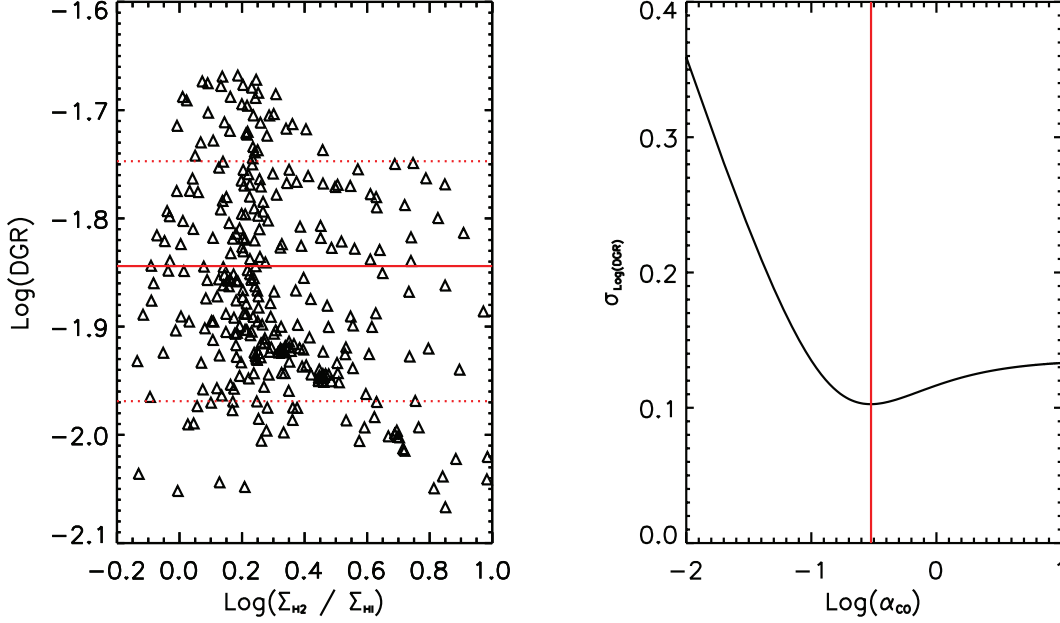
Figure 4.1: (continued)

Table 4.1. Dust-to-gas ratio,  $\alpha_{CO}$ , and  $H_2$  Surface Density using CO J=1-0 as the  $H_2$  Tracer

Opacity Model	Dust-to-Gas Ratio	$\alpha_{CO}$ [ $M_\odot \text{ pc}^{-2} (\text{K km s}^{-1})^{-1}$ ]	Average $\Sigma_{H_2}$ per Pixel [ $M_\odot \text{ pc}^{-2}$ ]
Region 1			
Planck	$0.017 \pm 0.004$	$0.230 \pm 0.005$	$4 \pm 3$
Li and Draine	$0.07 \pm 0.02$	$0.230 \pm 0.005$	$4 \pm 3$
Region 2			
Planck	$0.011 \pm 0.002$	$0.380 \pm 0.005$	$10 \pm 3$
Li and Draine	$0.044 \pm 0.009$	$0.410 \pm 0.005$	$11 \pm 4$
Region 4			
Planck	$0.024 \pm 0.005$	$0.150 \pm 0.005$	$4 \pm 2$
Li and Draine	$0.11 \pm 0.02$	$0.150 \pm 0.005$	$4 \pm 1$
Region 5			
Planck	$0.03 \pm 0.09$	$0.090 \pm 0.005$	$1.2 \pm 0.6$
Li and Draine	$0.11 \pm 0.02$	$0.100 \pm 0.005$	$1.4 \pm 0.6$
Region 6			
Planck	$0.010 \pm 0.001$	$0.590 \pm 0.005$	$6 \pm 1$
Li and Draine	$0.040 \pm 0.006$	$0.610 \pm 0.005$	$6 \pm 1$
No Nucleus			
Planck	$0.014 \pm 0.004$	$0.300 \pm 0.005$	$5 \pm 3$
Li and Draine	$0.06 \pm 0.02$	$0.310 \pm 0.005$	$5 \pm 3$

Table 4.2. Dust-to-gas ratio,  $\alpha_{CO}$ , and  $H_2$  Surface Density using CO J=2-1 as the  $H_2$  Tracer

Opacity Model	Dust-to-Gas Ratio	$\alpha_{CO}$ [ $M_\odot \text{ pc}^{-2} (\text{K km s}^{-1})^{-1}$ ]	Average $\Sigma_{H_2}$ per Pixel [ $M_\odot \text{ pc}^{-2}$ ]
Region 1			
Planck	$0.01 \pm 0.01$	$0.390 \pm 0.005$	$8 \pm 5$
Li and Draine	$0.048 \pm 0.01$	$0.410 \pm 0.005$	$8 \pm 5$
Region 2			
Planck	$0.0128 \pm 0.004$	$0.310 \pm 0.005$	$8 \pm 3$
Li and Draine	$0.054 \pm 0.003$	$0.330 \pm 0.005$	$8 \pm 3$
Region 4			
Planck	$0.0085 \pm 0.004$	$0.520 \pm 0.005$	$15 \pm 1$
Li and Draine	$0.037 \pm 0.005$	$0.540 \pm 0.005$	$16 \pm 6$
Region 5			
Planck	$0.013 \pm 0.008$	$0.340 \pm 0.005$	$4 \pm 1$
Li and Draine	$0.054 \pm 0.008$	$0.360 \pm 0.005$	$5 \pm 2$
Region 6			
Planck	$0.0108 \pm 0.004$	$0.450 \pm 0.005$	$5 \pm 1$
Li and Draine	$0.037 \pm 0.004$	$0.460 \pm 0.005$	$5 \pm 2$
No Nucleus			
Planck	$0.009 \pm 0.007$	$0.550 \pm 0.005$	$10 \pm 6$
Li and Draine	$0.034 \pm 0.008$	$0.580 \pm 0.005$	$10 \pm 6$



(g) Region 1 Without the Nucleus

Figure 4.1: (Continued)

## 4.2 Effects of the Dust Model and CO Treatment

The effects of the dust model (Planck vs Li and Draine) are mainly seen in the dust-to-gas ratio for the CO J=1-0 emission. Since the major difference in the two models was the resulting dust mass due to different reference opacity values, it is reasonable that the Li and Draine model produces larger dust-to-gas ratios since it has a smaller reference opacity. The values of  $\alpha_{\text{CO}}$  derived from the two dust models agree within uncertainty and the overall molecular gas surface densities all agree within error for each region for the two dust models. The same trend is seen when scaling the CO J=2-1 emission, where the dust-to-gas ratio of the Planck model is also smaller than the Li and Draine model.

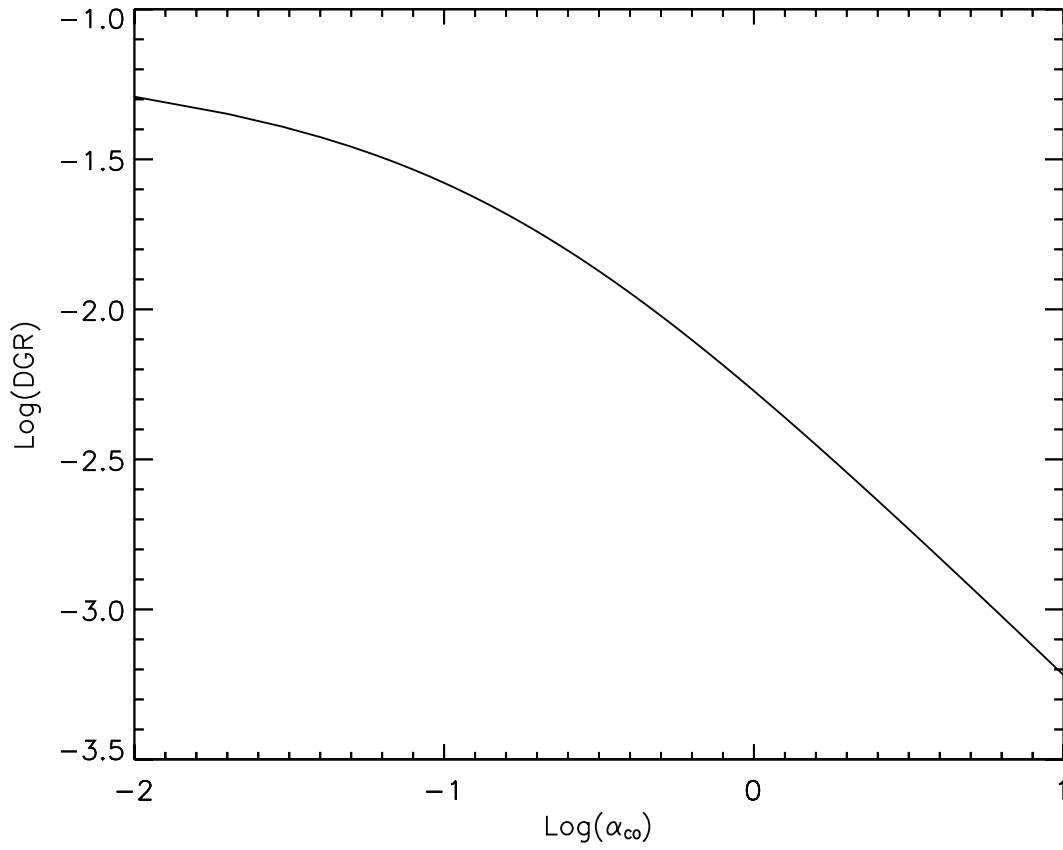


Figure 4.2: The dust-to-gas ratio as a function of  $\alpha_{CO}$  in region 1 without the nucleus. The dust model used is the Planck model with CO J=1-0 as the molecular gas tracer.



The difference in using either the CO J=1-0 or CO J=2-1 as the molecular hydrogen tracer is seen in the value of  $\alpha_{CO}$ . Using the CO J=2-1 emission with a 2-1/1-0 ratio applied, the conversion factor is significantly increased in regions 4 and 5, while the conversion factor is decreased in regions 2 and 6. The increase in regions 4 and 5 is large enough to increase the conversion factor for the galaxy as a whole despite the decrease in regions 2 and 6. Despite the change in  $\alpha_{CO}$  values in each region, we still see the same masses for all of the regions except for regions 4 and 5. The change in  $H_2$  surface densities are due to the behavior of the 2-1/1-0 ratio in these regions. Region 5 displays a large gradient in the 2-1/1-0 ratio from north to south along the spiral arm, and the factor of 4 change in region 4 is due to the entire region's 2-1/1-0 ratio being nearly double the mean value of the galaxy.

The difference in  $\alpha_{CO}$  between the CO J=1-0 emission and the converted CO J=2-1 emission raises the question of which value we should trust. The answer lies primarily in whether we are concerned with the dense or diffuse molecular ISM, or the dense and less dense components of a GMC. If we are interested in the diffuse molecular ISM such as the outer regions of a GMC, Wilson & Scoville (1990) showed in M33 that over half of the CO J=1-0 emission is due to diffuse gas, so using this transition would be ideal. If the dense molecular ISM is being examined such as the inner regions of a GMC, then the CO J=2-1 emission would be more appropriate to determine the  $H_2$  abundance. Since we are not able to resolve individual GMCs and are interested in the overall molecular ISM of NGC3627, both play a role in understanding the abundance of  $H_2$  in the system since both the dense areas

of a GMC traced by CO J=2-1 and less dense areas of a GMC traced by CO J=1-0 will be present in all of the regions being analyzed.

### 4.3 Comparison of Results with Previous Work

If NGC3627 were to have Milky Way like values for  $\alpha_{CO}$ , we would expect  $\alpha_{CO} \approx 4 \text{ M}_{\odot} \text{ pc}^{-2}$  (Sandstrom et al., 2013). However, the  $\alpha_{CO}$  values calculated using the the CO J=2-1 emission suggest NGC3627 is similar to U/LIRG type galaxies whose  $\alpha_{CO}$  range is more like  $0.3 - 1.3 \text{ M}_{\odot} \text{ pc}^{-2} (\text{K km s}^{-1})^{-1}$  (Downes & Solomon, 1998). The results using the CO J=1-0 emission fall below even the U/LIRG range. Even our smallest dust-to-gas ratio lies above the typical values found in late type galaxies of  $0.005 - 0.01$  (Smith et al., 2012). If we compare our Li and Draine results to values recently calculated using the same method by Sandstrom et al. (2013), we find that our conversion factor is much lower than their average for NGC3627 of  $1.2 \text{ M}_{\odot} \text{ pc}^{-2} (\text{K km s}^{-1})^{-1}$ , and our dust-to-gas ratio is much larger than their average of  $\approx 0.017$ .

The low  $\alpha_{CO}$  and high dust-to-gas ratios are likely due to the filtering process applied to our data (§2.3), in particular, the amount of the HI surface density removed by the filtering. If the HI emission is small, the product of  $I_{CO}\alpha_{CO}$  will dominate the denominator of equation 4.1 essentially removing the  $\Sigma_{HI}$  term. The effect of this would result in

$$\delta_{dgr}\alpha_{CO} = \frac{\Sigma_{dust}}{I_{CO}} \quad (4.2)$$

where the degeneracy between  $\delta_{dgr}$  and  $\alpha_{CO}$  is apparent. By removing a significant portion of the HI surface density we have weakened the constraint of the method, and strengthened the possibility for degeneracy.

As a crude test, we used the unfiltered gas data with the filtered Li and Draine dust surface densities to establish comparable values with the results reported by Sandstrom et al. (2013). This process gives the results shown in Table 4.3 and a plot similar to Figure 4.1 for region 1 with the nucleus removed is shown in Figure 4.3. The unfiltered mean dust-to-gas ratio is shown as a function of  $\alpha_{CO}$  in Figure 4.4 where the increase in the HI surface density has introduced a plateau at low values for  $\alpha_{CO}$ . Removing the filtering has increased the CO J=2-1 results to be in reasonable agreement with the values from Sandstrom et al. (2013) over region 1. The lower dust-to-gas ratios are primarily attributed to the spatial filtering that has occurred, but can also be linked to how the dust mass was calculated. Using the method we used to determine the dust mass by fitting a single blackbody fit over the cold component can lead to a dust mass nearly a factor of two larger compared to the approach taken by Sandstrom et al. (2013) of using the entire infrared spectrum (Dale et al., 2012).

## 4.4 Caveats Due to Uncertainty Estimation

The values for the uncertainty associated with our best fit  $\alpha_{CO}$  come from the step size used when calculating the minimum dust-to-gas ratio scatter. Comparing region 1 and the region without the nucleus, we would expect the results from the fitting to be the same since the difference is only two points. In

Table 4.3. CO Transition,  $\alpha_{CO}$ , and H<sub>2</sub> Surface Density using the Li and Draine dust model with No Spatial Filtering of CO or HI

Region	Dust-to-Gas Ratio	$\alpha_{CO}$ [M <sub>⊙</sub> pc <sup>-2</sup> (K km s <sup>-1</sup> ) <sup>-1</sup> ]	Average $\Sigma_{H_2}$ per Pixel [M <sub>⊙</sub> pc <sup>-2</sup> ]
Region 1			
J=1-0	0.013 ± 0.003	0.880 ± 0.005	21 ± 10
J=2-1	0.010 ± 0.001	1.520 ± 0.005	32 ± 18
Region 2			
J=1-0	0.011 ± 0.002	1.130 ± 0.005	33 ± 11
J=2-1	0.0106 ± 0.0009	1.360 ± 0.005	36 ± 15
Region 4			
J=1-0	0.035 ± 0.006	0.130 ± 0.005	4 ± 1
J=2-1	0.013 ± 0.001	1.170 ± 0.005	36 ± 12
Region 5			
J=1-0	0.013 ± 0.001	0.720 ± 0.005	14 ± 5
J=2-1	0.009 ± 0.0009	1.98 ± 0.005	28 ± 9
Region 6			
J=1-0	0.0050 ± 0.0007	3.780 ± 0.005	53 ± 8
J=2-1	0.0065 ± 0.0007	3.090 ± 0.005	35 ± 10
No Nucleus			
J=1-0	0.009 ± 0.002	1.470 ± 0.005	32 ± 14
J=2-1	0.0076 ± 0.0009	2.260 ± 0.005	43 ± 25

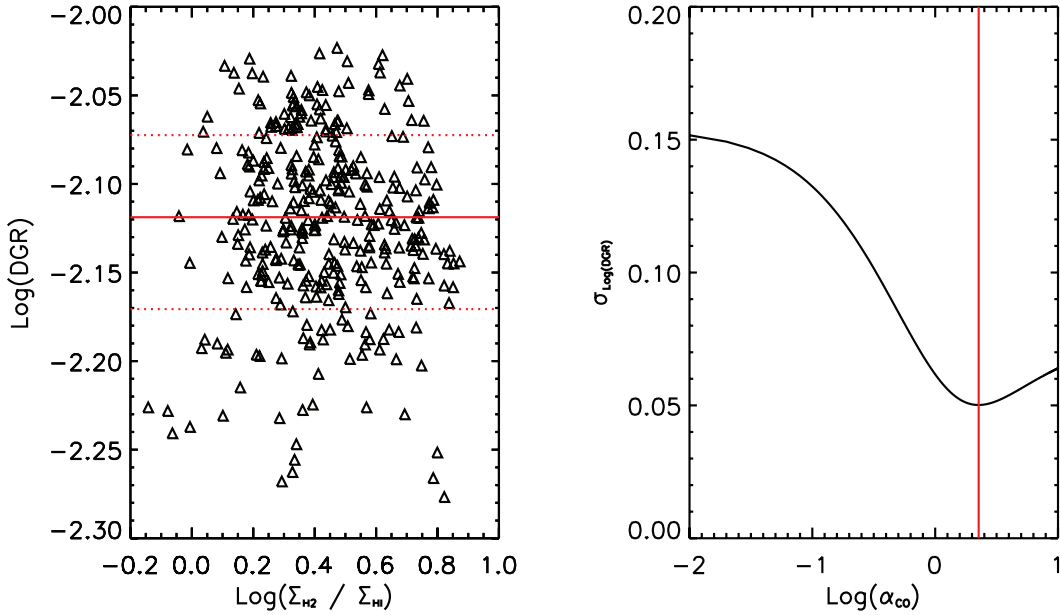


Figure 4.3: Plots of the dust-to-gas ratio vs the  $\text{H}_2$  to HI surface densities using the best fit  $\alpha_{\text{CO}}$  (left) and the scatter in the dust-to-gas ratio as a function of  $\alpha_{\text{CO}}$  (right). The plots were made using the Li and Draine dust model with the CO J=2-1 molecular tracer with the extended emission in the HI and CO J=2-1 data.

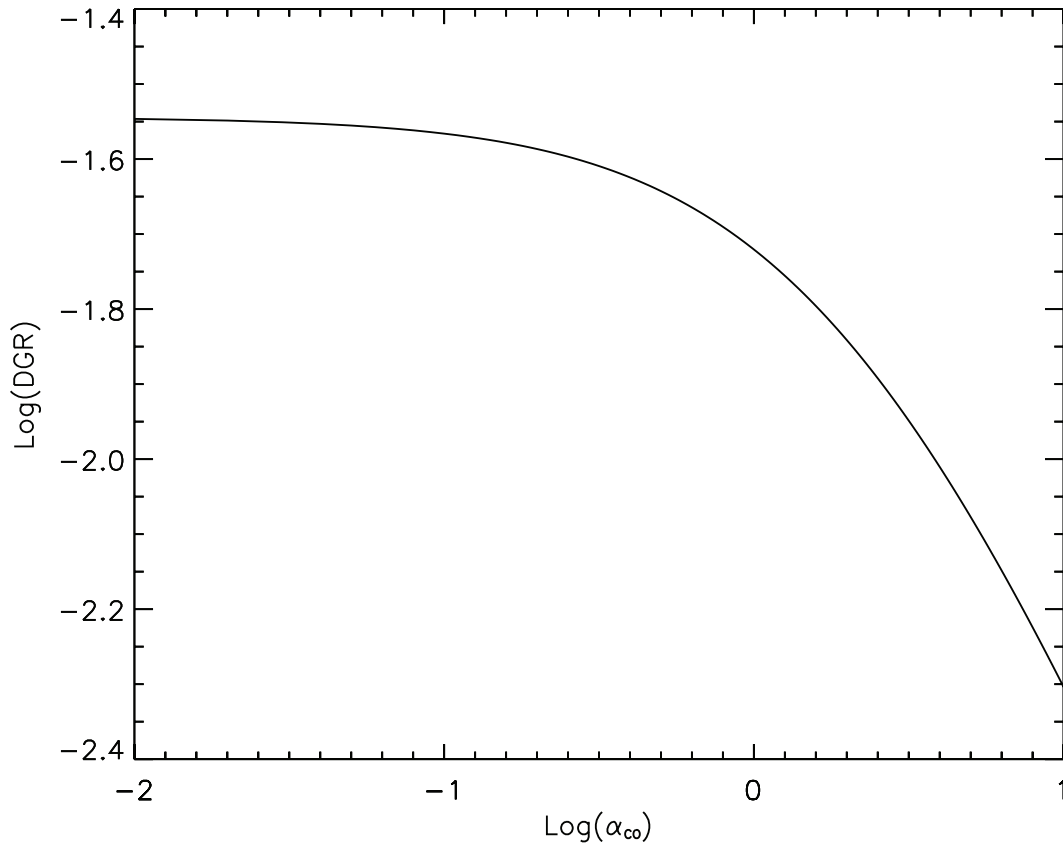


Figure 4.4: The mean dust-to-gas ratio as a function of  $\alpha_{CO}$  in region 1 with the nucleus removed using the Li and Draine dust model and the CO J=2-1 emission as the molecular tracer without any extended emission filtering in the HI or CO J=2-1 data.

Tables 4.1 and 4.2, we see that excluding these two points did not change the dust-to-gas ratio significantly, but did lead to  $\alpha_{CO}$  values that differed by 0.07-0.17  $M_{\odot} \text{ pc}^2 (\text{K km s}^{-1})^{-1}$  which is greater than our reported uncertainty in  $\alpha_{CO}$ . The change in  $\alpha_{CO}$  over these two regions suggests that we have underestimated the uncertainty in this parameter. Furthermore, if we adopt the difference of 0.07 as our uncertainty in  $\alpha_{CO}$  and convert it to its log space equivalent of 0.13, we can apply this as a horizontal error bar in Figure 4.1. If our error bars overlap the portion of the plot to the right of the  $\alpha_{CO}$  minimum where the scatter begins to converge to a single value, then the fitted  $\alpha_{CO}$  represents more of a minimum value of  $\alpha_{CO}$  for the system rather than the actual value.

## Chapter 5

### Summary

We have shown two new continuum maps of NGC3627 at  $450\mu\text{m}$  and  $850\mu\text{m}$  from SCUBA-2 and analyzed them with the goal of determining a dust-to-gas mass ratio, a suitable CO-to-H<sub>2</sub> conversion factor, and the amount of molecular hydrogen present, both in the galaxy as a whole and in 5 individual regions picked based upon the morphological features of the galaxy. In order to produce our results we utilized data from the KINGFISH survey (Kennicutt et al., 2011) and the NGLS (Wilson et al., 2012) to calculate a dust mass using SED fitting on a pixel by pixel basis and also for the total flux of each region. The dust-to-gas ratio,  $\alpha_{CO}$ , and molecular gas surface density were determined using a minimization of the dust-to-gas ratio scatter in the galaxy using data from the Nobeyama 45-m CO J=1-0 survey (Kuno et al., 2007), HERACLES (Reuter et al., 1996), and THINGS (Walter et al., 2008). The important results from our analysis are as follows:

1. We have created high quality images of NGC3627 using the Starlink program MAKEMAP by incorporating masks in the AST and FLT portions



of MAKEMAP and adding a high-pass filter of  $175''$  in the FLT portion of MAKEMAP in order to reduce the noise in the final image products.

2. Using results from the KINGFISH survey (Kennicutt et al., 2011), we were able to show an excess emission was present in the SCUBA-2  $450\mu\text{m}$  observations that was more likely due to calibration or mapping issues rather than a physical process in the ISM of NGC3627.
  
3. The results of the SED analysis were tested using two competing dust models calculated by the Planck observation group (Planck Collaboration et al., 2011) and Li and Draine (Li & Draine, 2001). A third model was tested using the opacity values from the Planck model with an emissivity index that was allowed to vary. All three models were applied to the 5 regions of NGC3627 and the galaxy as a whole. The results are shown in Tables 3.3, 3.4, 3.5, and 3.6. The calculated temperatures for the entire galaxy are  $23\pm 2$  K,  $24\pm 2$  K,  $22\pm 1$  K, and  $22\pm 2$  K for the Planck model, Li and Draine model, free emissivity index, and regional flux, respectively. The calculated masses using the Planck opacity are  $52\pm 23 \times 10^5 M_{\odot}$ ,  $73\pm 31 \times 10^5 M_{\odot}$ , and  $75\pm 28 \times 10^5 M_{\odot}$  for the Planck model, free emissivity index, and regional flux, respectively. The mass returned for the Li and Draine model is  $230\pm 103 \times 10^5 M_{\odot}$ . When the emissivity index was allowed to vary the returned values were  $2.2\pm 0.2$  and  $2.3\pm 0.3$  for the pixel by pixel fits and regional flux fits, respectively. The results from the fitting agreed with previous work by Galametz et al. (2012).

4. There was no observed excess emission at  $850\mu\text{m}$  in our fits, in contrast to the results of Galametz et al. (2014) using  $870\mu\text{m}$  maps from LABOCA. The difference in the two results can be attributed to how they handled the molecular contribution at  $870\mu\text{m}$  and whether the reduction process they used for the  $870\mu\text{m}$  emission preserved any extended features suggesting the excess emission can be attributed to extended emission.
5. Using the Planck and the Li and Draine dust models to determine the dust-to-gas ratio showed that the Li and Draine model yielded higher dust-to-gas ratios than the Planck model. This is due to the Li and Draine model having a higher dust surface density.
6. Using either the CO J=1-0 line or scaling the CO J=2-1 line using a 2-1/1-0 ratio does not affect the dust-to-gas ratio, but does change the CO-to-H<sub>2</sub> conversion factor. Using the scaled CO J=2-1 emission results in higher CO-to-H<sub>2</sub> conversion factors, perhaps because the CO J=1-0 emission may trace more diffuse gas (Wilson & Scoville, 1990) where atomic hydrogen will be more dominant than its molecular counterpart.
7. The gas data with the extended emission removed yielded  $\alpha_{CO}$  values typical of U/LIRGs. This was likely due to the significant portion of the HI emission that is made up of extended emission. This extended HI emission was removed by the filtering process, which greatly decreased the HI surface density. When using unfiltered gas data, we recovered conversion factors and dust-to-gas ratios similar to the results of Sandstrom et al. (2013) using the same H<sub>2</sub> tracer.

Future work on NGC3627 and the NGLS SCUBA-2 catalogue would include:

1. Investigating the excess emission in the  $450\mu\text{m}$  image to determine its source. If the source of this excess  $450\mu\text{m}$  emission could be found, the resolution of our analysis could be improved and higher quality SED fitting could take place.
2. Using a bootstrap or similar error estimation method in order to obtain more reliable uncertainties on  $\alpha_{CO}$  to gain more reliable errors on the dust-to-gas ratio and to determine the quality of the fits.
3. Implementing a MCMC method to determine  $\alpha_{CO}$  values for each pixel would help to decrease the overall scatter of the dust-to-gas ratio and provide dust-to-gas ratio,  $\alpha_{CO}$ , and  $\text{H}_2$  surface density maps to go with the SED fitting maps. These maps could be used to determine correlations in  $\alpha_{CO}$  with parameters returned from the SED fitting.
4. Implementing the SED and dust-to-gas ratio analysis for other targets in the NGLS catalogue would allow for a large scale statistical survey over the properties of the dust in the galaxies in local Universe.

## Bibliography

- Abel, T., Anninos, P., Zhang, Y., & Norman, M. L. 1997, *New A*, 2, 181
- Abergel, A., Ade, P. A. R., Aghanim, N., et al. 2013, *ArXiv e-prints*, arXiv:1312.1300
- Barrett, A. H. 1964, *Nature*, 202, 475
- Bolatto, A. D., Wolfire, M., & Leroy, A. K. 2013, *ARA&A*, 51, 207
- Boulanger, F., Abergel, A., Bernard, J.-P., et al. 1996, *A&A*, 312, 256
- Braine, J., Gratier, P., Kramer, C., et al. 2010, *A&A*, 518, L69
- Burden, R. L., & Faires, J. D. 2001, *Numerical analysis*
- Calzetti, D., Wu, S.-Y., Hong, S., et al. 2010, *ApJ*, 714, 1256
- Chapin, E. L., Berry, D. S., Gibb, A. G., et al. 2013, *MNRAS*, 430, 2545
- Dale, D. A., Aniano, G., Engelbracht, C. W., et al. 2012, *ApJ*, 745, 95
- Dempsey, J. T., Friberg, P., Jenness, T., et al. 2013, *MNRAS*, 430, 2534
- Dobbs, C. L., Krumholz, M. R., Ballesteros-Paredes, J., et al. 2013, *ArXiv e-prints*, arXiv:1312.3223
- Downes, D., & Solomon, P. M. 1998, *ApJ*, 507, 615
- Drabek, E., Hatchell, J., Friberg, P., et al. 2012, *MNRAS*, 426, 23

Draine, B. T. 2011, *Physics of the Interstellar and Intergalactic Medium*

Draine, B. T., Dale, D. A., Bendo, G., et al. 2007, *ApJ*, 663, 866

Dumke, M., Krause, M., Beck, R., et al. 2011, in *Astronomical Society of the Pacific Conference Series*, Vol. 446, *Galaxy Evolution: Infrared to Millimeter Wavelength Perspective*, ed. W. Wang, J. Lu, Z. Luo, Z. Yang, H. Hua, & Z. Chen, 111

Elmegreen, B. G. 1987, *ApJ*, 312, 626

Ferrière, K. M. 2001, *Reviews of Modern Physics*, 73, 1031

Field, G. B., & Saslaw, W. C. 1965, *ApJ*, 142, 568

Freedman, W. L., Madore, B. F., Gibson, B. K., et al. 2001, *ApJ*, 553, 47

Galametz, M., Kennicutt, R. C., Albrecht, M., et al. 2012, *MNRAS*, 425, 763

Galametz, M., Albrecht, M., Kennicutt, R., et al. 2014, *MNRAS*, 439, 2542

Gavin, H. P. 2013, *The Levenberg-Marquardt method for nonlinear least squares curve-fitting problems*, Tech. rep., Department of Civil and Environmental Engineering, Duke University

Glover, S. C. O. 2003, *ApJ*, 584, 331

Gould, R. J., & Salpeter, E. E. 1963, *ApJ*, 138, 393

Gry, C., Boulanger, F., Nehmé, C., et al. 2002, *A&A*, 391, 675

Haynes, M. P., Giovanelli, R., & Roberts, M. S. 1979, *ApJ*, 229, 83

- Herbst, E., Chang, Q., & Cuppen, H. M. 2005, *Journal of Physics Conference Series*, 6, 18
- Hildebrand, R. H. 1983, *QJRAS*, 24, 267
- Holland, W. S., Bintley, D., Chapin, E. L., et al. 2013, *MNRAS*, 430, 2513
- Israel, F. P., Bontekoe, T. R., & Kester, D. J. M. 1996, *A&A*, 308, 723
- Janssen, M. A., & Gulkis, S. 1992, in *NATO ASIC Proc. 359: The Infrared and Submillimetre Sky after COBE*, ed. M. Signore & C. Dupraz, 391–408
- Jura, M. 1975, *ApJ*, 197, 575
- Kennicutt, R. C., & Evans, N. J. 2012, *ARA&A*, 50, 531
- Kennicutt, R. C., Calzetti, D., Aniano, G., et al. 2011, *PASP*, 123, 1347
- Kennicutt, Jr., R. C., Armus, L., Bendo, G., et al. 2003, *PASP*, 115, 928
- Kim, W.-T., & Ostriker, E. C. 2001, *ApJ*, 559, 70
- Krumholz, M. R. 2014, *ArXiv e-prints*, arXiv:1402.0867
- Kuno, N., Sato, N., Nakanishi, H., et al. 2007, *PASJ*, 59, 117
- Kwan, J. 1979, *ApJ*, 229, 567
- Leroy, A. K., Walter, F., Bigiel, F., et al. 2009, *AJ*, 137, 4670
- Leroy, A. K., Bolatto, A., Gordon, K., et al. 2011, *ApJ*, 737, 12
- Li, A. 2005, in *American Institute of Physics Conference Series*, Vol. 761, *The Spectral Energy Distributions of Gas-Rich Galaxies: Confronting Models with Data*, ed. C. C. Popescu & R. J. Tuffs, 123–133

Li, A., & Draine, B. T. 2001, *ApJ*, 554, 778

Madden, S. C., Poglitsch, A., Geis, N., Stacey, G. J., & Townes, C. H. 1997, *ApJ*, 483, 200

Madden, S. C., Galametz, M., Cormier, D., et al. 2011, in *EAS Publications Series*, Vol. 52, *EAS Publications Series*, ed. M. Röllig, R. Simon, V. Ossenkopf, & J. Stutzki, 95–101

Markwardt, C. B. 2009, in *Astronomical Society of the Pacific Conference Series*, Vol. 411, *Astronomical Data Analysis Software and Systems XVIII*, ed. D. A. Bohlender, D. Durand, & P. Dowler, 251

McKee, C. F., & Ostriker, E. C. 2007, *ARA&A*, 45, 565

McMillan, P. J. 2011, *MNRAS*, 414, 2446

Moustakas, J., Kennicutt, Jr., R. C., Tremonti, C. A., et al. 2010, *ApJS*, 190, 233

Palla, F., Salpeter, E. E., & Stahler, S. W. 1983, *ApJ*, 271, 632

Parker, E. N. 1966, *ApJ*, 145, 811

Parkin, T. J., Wilson, C. D., Foyle, K., et al. 2012, *MNRAS*, 422, 2291

Pirronello, V., Liu, C., Shen, L., & Vidali, G. 1997, *ApJ*, 475, L69

Planck Collaboration, Abergel, A., Ade, P. A. R., et al. 2011, *A&A*, 536, A25

Rémy-Ruyer, A., Madden, S. C., Galliano, F., et al. 2013, *A&A*, 557, A95

Reuter, H.-P., Sievers, A. W., Pohl, M., Lesch, H., & Wielebinski, R. 1996, A&A, 306, 721

Rosenberg, M. J. F., Kazandjian, M. V., van der Werf, P. P., et al. 2014, A&A, 564, A126

Rots, A. H. 1978, AJ, 83, 219

Rybicki, G. B., & Lightman, A. P. 1986, Radiative Processes in Astrophysics

Sandstrom, K. M., Leroy, A. K., Walter, F., et al. 2013, ApJ, 777, 5

Skibba, R. A., Engelbracht, C. W., Dale, D., et al. 2011, ApJ, 738, 89

Smith, M. W. L., Gomez, H. L., Eales, S. A., et al. 2012, ApJ, 748, 123

Soida, M., Urbanik, M., Beck, R., Wielebinski, R., & Balkowski, C. 2001, A&A, 378, 40

Tabatabaei, F. S., Braine, J., Xilouris, E. M., et al. 2014, A&A, 561, A95

Walcher, J., Groves, B., Budavári, T., & Dale, D. 2011, Ap&SS, 331, 1

Walter, F., Brinks, E., de Blok, W. J. G., et al. 2008, AJ, 136, 2563

Warren, B. E., Wilson, C. D., Israel, F. P., et al. 2010, ApJ, 714, 571

Watanabe, Y., Sorai, K., Kuno, N., & Habe, A. 2011, MNRAS, 411, 1409

Wilson, C. D., & Scoville, N. 1990, ApJ, 363, 435

Wilson, C. D., Warren, B. E., Israel, F. P., et al. 2012, MNRAS, 424, 3050



Wolfire, M. G., McKee, C. F., Hollenbach, D., & Tielens, A. G. G. M. 2003,  
ApJ, 587, 278

Wolfire, M. G., Tielens, A. G. G. M., Hollenbach, D., & Kaufman, M. J. 2008,  
ApJ, 680, 384